

Organ-Mounted Robots for Minimally Invasive Beating-Heart Surgery

Nathan A. Wood

CMU-RI-TR-15-30

December 1, 2015



The Robotics Institute
School of Computer Science
Carnegie Mellon University
Pittsburgh, PA 15213

Thesis Committee:

Cameron Riviere, *Chair*

Howie Choset

George Kantor

Pierre Dupont, *Harvard Medical School*

*Submitted in partial fulfillment of the requirements
for the degree of Doctor of Philosophy in Robotics.*

Copyright © 2015 Nathan A. Wood

For Alissa, Elliot, and Ike

Abstract

In the push to improve patient outcomes in cardiac interventions, minimally invasive beating-heart surgery is a major field of surgical research. However, interventions on a soft tissue organ under continuous motion through remote incisions pose a significant challenge. Endoscopic approaches eliminate the associated morbidity of median sternotomy, but they require either mechanical immobilization of the heart or robotic motion compensation of the tools, both of which have serious drawbacks. While mechanical immobilization may cause electrophysiological and hemodynamic changes in the performance of the heart, active compensation requires high-bandwidth manipulators to track the complex motion of the heart.

In this thesis, we address the issue of physiological motion during minimally invasive beating-heart surgery through the use of *organ-mounted robots*. These devices eschew the high dexterity and actuation effort required of traditional surgical robots in favor of miniature robots that adhere directly to the operating site using vacuum pressure. Unlike mechanical stabilizers these devices are not fixed in the world frame and therefore do not immobilize the heart but instead move in unison with the heart providing a stable platform from which interventions may be administered.

This thesis is built around two main contributions to the state of the art in robotic MIS. The first major contribution of this work is the development of *spatiotemporal registration* methods to improve positioning accuracy under *virtual image guidance* for organ-mounted robots. These efforts rely on frequency-based models, which capture the periodic motion of the heart, and anatomical models constructed from preoperative imaging. Using these models we estimate when in the *physiological cycles* the images were captured and the pose of the robot at that time to spatially align the models. Finally, we introduce a method for localizing these robots on the beating heart using function approximation that provides more accurate estimates over short time horizons.

The second major contribution is the design and construction of new robots that provide a wider array of interventions using the organ-mounted paradigm. These efforts use emerging therapies as motivation for the design of an active cooling system for minimally invasive delivery of thermosensitive materials and a new parallel wire robot, known as Cerberus, for therapies that require coverage over large areas of the surface of the heart. Both of these new capabilities are demonstrated successfully in closed-chest beating-heart procedures.

Overall, our contributions take a holistic approach to the advancement of the capabilities of organ-mounted robots. New form-factors provide specialized capabilities, while new approaches to registration improve our ability to accurately position these robots on the beating heart. Most importantly, everything presented in this thesis is demonstrated in *closed-chest beating-heart procedures*, or on data recorded in such a procedure.

Acknowledgments

This thesis, and the many years of work contained within it, would not have been possible without the support of many people. I would first like to thank my advisor, Cam Riviere, for his many (many) years of mentorship and guidance. Thanks also to the members of my thesis committee, Howie Choset, George Kantor, and Pierre Dupont.

My wife, Alissa has kept me afloat throughout this journey. She has pulled way more than her share of the weight for far too long. My children, Elliot and Ike, have motivated me to get to work in the morning, but not stay too late. I wouldn't want to miss bed time.

I owe a significant debt of gratitude to my mother for instilling in me the work ethic and perseverance required to reach this point. For your unconditional love and support I am grateful. My entire family – Joel, Jill, Ty, Elsie, Adam, Erin, Fallon, Harper, Lucas, Steve, Jodi, Danielle, Zeke, and Gabe – have been an immense support system, even from afar. I love you all.

Much of this work is the result of collaboration with many very talented people. Within the Surgical Mechatronics Lab I would like to thank (superscript denotes chapter number) Kevin Fok,⁷ Adam Costanza,⁸ Macauley Breault⁸ for the many hours and early mornings we worked on HeartLander and Cerberus.

I am very thankful to Dr. David Schwartzman, Dr. Marco Zenati, Dr. William Wagner, and Dr. Michael Passineau for the opportunities I have had to work with them and their groups. I immensely enjoyed working with Yang Zhu⁷ on the injectable hydrogel. That material still does not make any sense to me. A special thanks is due to Dr. Tomo Yoshizumi^{7,8} for the many animal labs he assisted with.

The unsung heroes of much of this work are the wonderful people at the UPMC animal lab. This work would not have been possible without the help and guidance of Dave Fischer, Linda Lavery, and Judy Thoma. I learned a great deal in the many hours we spent together.

There are so many people in the greater CMU community that affected me greatly, both socially and professionally: Brian Becker, Sungwook Yang, Craig Lehocky, Dave Rollinson, Steve Tully, Arun Rangaprasad, Elif Ayvali, Dan Munoz, Dave Silver, Felix Duvallet, Stephen Nuske, and Matt Barnes. Thank you all.

Finally, the completion of this thesis and my doctoral degree would not have been possible without the financial support provided by the U. S. National Institutes of Health (grant nos. R01HL078839 and R01HL105911) and the Disruptive Health Technology Institute at Carnegie Mellon University.

Contents

1	Introduction	1
1.1	Motivation for Organ-mounted Robots	2
1.2	Virtual Image Guidance	4
1.3	Specialized Organ-mounted Robots	5
1.4	Organization	6
2	Background	7
2.1	Anatomy of the Thoracic Cavity	7
2.2	Cardiac Dynamics	8
2.3	Minimally Invasive Cardiac Surgery	9
2.3.1	Access Methods	9
2.3.2	Tools	11
2.4	Organ-Mounted Robots	12
2.4.1	HeartLander	12
2.4.2	Lamprey	15
2.5	Medical Imaging for Guidance	16
2.6	Virtual Image Guidance	16
2.6.1	Anatomical Models	17
2.6.2	Tracking	17
2.6.3	Registration	18
2.7	Organ-Mounted Robot VIGS Protocol	19
2.7.1	Preoperative Protocol	19
2.7.2	Operating Field Layout	21
2.7.3	Measurement Collection and Processing	22
2.7.4	Fiducial Registration	24
2.7.5	Discussion	25
I	Virtual Image Guidance for Organ-Mounted Robots	27
3	The Organ-mounted Robot Registration Problem	29
3.1	Problem Formulation	29
3.2	Approach	31
3.3	Related Work	32

3.3.1	Physiological Motion Modeling	32
3.3.2	Surgical Registration	34
4	Physiological Motion Modeling	37
4.1	Analysis of Cardiac Motion	38
4.2	Periodic Motion Modeling in \mathbb{R}^3	39
4.3	Parameterizations of 3-D Rotation	41
4.3.1	Unit Quaternions	42
4.3.2	Exponential Coordinates	43
4.3.3	Euler Angles	43
4.3.4	Converting Between Parameterizations	44
4.4	Periodic Motion Modeling in $SO(3)$	44
4.4.1	Direct Quaternion Model	45
4.4.2	Intermediate Frame Models	45
4.5	Intermediate Frame Translation Model	46
4.6	Model Parameter Estimation	47
4.7	Experiments	48
4.7.1	Rotation Model Comparison	48
4.7.2	Model Fidelity	50
4.7.3	Online Estimation and Prediction	52
4.8	Discussion	54
5	Spatiotemporal Registration	59
5.1	Problem Formulation	60
5.2	Experimental Data	62
5.3	Experiments	64
5.3.1	Respiration Phase Registration	64
5.3.2	Spatial Registration Comparison	67
5.4	Discussion	68
6	Localization	71
6.1	Localization via Motion Prediction	72
6.2	Localization via Function Approximation	73
6.2.1	Radial Basis Function Approximation	74
6.2.2	RBF's for Organ-mounted Robot Localization	75
6.3	Experiments	76
6.3.1	RBF Localization Performance	77
6.3.2	Effects of Center Density	78
6.3.3	Motion Prediction Comparison	80
6.4	Discussion	81

II	Specialized Organ-mounted Robots	83
7	HeartLander: Delivery of Thermosensitive Materials	85
7.1	Hydrogel for Myocardial Infarction Therapy	86
7.1.1	Clinical Relevance	86
7.1.2	Thermoresponsive Hydrogel Design	87
7.2	Design of Active Cooling System	88
7.2.1	Simulation Study	89
7.2.2	Water Bath Study	90
7.2.3	Incorporation into HeartLander	92
7.3	Experiments	92
7.3.1	Water Bath Injections	92
7.3.2	Injections Ex Vivo	93
7.3.3	Beating Heart Injections in Porcine Model	94
7.4	Discussion	98
8	Cerberus: A Parallel Wire Robot for Epicardial Interventions	99
8.1	Gene Therapy for Congestive Heart Failure	100
8.1.1	Clinical Relevance	100
8.1.2	Cerberus Concept	101
8.2	Design and Control of Cerberus Robot	102
8.2.1	Hardware	102
8.2.2	Inverse Kinematics	103
8.2.3	Statics	105
8.2.4	Injector Rotation	107
8.2.5	Optimal Tension Distribution	108
8.2.6	Control System	109
8.3	Experiments	110
8.3.1	Control Experiments	110
8.3.2	Beating Heart Injections in Porcine Model	112
8.4	Discussion	115
III	Conclusions and Future Work	117
9	Conclusions	119
10	Future Work	123
10.1	Virtual Image Guidance	123
10.2	Cooled Injection	124
10.3	Cerberus	125
	Bibliography	127

List of Figures

2.1	The Cardiothoracic Cavity	8
2.2	Displacements and Velocities of the RCA	9
2.3	Minimally Invasive Cardiac Access	10
2.4	Minimally Invasive Cardiac Surgical tools	11
2.5	The HeartLander robot.	12
2.6	Subxiphoid pericardial access.	13
2.7	The Lamprey robot.	15
2.8	Real-Time Medical Imaging Modalities	17
2.9	Image guided surgery virtual environment.	18
2.10	Heart Surface Model Construction	21
2.11	Operating Field Arrangement	22
2.12	Cardiac Phase Estimation from ECG Signal	24
2.13	Respiration Phase Estimation from Respiration Flow Sensors	24
4.1	Translation and Rotation on the Beating Heart	38
4.2	Cardiac Motion Frequency Response	39
4.3	Block Diagram of Online Estimation Scheme	48
4.4	Offline Estimation of Periodic Rotation	49
4.5	Model Fidelity Experimental Errors	51
4.6	Results of Online Estimation of Physiological Motion	54
4.7	Model Parameter Convergence for Online Estimation	55
4.8	Global Error for Online Estimation and Prediction for a 5 s Horizon	55
5.1	Spatiotemporal Registration Diagram	61
5.2	Spatiotemporal Registration RMS Error	62
5.3	Gated Cardiac CT per Slice Image Phase	64
5.4	Spatial Registration Parameters for All Respiration Phases	65
5.5	Magnitudes of Registration Distance	66
5.6	Qualitative Results of Registration	66
5.7	Difference in estimated position between registration methods.	68
6.1	Motion Prediction Localization Scheme	73
6.2	Locally-Weighted Regression Motion Prediction Scheme	74
6.3	RBF Interpolation Performance	77
6.4	Uniform Sampling of Centers	78

6.5	Effect of Center Density on RBF Interpolation	79
6.6	Localization Method Comparison	80
7.1	Characterization of Thermoresponsive Hydrogel	87
7.2	Schematic of Active Cooling System	89
7.3	Simulation Results for Optimizing Cooled Injection System	90
7.4	Water Bath Cooling Performance	91
7.5	Modified HeartLander with cooled injection system.	92
7.6	Injection Performance in Water Bath	93
7.7	Ex Vivo Injection in Porcine Heart	94
7.8	Photoacoustic imaging of patterned injections in a beating porcine heart.	96
7.9	Overlay of photoacoustic image with the preplanned injection sites.	97
8.1	Conceptual Design of Cerberus Robot	102
8.2	Cerberus Robotic System Hardware	103
8.3	Kinematic Diagram of Cerberus	104
8.4	Free Body Diagram of Injector Head	106
8.5	Identification of Singular Pose Using Eigenvalues	107
8.6	Orientation Surface Plots	108
8.7	Normalized Wire Tensions	110
8.8	Normalized Wire Tension Ratios	111
8.9	Parallel Force/Position Control Diagram	111
8.10	Control Experiment Hardware and Tool Path	112
8.11	Cerberus Positioning Error	113
8.12	Subxiphoid Insertion of Cerberus Robot	113
8.13	Cerberus Deployed in vivo	114
8.14	Live Animal Injections with the Cerberus Robot	115

List of Tables

4.1	Orientation Relative Prediction Error	50
4.2	Preferred Model List	52
5.1	Trial Data	63
6.1	Results from Center Density Experiment	79

Chapter 1

Introduction

The primary goal of minimally invasive surgery (MIS) is to minimize the unnecessary trauma inflicted during a surgical intervention. Among the benefits of MIS compared to traditional surgery are lower risk of infection, reduced post-operative pain, recovery time, and duration of hospitalization. Typically, MIS is accomplished is by reducing the size of the incisions used to gain access to the surgical site and using long tools to remotely perform the procedure. While the exact methods used vary based on the target anatomy, the general approach remains constant.

In the field of cardiac surgery the “gold standard” approach to access the heart, median sternotomy, is especially traumatic. This technique uses a midline incision from the sternal notch to below the xiphoid process to reveal the sternum, which is then separated with a saw and spread with a sternal retractor. While this approach provides unrivaled access to the heart, it causes significant trauma to the patient.

A wide range of less invasive access techniques for procedures including coronary artery bypass grafting (CABG), aortic valve surgery (AVS), and mitral valve surgery (MVS) have been developed which significantly reduce patient trauma. Mini-sternotomies only separate a portion of the sternum; peristernal approaches gain access by removing the costal cartilage of the ribs next to the sternum; thoracotomies gain access via incisions

in the intercostal spaces between the ribs [1]. Recent data suggests that these minimally invasive approaches are not inferior to conventional approaches [2].

While these approaches significantly reduce the trauma associated with the mode of access they are often used in conjunction with cardiopulmonary bypass (CPB) where the heart and lungs are temporarily stopped and their functions are mechanically replaced. It has been shown, however, that CPB can lead to serious complications [3, 4] and is highly correlated with postoperative stroke [5].

Further improvements in minimally invasive cardiac surgery have arisen from the use of mechanical cardiac stabilizers, such as the Medtronic StarfishTM and OctopusTM, enabling interventions to be performed on the beating heart [6, 7].

The most recent advances in minimally invasive cardiac surgery are the introduction of robotic tele-manipulation systems like the da Vinci System (Intuitive Surgical, Mountain View, CA). These systems provide for improved articulation, stereoscopic vision of the operating site, and improve hand-eye coordination when compared with existing thoracoscopic approaches [8]. Robotic-assisted procedures have been shown to reduce the length of hospitalization, incidence of complications, and mortality when compared to their non robotic counterpart [9]. When coupled with mechanical immobilization of the heart and keyhole intercostal incisions, robotic totally endoscopic procedures are one of the least invasive approaches to perform interventions on the heart [1].

1.1 Motivation for Organ-mounted Robots

Although the robotic thoracoscopic approach to cardiac surgery is a significant improvement over conventional approaches in terms of reducing patient trauma, there still exists room for improvement. The intercostal thoracoscopic approach requires deflation of the left lung, general endotracheal anesthesia, and differential ventilation, adding to the overall morbidity and can lead to complications separate from the cardiac intervention [10, 11].

Mechanical stabilization has been shown to adversely affect the electrophysiological and mechanical performance of the heart due to the forces exerted on the heart [12, 13], and care must be taken to avoid arrhythmia or hemodynamic impairment [14]. Even with immobilization residual motions of 1.5 to 2.4 mm may still remain [15, 16]. The intercostal approach used also limits the availability of distal regions of the heart, such as the posterior left ventricle [14]. The left ventricle is the most severely affected region of the heart by myocardial infarct and congestive heart failure [17].

In order to avoid the existing drawbacks in minimally invasive cardiac surgery, our group has pioneered the development of miniature robots for cardiac interventions. These robots, which we refer to as organ-mounted robots, address the three previously listed drawbacks with minimally invasive cardiac surgery.

First, the robots adhere to the epicardial surface of the heart, under the pericardium, using vacuum pressure, which has been demonstrated to be safe in the case of mechanical cardiac stabilizers [6, 7], without applying the large forces due to restraining the motion. Next, access to the heart is gained via a subxiphoid approach which avoids the space occupied by the lungs, thus obviating the need for lung deflation and differential ventilation [18, 19]. Finally, these robots have the capability of moving through the pericardial space under their own power, or that of the clinician, enabling them to reach distal portions of the heart currently unavailable to thoracoscopic approaches.

We feel strongly that the most important impact of the organ-mounted robot paradigm will not be the improvement of existing procedures, but rather the enabling of new types of procedures that are currently not performed due to limitations of operating on the beating heart. These procedures, however, may not be developed until the enabling technology is in place.

1.2 Virtual Image Guidance

A major issue for organ-mounted robots arises due to the subxiphoid approach used to gain access to the heart in conjunction with the anatomy of the mediastinum. Because of the small incision used to gain access, line of sight to the heart is occluded and because of the tightly packed space around the heart, video endoscopes do not provide sufficient field of view to be helpful. Real-time medical imaging such as ultrasound, fluoroscopy, real-time computed tomography (CT) or magnetic resonance imaging (MRI) has been used for guiding minimally invasive procedures; however these methods are noisy, slow, expensive, and potentially harmful.

To address these issues, virtual image-guided methods are instead used to provide the surgeon with visual feedback during procedures. In this framework models of the anatomy created from preoperative imaging are used in conjunction with live measurements of the 6 degree-of-freedom tool pose from an electromagnetic positioning sensor to provide a virtualized representation of the operating site. When we attempt to fuse the information from the preoperative models and tool position measurements however, we must address the issue of temporal misalignment between the measurements and anatomical models.

The approach taken in this thesis is to first model the quasi-periodic 6-DOF motion the robots undergo using frequency-based models. These models capture the complex dynamics of the motion of points on the surface of the heart, and enable us to predict the pose of an observed point at any phase. Using a collection of these observations, we next estimate when the images were acquired by spatially registering the predicted pose of the robots with the static models. While minimizing the standard registration distance metric is unfruitful, we show that we can register temporally by minimizing the magnitude of the corresponding spatial registration. Once registered spatially and temporally, the location of the robot on the surface of the heart is found by projecting the robot's current position to the known image phase. This projection can be done using the frequency-based models;

however, they require observing complete motion cycles before they converge. Our final contribution is posing projection onto the registered heart as a function approximation problem which uses previously observed motions to localize on the heart. This approach provides more accurate estimates of robot position than the frequency based models alone over short time horizons.

1.3 Specialized Organ-mounted Robots

Due to the unique constraints imposed by the operating on the beating heart, we do not have the luxury of using general platform to which we add on specialized tools for specific interventions. For all the success shown with the original organ-mounted robot, HeartLander [20], it excels at a narrow range of interventions, namely those that require a relatively small number of accurately placed or tightly grouped point interventions, such as injections or ablation. There are many emerging therapies for which the existing HeartLander robot is ill suited. The development of new types of organ-mounted robots with specialized capabilities will expand the potential applications this approach to minimally invasive cardiac surgery can enable.

This thesis expands the capabilities of organ-mounted robots by first designing an active cooling system for delivery of thermoresponsive hydrogels for myocardial infarction therapy. These materials transition from a liquid to gel state well below body temperature, and when injected into infarcted heart tissue reduce ventricular remodeling [21]. Through these efforts we demonstrate the ability to deliver thermosensitive materials to the beating heart in a minimally invasive manner.

We next present the design and control of a miniature parallel wire robot for gene therapies for chronic heart failure. These therapies require controlled dosage of material to wide large areas of the left ventricle, a task for which HeartLander is ill-suited. Due to the significant space constraints, our robot design possesses kinematic non-idealities

which require special attention. Through these efforts we develop and demonstrate a new organ-mounted robot capable of global, homogenous delivery on the beating heart.

1.4 Organization

The contributions of this thesis are divided into two parts. Relevant background for both parts is first discussed in Chapter 2. Part I presents our efforts to provide more accurate interventions using organ-mounted robots and begins with by formally defining the framework for image guided surgery in Chapter 3. Chapter 4 presents our work on modeling the quasi-periodic motion our robots undergo on the surface of the heart. Chapter 5 uses the models for the motion of the heart to solve for both spatial and temporal registration to provide for accurate positioning on the surface of the heart. Chapter 6 presents a method for localizing on the surface of the heart with constant performance in time and providing better estimates of position over short time horizons.

Part II describes our effort to develop a family of organ-mounted robots that provide capabilities specifically designed for a multitude of interventions. Chapter 7 presents the design and demonstration of our actively cooled injection system, while Chapter 8 presents the design, control, and demonstration of an parallel-wire organ-mounted robot.

Chapter 9 summarizes our contributions and presents conclusions and implications of this work. Finally, extensions to this thesis and new research directions for organ-mounted robots are presented in Chapter 10.

Chapter 2

Background

Organ-mounted robots represent a vastly different approach to minimally invasive cardiac surgery than existing approaches. These robots were specifically designed to address the limitations that exist with state of the art robotic approaches to reduce patient trauma and provide a more stable platform for launching interventions. This chapter first introduces the arena that these robots target and describe the unique challenges it poses. Next, existing approaches to minimally invasive surgery (MIS) are explored. Finally, the original organ-mounted robot, HeartLander, is introduced as the genesis of the organ mounted approach to beating heart surgery.

2.1 Anatomy of the Thoracic Cavity

The heart resides in the mediastinum, the central lower section of the cardiothoracic cavity, encased by a two-layered sac called the pericardium. Although the heart moves during the heartbeat, there is very little free space around the heart as it is surrounded on all sides by various anatomy as shown in Fig. 2.1. In the coronal plane, 2.1(a), the lungs and diaphragm surround the heart, while in the axial plane, 2.1(b), it is restricted by the lungs, sternum, spinal column, and esophagus. While the heart is surrounded by these

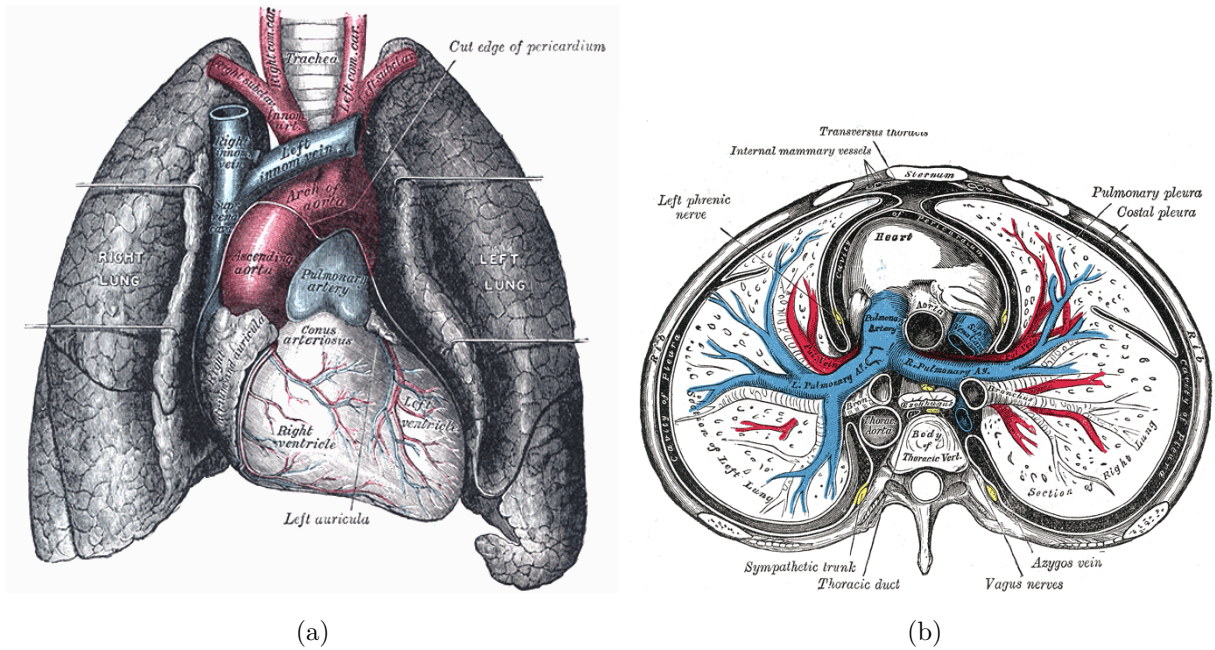


Figure 2.1: Illustrations of the anatomy of the cardiothoracic cavity in the (a) coronal plane and (b) the axial plane. The heart is surrounded on all sides by the lungs, diaphragm, sternum, and spine. This figure reproduced from [22]

anatomical structures, the only attachment point of the heart is to the great vessels at the base of the heart, allowing the heart to move and deform.

2.2 Cardiac Dynamics

Points on the surface of the undergo large displacements due to both the heartbeat and respiration. Previous studies conducted by Shechter et al. [23] measured the displacements and velocities of the coronary arteries in human patients using data collected from biplane angiograms. Representative data from these studies are shown in Fig. 2.2. For the tracked anatomical locations peak displacements of up to 26.3 mm and peak velocities of up to 130.7 mm/s were observed due to the heartbeat, while displacements and velocities due to respiration peaked at 7.2 mm and 9.0 mm/s respectively.

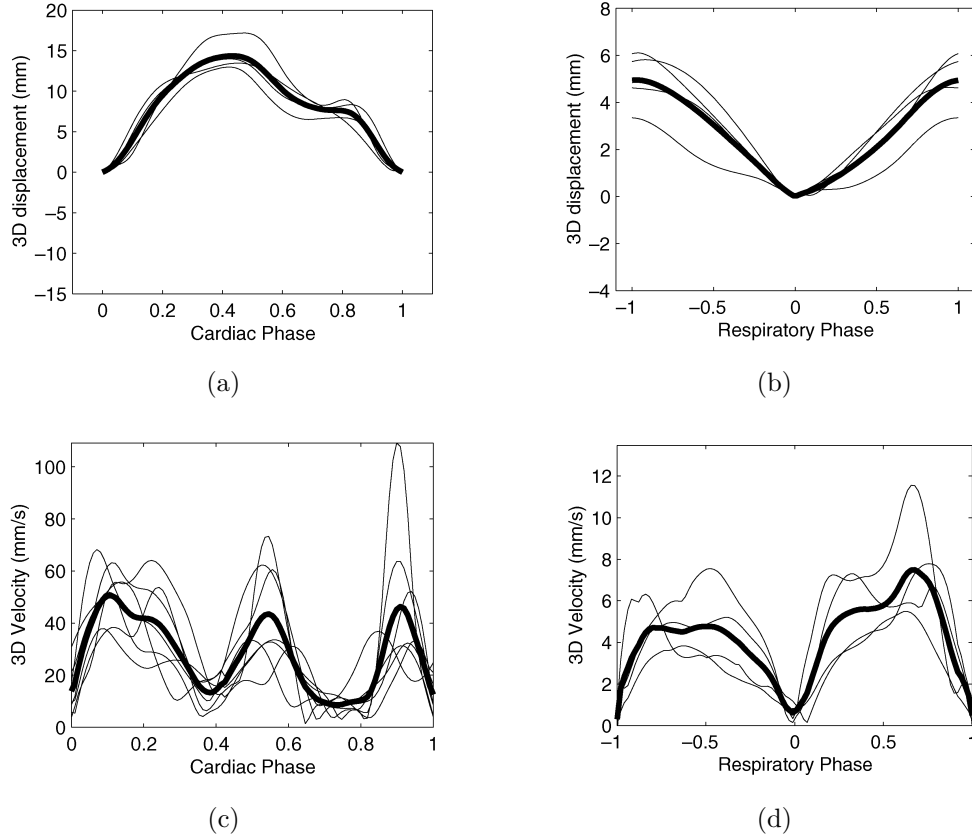


Figure 2.2: Data showing the 3D displacement of the right coronary artery due to (a) cardiac motion and (b) respiratory motion, and the 3D velocity of the RCA due to (c) cardiac motion and (d) respiratory motion. Each trace corresponds to a single human subject, with the bold trace corresponding to the mean. This figure is reproduced from [23].

2.3 Minimally Invasive Cardiac Surgery

2.3.1 Access Methods

The range of access methods from the standard median sternotomy to the keyhole thoracoscopic incisions employed in minimally invasive robotic endoscopic procedures are shown in Fig. 2.3. The median sternotomy provides access to the heart by separating the sternum entirely. Less invasive approaches which significantly reduce patient trauma have been developed for a variety of procedures.

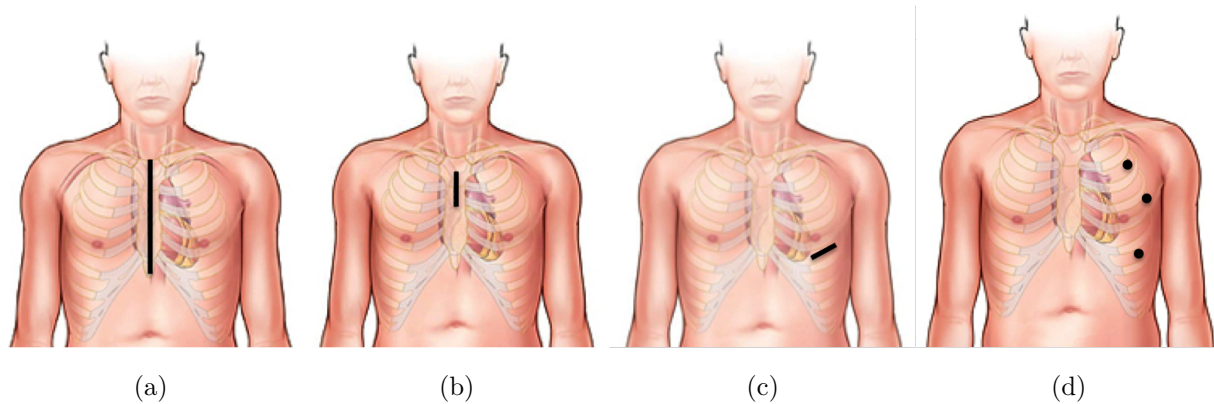


Figure 2.3: Access methods to the heart include (a) the standard median sternotomy, (b) partial sternotomy, (c) left thoracotomy, and (d) endoscopic keyhole. Image credit to The Cleveland Clinic.

Mini-sternotomies, shown in Fig. 2.3(b), only separate a portion of the sternum and can be used for aortic and mitral valve replacements; thoracotomies, shown in Fig. 2.3(c), gain access via incisions in the intercostal spaces between the ribs and can be used for minimally invasive direct coronary artery bypass (MIDCAB) [1]; keyhole intercostal incisions, shown in Fig. 2.3(d), are employed for totally endoscopic coronary artery bypass and grafting (TECAB) [1].

Each of these approaches requires either gaining access by partially or fully separating the sternum, or going through the pleural space, which is the space occupied by the lungs. Deflation of a lung, general endotracheal anesthesia, and differential ventilation, adds to the overall morbidity and can lead to complications separate from the cardiac intervention [10, 11]. The intercostal approach used also limits the availability of distal regions of the heart, such as the posterior left ventricle [14]. The left ventricle is the most severely affected region of the heart by myocardial infarct and congestive heart failure [17].

These approaches are often also used in conjunction with cardiopulmonary bypass (CPB) where the heart and lungs are temporarily stopped and their functions are mechanically replaced. It has been shown, however, that CPB can lead to serious complications [3, 4] and is highly correlated with postoperative stroke [5].



Figure 2.4: Tools used during minimally invasive cardiac surgery include (a) hand held endoscopes (Karl Storz BmbH & Co., Tuttlingen, DEU), (b) tissue stabilizers such as the Octopus® Nuvo tissue stabilizer (Medtronic, Minneapolis, MN, USA), and (c) the da Vinci® surgical robot (Intuitive Surgical Inc., Sunnyvale, CA, USA)

2.3.2 Tools

Advancement in tools used in minimally invasive cardiac tools from the standard hand-held laparoscopic tools, shown in Fig. 2.4(a), have caused further improvements in MIS. Mechanical cardiac stabilizers, such as the Medtronic Starfish® and Octopus®, shown in Fig. 2.4(b), enable interventions to be performed on the beating heart [6, 7].

The most recent advances in minimally invasive cardiac surgery are the introduction of robotic tele-manipulation systems like the da Vinci System (Intuitive Surgical, Mountain View, CA), shown in Fig. 2.4(c). These systems provide for improved articulation, stereoscopic vision of the operating site, and improve hand-eye coordination when compared with existing thoracoscopic approaches [8]. Robotic-assisted procedures have been shown to reduce the length of hospitalization, incidence of complications, and mortality when compared to their non robotic counterpart [9]. When coupled with mechanical immobilization of the heart and keyhole intercostal incisions, robotic totally endoscopic procedures are one of the least invasive approaches to perform interventions on the heart [1].

Mechanical stabilization, however, has been shown to adversely affect the electrophys-

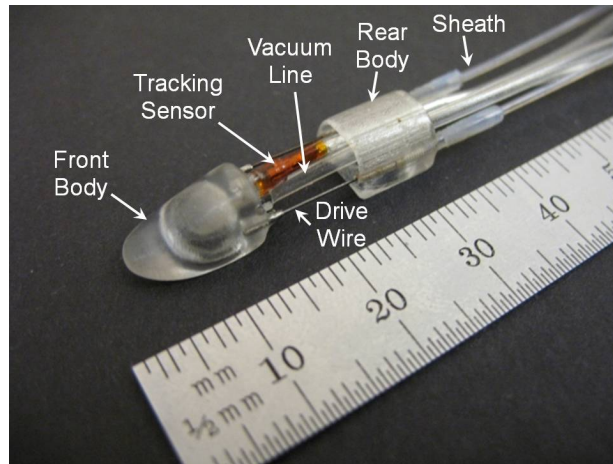


Figure 2.5: The HeartLander robot.

iological and mechanical performance due to the forces exerted on the heart [12, 13], and care must be taken to avoid arrhythmia or hemodynamic impairment [14]. Even with immobilization residual motions of 1.5 to 2.4 mm may still remain [15, 16].

2.4 Organ-Mounted Robots

2.4.1 HeartLander

The inspiration for the work presented in this thesis is the HeartLander robot [24–26]. HeartLander, shown in Fig. 2.5 is a small inchworm-style robot designed specifically to overcome the limitations of existing minimally invasive cardiac approaches.

HeartLander consists of two “feet” that measure $5.5 \times 8 \times 8$ mm which adhere to the heart independently using vacuum pressure that is maintained between 400 to 600 mmHg. This pressure range has been shown to be safe and effective for use in mechanical cardiac stabilizers that are routinely applied for hours during surgery [7]. The small size of the robot allows it to operate entirely within the pericardial space and, by adhering to the surface of the heart, the robot provides a platform of zero relative motion from which interventions may be administered.

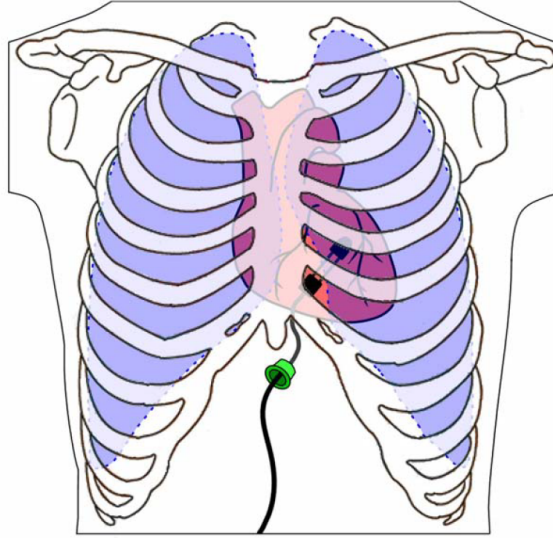


Figure 2.6: Access to the pericardial space is achieved by inserting the robot through a subxiphoid skin incision. Photo credit to [25]

Access to the apex of the heart is achieved through a small port below the xiphoid process of the sternum in conjunction with a small incision in the pericardium at the apex of the heart. HeartLander is then placed in the intrapericardial space. An illustration of this approach is shown in Fig. 2.6. A major advantage of the subxiphoid approach in comparison with other access methods is that the space occupied by the lungs is undisturbed, removing the need for differential ventilation and lung deflation [18]. In principle this means that general anesthesia is not required and HeartLander interventions could be performed on an outpatient basis.

Locomotion over the surface of the heart is achieved by alternating suction between the front and rear feet and extending and retracting the drive wires. Due to the use of flexible nitinol as drive wires, turning motions may be achieved by differentially extending the drive wires. The locomotion capabilities of HeartLander enable it to reach all portions of the heart and not be constrained by the access point.

In order to provide position feedback a miniature 6-DOF magnetic tracker (microBIRD, Ascension, Burlington, VT) is embedded in the front foot of the robot. This device provides

real-time feedback of the position and orientation of the robot relative to an electromagnetic emitter with a resolution of 0.5 mm in position and 0.1° in orientation.

Therapies that are strong candidates for HeartLander to provide must possess three main characteristics. First, the therapy must be able to be delivered entirely through the intrapericardial space. Second, they can be completed using flexible 1-DOF actuators which are integrated into the HeartLander platform. Finally, the treatments which are most suitable for HeartLander are those which require multiple accurately located tightly grouped treatment sites on the surface of the heart. There are many procedures which conceivably could be performed using HeartLander, including, but not limited to cell transplantation [27], gene therapy for angiogenesis [28], intrapericardial drug delivery [29], epicardial electrode placement for resynchronization [30], epicardial atrial ablation [31]

Three main therapies have been demonstrated using the HeartLander robot in the porcine model: myocardial injection, epicardial pacing, and epicardial ablation. Myocardial injection refers generally to the injection of a material into the heart muscle, or myocardium. Successful injections of hydrogel into the porcine heart have recently been demonstrated, while successful injections of dye have been previously shown [25]. Epicardial pacing is a potential treatment for congestive heart failure (CHF) in which pacing leads are placed at multiple sites to alter the degree of electromechanical asynchrony in patients with significant conduction disorders. Successful lead placement and electrical pacing tests have been demonstrated using the HeartLander robot [32]. The final therapy demonstrated using the HeartLander robot is epicardial ablation. Ablation or destruction of cardiac tissue with an electrode is a technique used to treat atrial fibrillation (AF), a condition in which the atria rapidly contract asynchronously from the normal heartbeat rhythm. Spot ablations have been successfully performed in a porcine model using the HeartLander robot retrofitted with a RF ablation tip [20].

HeartLander excels at a relatively narrow range of interventions that consist of tight



Figure 2.7: The Lamprey robot.

groupings of point interventions. Even with all of the advantages provided by the sub-xiphoid access and organ-mounted approach employed by HeartLander, there are many emerging therapies for which the existing HeartLander robot is ill suited. The development of new types of organ-mounted robots with specialized capabilities will expand the potential applications this approach to minimally invasive cardiac surgery can enable.

2.4.2 Lamprey

Reduction of the organ-mounted paradigm to its simplest form yields the robot we refer to as Lamprey, shown in Fig. 2.7. This device consists of a single distal "foot," which houses a suction chamber on its bottom surface, and a flexible cable attached to the foot which protrudes from the body. Motion over the surface of the heart is achieved by manually applying forces to the proximal end of the flexible cable, while vacuum pressure is supplied by a single vacuum line which connects to the off board instrumentation. Essentially, this device is equivalent to a catheter with a suction cup at the tip, and relies on the operator to manually position the tool. This device is capable of delivering the same therapies as HeartLander, but is most applicable to those which do not have tight constraints on positioning accuracy.

2.5 Medical Imaging for Guidance

A major hurdle in minimally invasive cardiac surgeries is providing the surgeon sufficient information to successfully perform the intervention. While the minimally invasive robotic approaches employ video endoscopy for visual feedback, due to the subxiphoid approach and the tightly packed thoracic cavity we must use alternative methods for guidance.

Image guided surgeries (IGS) or image guidance interventions (IGI) are generally defined as minimally invasive interventions which use any form of imaging for guidance [33]. This definition includes procedures which have used real-time magnetic resonance imaging (MRI) to perform catheterization [34] and aortic valve replacement [35], three-dimensional ultrasound (3DUS) to repair atrial septal defects [36], and cone-beam computed tomography (CBCT) [37], a variant of fluoroscopy. Example images from these modalities can be seen in Fig. 2.8. Each of these imaging modalities has its own drawbacks. MRI requires material compatibility, real-time CT and fluoroscopy pose radiation concerns, and ultrasound is noisy.

In order to provide situational awareness to the clinician during MIS using organ mounted robots, we instead employ virtual image guided surgery. This method relies on preoperative models of the anatomy and tracked tools to provide the clinician a virtual view of the environment. This chapter outlines the component parts of virtual image guidance and how the information is fused to provide an accurate representation of surgery.

2.6 Virtual Image Guidance

Virtual image guidance refers to those minimally invasive procedures that use preoperatively generated models of the anatomy and tracked tools to provide a virtualized view of the operating sight to the clinician [38–40]. An example of the virtualized view can be seen in Fig. 2.9. The architecture for such a system is composed of three major components:

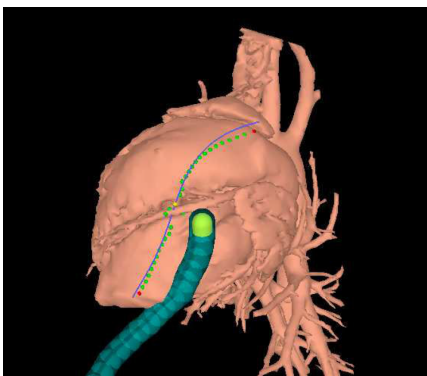


Figure 2.9: Example visualization provided in an image guided surgery with the Highly Articulated Robotic Probe (HARP) . Photo credit to [38]

as the 3-D Guidance system (Ascension, Burlington, VT) do not suffer from line-of-sight restrictions and allow for tracking inside the body.

2.6.3 Registration

Registration is the determination of the mathematical relationship between homologous points in two different spaces. When this mapping is known the two spaces are considered to be registered [42]. In the context of virtual image guided surgery, registration often refers to the rigid transformation which aligns the anatomical models with their real-world counterpart [33].

The most common form of patient registration involves identifying corresponding points in the model and patient spaces and solving for the rigid transformation between the two coordinate frames using a least-squares approach [43, 44]. Such methods are used for fiducial registration where easily identifiable markers are placed on the patient prior to imaging and remain throughout the intervention. Registration between image-based anatomical models and real-world surface data collected using sources such as ultrasound [45], laser range scanner [46], or tracked tools generally utilizes an iterative approach to aligning the models, most commonly the iterative closest point (ICP) algorithm [47].

2.7 Organ-Mounted Robot VIGS Protocol

This section explicitly defines pre- and intraoperative methods used for virtual image guided organ-mounted robotic surgery (VIGORS) in live-animal closed-chest beating-heart procedures that are of importance to this work. These methods are part of a protocol that follows the National Institutes of Health guidelines for animal care and was approved by the University of Pittsburgh’s Institutional Animal Care and Use Committee. All of the data used in the following chapters were collected and processed using the methods described in this chapter. We first describe the preoperative placement of fiducials on the animal, collection of volumetric imaging, and construction of the map of the heart. Next, we describe the layout of the operating field and the collection and processing of measurements we use in the remainder of the work and conclude with the pre-operative registration procedure.

2.7.1 Preoperative Protocol

Fiducial Placement External skin markers were placed on the chest for use as initial estimates of spatial registration. The markers used were Weck Visistat 35W 6.5 mm x 4.7 mm staples (Ref. #528235, Teleflex Medical, Research Triangle Park, NC). The 3x3 grid of markers was applied with a spacing of approximately 4 cm, with the center marker placed at the midpoint of the line from the xiphoid cartilage and the manubrium of the sternum.

Imaging ECG-gated cardiac CT image sets were collected prior to each surgery using a LightSpeed VCT imaging system (GE Medical Systems). ECG-gating techniques are used to provide snapshots of the heart at a fixed instant in the cardiac cycle and use the ECG signal. The imaging system provided retrospectively gated image sets which retroactively align image slices of the same phase. The desired cardiac phase of the image sets was $\phi_c = 0.7$, corresponding to the most common motion-free imaging window during diastole

[48]. During the collection of the image sets, forced ventilation was halted after inspiration.

The ground-truth cardiac phase for each slice in the image sets was estimated using image metadata that included the time each image was collected as well as the time of every detected QRS complex in the ECG. Cardiac phase for each slice was calculated as the proportion of time between successive QRS detections. Cardiac phase for the entire image volume, ϕ_C^* , is estimated as the average phase of the image slices. Image sets had an axial slice thickness of 0.625 mm, with in-plane pixel spacing of 0.488 mm.

Model Construction CT volumes were manually segmented using OsiriX[®] software (Fondation OsiriX, Geneva, Switzerland) to produce triangle mesh surface models of the heart, fiducial markers, and various other anatomical structures for visual feedback purposes including the ribs, coronary arteries, and endocardial surfaces. These surface models were then further processed using MeshLab [49] to smooth, close holes, and decimate the surface models.

Models were then transformed into a heart-centric reference frame. This frame is defined by first recursively fitting ellipses to the vertices of the heart model in 10-mm slices in the z -direction, and aligning the new z -axis with the centroid of these ellipses. The x -axis is then defined as the weighted average, by eccentricity, of the minor axes of the ellipses. Locations of the fiducials in the map frame were also collected to provide initial patient registration.

Examples of the segmented models, ellipses fit to the heart model, and the heart-centric reference frame are shown in Fig. 2.10. The heart-centric frame as defined here is analogous to standard medical imaging views of the heart where slices parallel to the xy -, xz -, and yz -planes give short axis, vertical long axis, and horizontal long axis views respectively.

These heart-centric surface models used for image guidance, \mathcal{S} , are triangular meshes that consist of approximately 10,000 vertices. For the remainder of this work we use the notation \mathbf{u} to refer to the location on the surface of the map, and can be thought of as

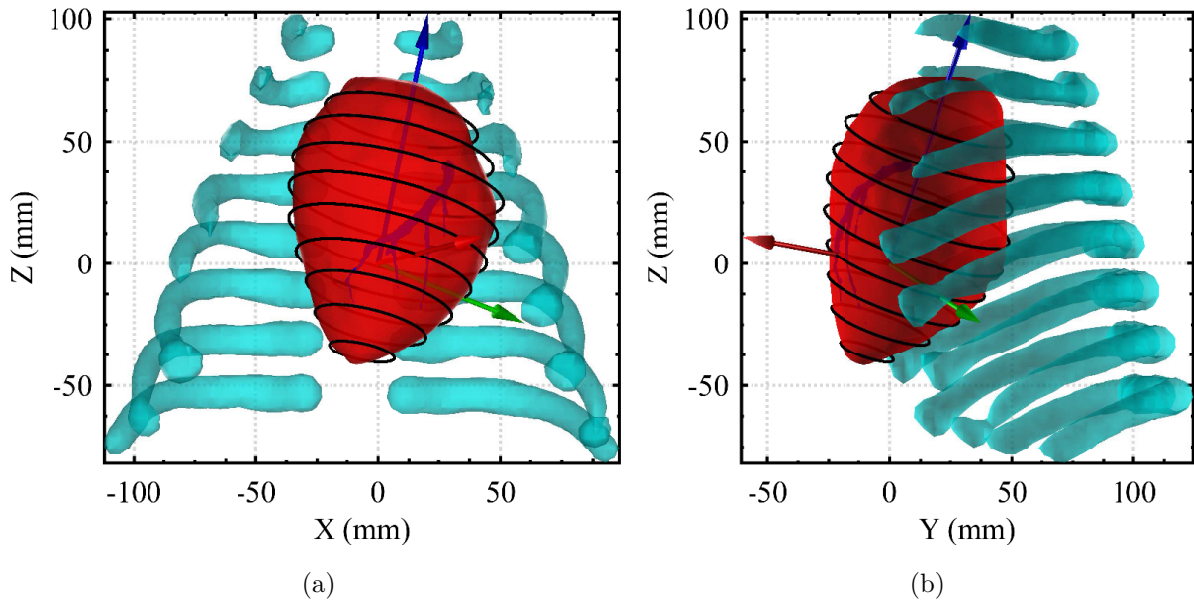


Figure 2.10: (a) Front and (b) right views, in image coordinates, of the segmented anatomical structures. Ellipses fit to the heart surface model define the heart-centric reference frame, with the z -axis defined by their centers, and y - and x -axes defined by their major and minor axes respectively.

the latitude and longitude coordinates. The previously described process of aligning the heart model places the apex of the heart at the south pole, enabling \mathbf{u} to be thought of as a latitude and longitude coordinate on the surface. The notation $\mathcal{S}(\mathbf{u})$ is used to refer to the 3D coordinates of the location \mathbf{u} in the map frame.

2.7.2 Operating Field Layout

The animal was placed in the supine position and draped for each experiment. The micro-Bird magnetic tracking sensor (Ascension Technologies, Burlington, VT) base frame was placed on the operating table adjacent to the animal such that the x -axis of the tracking frame approximately aligned with the centroid of the heart. A magnetic tracking probe was secured to the chest wall using surgical tape to provide measurements that are fixed in the patient frame. Working with the relative poses ensures that motion of the patient or mea-

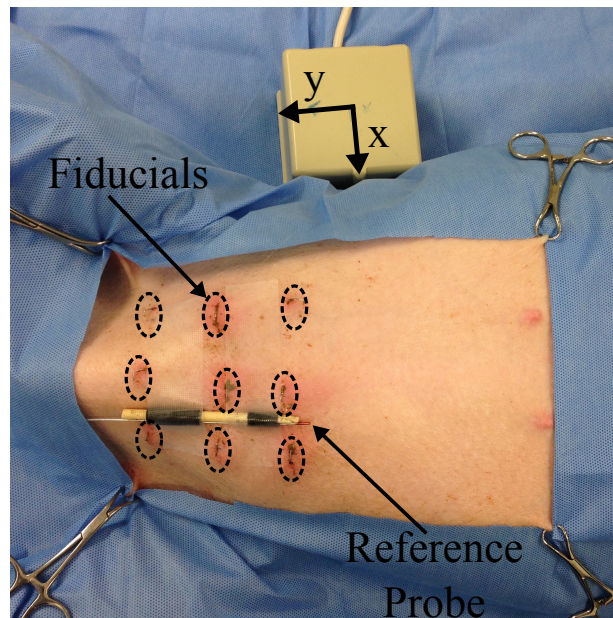


Figure 2.11: The arrangement of the operating field. The electromagnetic tracker is placed as close to the thoracic cavity as possible. A reference probe is placed on the chest well to provide a patient-fixed reference frame, while a matrix of fiducial markers enables initial patient registration.

surement frame does not corrupt the data. The arrangement of the animal, measurement frame, and reference probe frame are shown in Fig. 2.11.

2.7.3 Measurement Collection and Processing

Throughout the procedure measurements and state variables are logged at 100 Hz for diagnostic and research purposes. The work presented in the following three chapters is demonstrated retrospectively on data logged during experiments in vivo. We briefly describe here the collection and processing of the measurements that are of significance to the work presented.

Robot Pose Measurements of the 6-DOF pose of both the robot and reference probe from the microBird magnetic tracking system were logged at 100 Hz. The raw measurement signals were then processed to yield the signals used in the remainder of this work. The

pose of the robot in the measurement frame, \mathbf{T}_H^W , and the pose of the reference probe in the measurement frame, \mathbf{T}_P^W , yield the pose of the robot in the reference frame, $\mathbf{T}_H^P = \mathbf{T}_P^{W^{-1}}\mathbf{T}_H^W$. Again we choose to operate in the patient-relative frame so that the system is not sensitive to unintended patient motion.

Cardiac Phase An electrocardiogram (ECG) signal is recorded using the 0-1 V analog output from a LIFEPAK 12 defibrillator/monitor (Medtronic, Minneapolis, MN) using a Physio-Control LIFEPAK 12/15 Analog ECG Output Cable (Part #: 3010484-00). A representative time trace of the ECG signal is shown in Fig. 2.12.

Cardiac phase is defined as the percentage of a cardiac cycle completed, with zero phase corresponding to the onset of systole, or the contraction of the heart. The beginning of systole corresponds with the R wave in the ECG signal. Cardiac phase, ϕ_C , was extracted from the raw ECG signal by first using a Pan-Tompkins QRS detection algorithm [50] to detect the QRS complexes and then linearly interpolating between them. Cardiac phase is then defined as

$$\phi_C(k) = \frac{t(k) - t_{QRS}}{t_{QRS+1} - t_{QRS}}, \quad (2.1)$$

where $t(k)$ is the current time, t_{QRS} is the time of the last QRS detection, and t_{QRS+1} is the time of the next QRS detection.

Respiration Phase Forced respiration was used during all experiments, as well as during image collection. Measurements of the flow rates for inspiration and expiration were supplied using non-contact MEMS airflow sensors (Omron D6F-50A-000) placed in line with the respective lines of the ventilator. A representative time trace of the ventilation signals is shown in Fig. 2.13.

Respiration phase is defined as the percentage of a respiration cycle complete, with zero phase corresponding to the beginning of inspiration. Estimation of respiration phase is done similar fashion to cardiac phase, where the start of inspiration is detected and

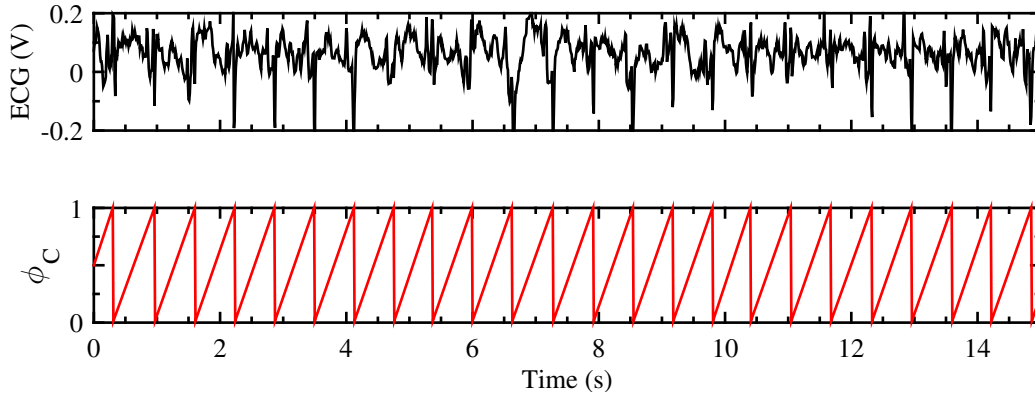


Figure 2.12: Cardiac phase is estimated from raw electrocardiogram (ECG) signal by detecting R-wave peaks in the signal. Cardiac phase is then defined as the percentage of a cycle completed.

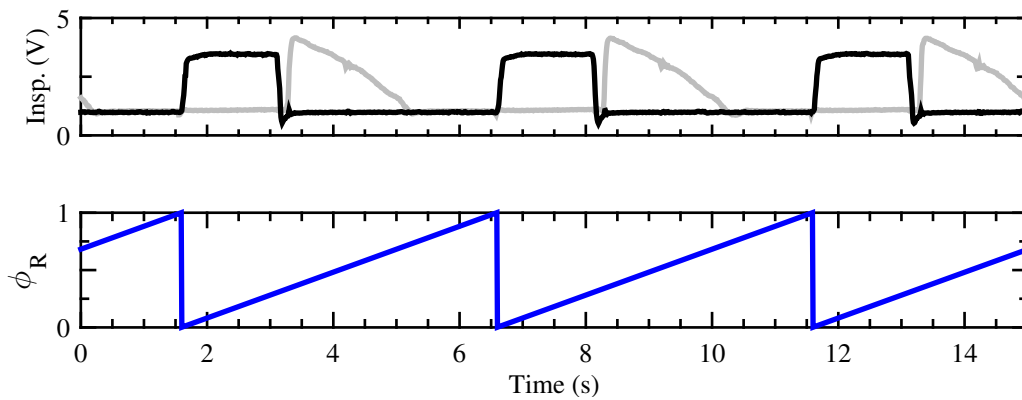


Figure 2.13: Respiration phase is estimated from respiration flow sensors by detecting the beginning of inspiration. Respiration phase is then defined as the percentage of a cycle completed.

we interpolate between successive detected starts of inspiration. The forced inspiration had approximately equal durations of inspiration, expiration, and dwell. Maximum lung volume then corresponds to a respiration phase of 0.3.

2.7.4 Fiducial Registration

After access to the heart is gained via the subxiphoid approach, and before the robot is placed on the surface of the heart, initial spatial registration between the patient and the heart model, T_0 , is estimated using the fiducials placed in the chest wall, shown in Fig. 2.11.

Using an electromagnetic tracking probe, the locations of the 9 markers are measured with respect to the reference probe. These measurements are then used with the locations of the markers in the map frame to solve for the rigid registration that aligns the point clouds. As the points are already matched, this transformation is easily solved using an SVD-based approach [43]. After the fiducial-based registration is solved, the robot is placed on the heart and the experiment is conducted.

2.7.5 Discussion

This section briefly outlined the pre- and intraoperative procedures used to perform live-animal experiments that are relevant to the collection of data used in the following chapters. Retrospectively gated cardiac CT imaging was done preoperatively for construction of anatomical surface models. The ground-truth cardiac phase corresponding to the image set can be estimated from image metadata, while ground-truth respiration phase for the image set is 0.3, corresponding to the end of inspiration. Robot pose measurements are referenced to a frame fixed to the chest wall of the pig, and cardiac phase and respiration phase are estimated from ECG and respiration sensor signals. Data collected in this fashion is used in the remainder of this thesis.

Part I

Virtual Image Guidance for Organ-Mounted Robots

Chapter 3

The Organ-mounted Robot

Registration Problem

In most virtual image guided systems registration consists of only the rigid transform which aligns the real and virtual space. This registration, which we refer to as *spatial registration*, provides full knowledge of the system. This is because this system can be described by a three-link closed kinematic chain. If we are given a measurement of the robot in the world frame, \mathbf{z} , and we know the ground-truth registration, \mathbf{T}^* , which aligns the maps, \mathcal{S} , with the actual surface, \mathcal{H} , then the location of the robot in the map frame is simply found by transforming the measurement by the rigid registration transformation, $\mathbf{T}^*\mathbf{z}$. The underlying assumption in this view is that the dimensionality of the map matches the dimensionality of the world, i.e., the static map represents a static organ. In the case of operating on the beating heart, this assumption does not hold.

3.1 Problem Formulation

The surface of the heart, as previously described, is a dynamic environment that undergoes periodic deformations due to both the contraction of the heart and respiration. If we assume

that the we have a function that describes the periodic motion of the surface of the heart,

$$\mathcal{H}(u, v, \phi_C, \phi_R), \quad (3.1)$$

then preoperative medical imaging provides a snapshot of the periodically deforming heart at an instant,

$$\mathcal{S}(u, v) = \mathbf{T}^* \mathcal{H}(u, v, \phi_C^*, \phi_R^*), \quad (3.2)$$

where u and v are coordinates describing a location on the surface, ϕ_C^* and ϕ_R^* are the ground-truth cardiac and respiration phases at the instant the images were taken, and \mathbf{T}^* is once again the ground-truth registration which aligns the map and image frames.

The second assumption is that if an organ-mounted robot remains stationary on the heart, it follows the path of the underlying point on the surface of the heart,

$$\mathcal{P}_i(\phi_C, \phi_R) = \mathcal{H}(u_i, v_i, \phi_C, \phi_R), \quad (3.3)$$

where \mathcal{P} is the function describing the path in 3D space the i^{th} point on the surface of the heart. This implies that the robots do not deform the surface of the heart, which, for HeartLander and Lamprey, we believe is a valid assumption. These robots are small and their connections to the outside world consist of very small, flexible wires.

Combining (3.2) and (3.3) provides the basis for the approach of registration for organ-mounted robots,

$$\mathcal{S}(u_i, v_i) = \mathbf{T}^* \mathcal{P}_i(\phi_C, \phi_R), \quad (3.4)$$

that the points on the surface of the map are given by the path of the robot at the instant the images used to create the map were captured. This view of registration for organ-mounted robots is equivalent to the case of a static world and static map if we only collect measurements at the ground-truth physiological phases. If the surface consisted of only a single periodic component this may be a reasonable approach, however, with multiple periodic components one could wait an arbitrarily long time before observing the correct phase combination.

Because of these periodic components to the deformation of the heart and the mismatch in dimensionality of the real world and the map, registration for organ-mounted robots requires knowledge of the physiological phases when the medical images were captured, which we refer to as *temporal registration*, as well as the rigid transformation that aligns the world and map at these phases, which we refer to as *spatial registration*. The work presented in the following three chapters is our approach to solving the *spatiotemporal* registration problem for organ-mounted robots, which we outline here.

Next we use a collection of learned periodic motion models to do rigid *spatial registration* in conjunction with *temporal registration*. This approach assumes the point cloud of periodic motion models is the same shape as the surface model at a specific instant. Identifying this instant is the temporal component of registration, and we refer to the combined estimation of spatial and temporal alignment *spatiotemporal registration*.

3.2 Approach

In order to solve the registration problem for organ-mounted robots, we first must be able to estimate or predict where the robot will be at the ground-truth physiological phases. Given a collection of measurements, $\{\mathbf{z}^{\phi_1}, \mathbf{z}^{\phi_2}, \dots, \mathbf{z}^{\phi_k}\}$, where \mathbf{z}^{ϕ_i} is a 6 degree-of-freedom pose of the robot at a particular set of phases, ϕ_i , we first learn frequency-based models which accurately describe the periodic motion of points on the surface of the heart, $\mathcal{P}(\cdot)$. Using these models, we can then predict where the robot will be at any phase, or, more importantly, at the ground-truth map phases, ϕ^* . We refer to the fitting of these frequency-based models to the periodic measurements of the robot on the surface of the heart as *physiological motion modeling*.

Next, using a collection of these periodic models, $\{\mathcal{P}_1(\cdot), \mathcal{P}_2(\cdot), \dots, \mathcal{P}_n(\cdot)\}$, the ground-

truth phases and rigid transformation which minimizes the registration error,

$$\sum_i (\mathcal{S}(\mathbf{u}_i) - \mathbf{T}\mathcal{P}_i(\phi))^2, \quad (3.5)$$

are estimated simultaneously. This estimation of parameters which aligns the real world and map, in both space and phase, is called *spatiotemporal registration*.

The previously described error function relies upon a matching metric which solves for the correspondence between a particular point $\mathcal{P}_i(\cdot)$ and the corresponding location in the map, \mathbf{u}_i . This correspondence we refer to as *localization*. Using the previously described methods for constructing models of the periodic motion of the heart and registration requires accurate models of the motion to provide accurate registration. Once accurate registration is achieved, however, waiting for sufficient measurements to learn accurate models of the motion wastes valuable time. The final piece of our contribution to virtual image guided surgery for organ-mounted robots poses localization as a function approximation problem which uses previously learned motion models to map directly heart surface in a single step.

3.3 Related Work

3.3.1 Physiological Motion Modeling

The vast majority of work on the modeling of the motion of the freely beating heart is in the area of active motion cancellation (AMC). AMC aims to provide a virtual stable operating platform to the surgeon by automatically moving robotically controlled tools in unison with the surface of the beating heart. Due to the large displacements and high velocities of the heart [23], feedforward controls are often implemented which rely on predictions of the future position of the surgical site. A wide variety of methods and measurement techniques has been used to provide these predictions, from which relevant work is discussed below. For further information readers are pointed to reviews of these methods [51, 52].

Several methods for prediction of motion of the heart do not attempt to fit models to the motion. Copies of previous measurements have been used for prediction [53–55]. Autoregressive models, in which future states are linear combinations of previous measurements, similarly eschew directly modeling the motion [56–60].

Approaches which attempt to fit predictive models to the periodic motion of the heart include the use of splines [61], but overwhelmingly use frequency-based models. Frequency-based models used have included single Fourier series [62, 63], dual Fourier Series [64–68], discrete Fourier transforms [69], amplitude-modulated Fourier series [51], and dual Fourier series with a quadratic coupling term [70].

Transformations were used to model the point motion of the heart in simulation in [71]. This work assumed that measurements of diaphragm position and cardiac phase were available and used a convolution of triangular basis functions to model the motion due to both heart contraction and respiration. This is the only work which attempts to model the orientation of the heart surface, but the technique was not demonstrated on real data, nor were measurement modalities presented which enable orientation measurements.

Measurement modalities used in the previous works include sonomicrometry [54–60, 70], stereo vision [53, 65–68], monocular vision [51, 61, 69], fiber-optic laser reflectance [64], and ultrasound [62, 63]. Each of these measurement modalities, excluding ultrasound, requires direct access to the heart through a sternotomy or thoracotomy, either to place sonomicrometry crystals or for direct line of sight for visual methods. While endoscopes may be used for imaging in minimally invasive procedures, the cramped space around the heart limits the ability of the camera to provide satisfactory views without requiring large access ports.

3.3.2 Surgical Registration

Methods for registering and localizing in and around the heart are highly dependent upon the instrument or robot being used. Tully et al. use an electromagnetic tracker located at the distal end of a highly articulated snake-like robot to estimate the shape of the robot using an extended Kalman filter framework [38]. If the pose of the robot is found to violate geometric constraints, namely intersecting the preoperative surface models, the registration and world frame localization parameters are updated using inequality- or equality-constrained Kalman filtering to project the system state into the feasible space [39, 72]. In the inequality-constrained case the model is assumed to be rigid, thereby restricting the robot to lie entirely out of the surface, while the equality-constrained case incorporates a stiffness model and force measurement to more accurately model the surface as a deformable body.

Therapies which target the endocardium using intracardiac echocardiographic (ICE) catheters use ultrasound images in conjunction with an electromagnetic tracker. One method generates a point cloud by extracting heart surface points from 2-dimensional ultrasound images at the catheter tip by rotating the catheter about its longitudinal axis. After sufficient points have been collected the point cloud is registered to the preoperative model of the left atrium using an iterative closest point (ICP) method to determine the pose of the catheter in the model frame directly [73]. The electromagnetic position measurements can then be used to determine registration.

Another method uses a particle filter to recursively estimate the map frame pose of the ICE catheter in the left atrium [40]. In this work the probability of a catheter tip pose is calculated by comparing virtual ultrasound images constructed from a preoperative model with the actual ultrasound images. The predicted catheter pose is then determined as the weighted sum of the particles and the registration parameters are then calculated using this pose estimate and measurements from an electromagnetic position tracker. Again the

use of ultrasound allows for directly estimating the map frame pose.

Chapter 4

Physiological Motion Modeling

This chapter is the first stage in addressing the registration and localization of organ-mounted robots on the beating heart. Although we have taken a vastly different approach to beating-heart surgery, the question we must first address is the same that has been addressed by some traditional approaches: how points move on the surface of the beating heart. The nature of our robots, however, enables us to address this question in ways which have yet to be explored.

The use of 6-degree-of-freedom (6-DOF) magnetic trackers and the subxiphoid approach means that this work is the first to use data from a closed-chest procedure as well as the first to address the orientation of the robot. Also, as these robots are mobile, data from the entire heart can be considered, as opposed to just a few points.

This chapter extends the amplitude-modulated (AM) Fourier series framework introduced by Bachta et al. [51] to model the periodic deformation of points on the surface of the heart in $SE(3)$. Careful consideration of the rotational model enables the periodic motion to be modeled in the same framework and optimized using a simple least squares solution. These models are then used to identify the best model for rotation, determine the optimal number of model parameters which limits overfitting and model size, and estimate the model parameters online.

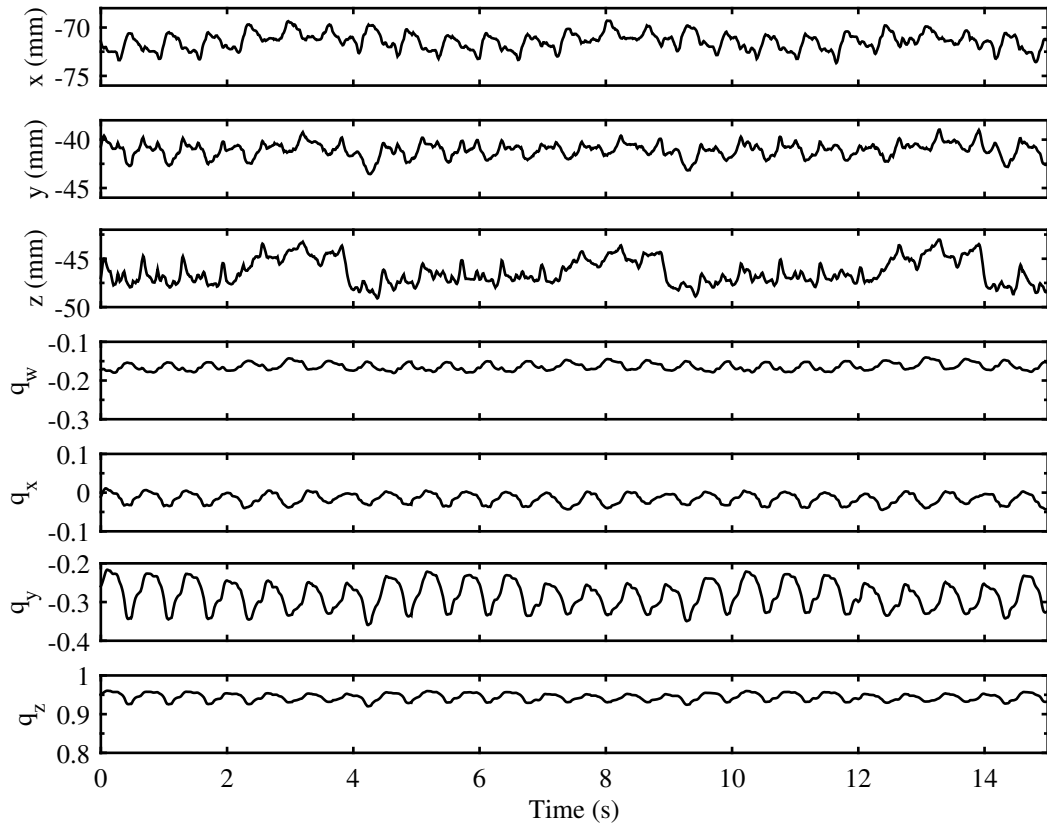


Figure 4.1: Position and orientation time traces of the Lamprey robot on the surface of the beating heart.

4.1 Analysis of Cardiac Motion

As previously noted by many researchers, the motion of points on the surface of the heart, shown in Fig. 4.1, is the combination of a low-frequency component due to respiration, and a high-frequency component due to heartbeat. These components can be seen clearly in the frequency response plots of both displacement, Fig. 4.2(a), and rotation, Fig. 4.2(b), where peaks in response due to respiratory motion are denoted with blue lines for the primary frequency through the fifth harmonic, and peaks in response due to the contraction of the heart are denoted with red dotted lines. A few prior works have also noted that significant peaks occur at integer combinations of the cardiac and respiration frequencies ($i\omega_C \pm j\omega_R$) [51]. These peaks, denoted by green dotted lines in Fig. 4.2, capture the effect of lung

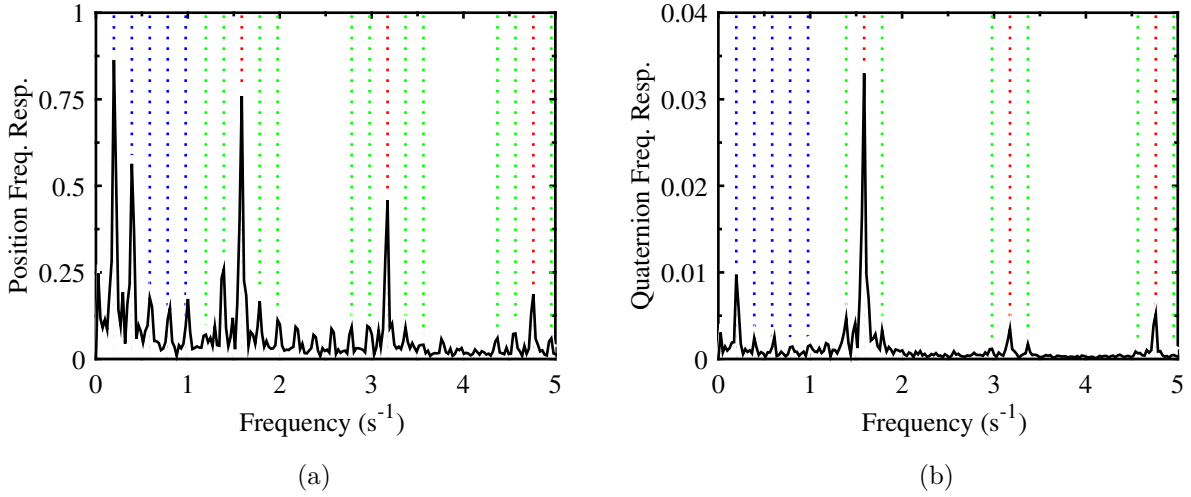


Figure 4.2: Frequency response for (a) translation and (b) rotation. Vertical blue lines correspond to harmonics of respiratory motion, red lines to heart contraction, and blue to the mixture of respiratory and cardiac motion.

volume on the contraction of the heart, namely that when the lungs are full the motion of the heart is constricted. Also, it is clear that there is significantly less power in the higher harmonics for rotation in comparison to translation.

4.2 Periodic Motion Modeling in \mathbb{R}^3

The amplitude-modulated (AM) Fourier series model used in this work, introduced by Bachta et al. [51], is an extension to dual Fourier series models for cardiac Cartesian point motion, which directly accounts for the coupling between cardiac and respiration motion. In this framework, the periodic Cartesian motion of a point, $\mathcal{P}(\phi_C, \phi_R)$, is modeled as the sum of a constant offset term, \mathbf{t}_0 , a low-frequency respiratory motion component, \mathcal{P}_R , a higher-frequency heartbeat motion component, \mathcal{P}_C , and a coupling term, \mathcal{P}_{CR} . This coupling term directly models the effect lung volume has on cardiac motion.

$$\mathcal{P}(\phi_C, \phi_R) = \mathbf{t}_0 + \mathcal{P}_R(\phi_R) + \mathcal{P}_C(\phi_C) + \mathcal{P}_{CR}(\phi_C, \phi_R) \quad (4.1)$$

$$\mathcal{P}_R = \sum_{i=1}^{H_R} \mathbf{a}_i \sin(i\phi_R) + \mathbf{b}_i \cos(i\phi_R) \quad (4.2)$$

$$\mathcal{P}_C = \sum_{i=1}^{H_C} \mathbf{c}_i \sin(i\phi_C) + \mathbf{d}_i \cos(i\phi_C) \quad (4.3)$$

$$\begin{aligned} \mathcal{P}_{CR} = & \sum_{i=1}^{H_{MC}} \sum_{j=1}^{H_{MR}} \mathbf{e}_{ij} \sin(i\phi_C - j\phi_R) + \mathbf{f}_{ij} \cos(i\phi_C - j\phi_R) \\ & + \mathbf{g}_{ij} \sin(i\phi_C + j\phi_R) + \mathbf{h}_{ij} \cos(i\phi_C + j\phi_R) \end{aligned} \quad (4.4)$$

where \mathbf{a} , \mathbf{b} , \mathbf{c} , \mathbf{d} , \mathbf{e} , \mathbf{f} , \mathbf{g} , and \mathbf{h} are Fourier series parameters, and H_R , H_C , H_{MC} , and H_{MR} are the number of respiration, cardiac, and coupled cardiac and respiration harmonics, respectively, to consider. The number of parameters in this model per degree of freedom of the signal is a function of the number of harmonics used.

$$\mathbf{N} = 1 + 2H_R + 2H_C + 4H_{MC}H_{MR} \quad (4.5)$$

This model possesses several attributes that warrant its use, aside from being shown to outperform other approaches [51]. First, it directly models the coupling between cardiac and respiration motion, which has significant effect in closed-chest procedures. Also, as we have measurements for both cardiac and respiration phase, the model is linear, can be expressed in matrix form as follows, and can be easily solved using a least-squares approach.

$$\mathcal{P}(\phi_C, \phi_R) = \mathbf{W}^T \boldsymbol{\varphi} \quad (4.6)$$

$$\mathbf{W} = \begin{bmatrix} \mathbf{t}_0^T \\ \left[\begin{array}{c} \mathbf{a}_i^T \\ \mathbf{b}_i^T \end{array} \right]_{i=1, \dots, H_R} \\ \left[\begin{array}{c} \mathbf{c}_i^T \\ \mathbf{c}_i^T \end{array} \right]_{i=1, \dots, H_C} \\ \left[\begin{array}{c} \mathbf{e}_{ij}^T \\ \mathbf{f}_{ij}^T \\ \mathbf{g}_{ij}^T \\ \mathbf{h}_{ij}^T \end{array} \right]_{\substack{i=1, \dots, H_C \\ j=1, \dots, H_R}} \end{bmatrix} \quad \varphi = \begin{bmatrix} 1 \\ \left[\begin{array}{c} \sin(i\phi_R) \\ \cos(i\phi_R) \end{array} \right]_{i=1, \dots, H_R} \\ \left[\begin{array}{c} \sin(i\phi_C) \\ \cos(i\phi_C) \end{array} \right]_{i=1, \dots, H_C} \\ \left[\begin{array}{c} \sin(i\phi_C - j\phi_R) \\ \cos(i\phi_C - j\phi_R) \\ \sin(i\phi_C + j\phi_R) \\ \cos(i\phi_C + j\phi_R) \end{array} \right]_{\substack{i=1, \dots, H_C \\ j=1, \dots, H_R}} \end{bmatrix} \quad (4.7)$$

4.3 Parameterizations of 3-D Rotation

A major contribution of the work presented in this chapter is the modeling of periodic rotational motion. Application of the previously described amplitude-modulated Fourier series model to rotation, however, requires careful consideration of the representation used. The major issue we wish to investigate is the effect of optimizing over the Euclidean distance metric in each parameterization. This section summarizes the parameterizations considered in the remainder of the chapter as well as distance metrics in this space. The space of rotations in 3 dimensions is given by:

$$SO(3) = \{ \mathbf{R} \in \mathbb{R}^{3 \times 3} : \mathbf{R}\mathbf{R}^T = I, \det \mathbf{R} = 1 \}. \quad (4.8)$$

Rotation matrices, \mathbf{R} , use nine scalars to describe three degrees of freedom, requiring the enforcement of 6 constraints. The standard distance metric in this space is the geodesic distance,

$$d_G(\mathbf{R}_1, \mathbf{R}_2) = \frac{1}{\sqrt{2}} \|\log(\mathbf{R}_1^{-1}\mathbf{R}_2)\|_F, \quad (4.9)$$

which does not lend itself to simple optimization techniques. The following are three alternative parameterizations we will consider.

4.3.1 Unit Quaternions

Unit quaternions are the extension of the complex numbers to rotations. The quaternion corresponding to a rotation angle, θ , about an axis, $\hat{\mathbf{u}}$, is given by

$$\mathbf{q} = \begin{bmatrix} q_w \\ q_x \\ q_y \\ q_z \end{bmatrix} = \begin{bmatrix} q_w \\ \mathbf{q}_v \end{bmatrix} = \begin{bmatrix} \cos \frac{\theta}{2} \\ \hat{\mathbf{u}} \sin \frac{\theta}{2} \end{bmatrix}, \quad (4.10)$$

where $\|\mathbf{q}\| = 1$. The rotation matrix corresponding to the quaternion rotation, \mathbf{q} , is given by:

$$\mathbf{R}(\mathbf{q}) = \mathbf{I} + 2q_w \widehat{\mathbf{q}}_v + 2\widehat{\mathbf{q}}_v^2 \quad (4.11)$$

where the $\widehat{\cdot}$ operator maps vector $\mathbf{v} \in \mathbb{R}^3$ to $so(3)$.

$$\widehat{\mathbf{v}} = \begin{bmatrix} 0 & -v_z & v_y \\ v_z & 0 & -v_x \\ -v_y & v_x & 0 \end{bmatrix} \quad (4.12)$$

Once again the unit norm constraint of this representation requires four parameters to describe three degrees of freedom. Quaternions are more space-efficient than rotation matrices and allow directly for manipulation using the quaternion multiplication operator. The geodesic distance between quaternions takes a much simpler form than that for rotation matrices.

$$d_G(\mathbf{q}_1, \mathbf{q}_2) = 2 \cos^{-1} |\mathbf{q}_1 \cdot \mathbf{q}_2| \quad (4.13)$$

An alternative distance metric on unit quaternions which is functionally and boundedly equivalent to the geodesic distance is the Euclidean distance [74]. Because quaternions double-cover the space of rotations, $-\mathbf{q}$ and \mathbf{q} represent equivalent rotations, which must be accounted for in the metric.

$$d_q(\mathbf{q}_1, \mathbf{q}_2) = \min(\|\mathbf{q}_1 - \mathbf{q}_2\|, \|\mathbf{q}_1 + \mathbf{q}_2\|) \quad (4.14)$$

4.3.2 Exponential Coordinates

In exponential coordinates, a rotation of an angle, θ , about an axis, $\hat{\mathbf{u}}$, is given by

$$\boldsymbol{\omega} = \theta \hat{\mathbf{u}}. \quad (4.15)$$

The skew-symmetric matrix, $\hat{\boldsymbol{\omega}} \in so(3)$, is the Lie algebra of the rotation group, and the rotation matrix corresponding to the rotation $\boldsymbol{\omega}$ is found using the exponential map.

$$\begin{aligned} \mathbf{R}(\boldsymbol{\omega}) &= e^{\hat{\boldsymbol{\omega}}} \\ &= \mathbf{I} + \frac{\hat{\boldsymbol{\omega}}}{\|\boldsymbol{\omega}\|} \sin \|\boldsymbol{\omega}\| + \frac{\hat{\boldsymbol{\omega}}^2}{\|\boldsymbol{\omega}\|^2} (1 - \cos \|\boldsymbol{\omega}\|) \end{aligned} \quad (4.16)$$

Exponential coordinates are a minimal state representation, and as such have discontinuities in the space. For this work we choose to center the space at 0 and place this discontinuity at $\pm\pi$. Also, the Euclidian distance in this space is not functionally equivalent to the geodesic distance.

4.3.3 Euler Angles

The final parameterization considered is the Euler angle representation. This family of rotations is parameterized as three successive rotations about a set of three axes. There are 24 different conventions of this form due to the non-commutativity of rotations, an exhaustive list of which can be found in [75].

This work uses Z - Y - X , or yaw-pitch-roll, Euler angles. In this parameterization the relative pose of two frames is defined by rotating an angle, α , about the z -axis, then rotating an angle, β , about the rotated y -axis, and finally rotating an angle, γ , about the rotated

x -axis. The rotation matrix corresponding to this rotation is constructed as follows.

$$\begin{aligned}
\mathbf{R}(\alpha, \beta, \gamma) &= \mathbf{R}(\alpha) \mathbf{R}(\beta) \mathbf{R}(\gamma) \\
&= \begin{bmatrix} c_\alpha & -s_\alpha & 0 \\ s_\alpha & c_\alpha & 0 \\ 0 & 0 & 1 \end{bmatrix} \begin{bmatrix} c_\beta & 0 & s_\beta \\ 0 & 1 & 0 \\ -s_\beta & 0 & c_\beta \end{bmatrix} \begin{bmatrix} 1 & 0 & 0 \\ 0 & c_\gamma & -s_\gamma \\ 0 & s_\gamma & c_\gamma \end{bmatrix} \\
&= \begin{bmatrix} c_\alpha c_\beta & c_\alpha s_\beta s_\gamma - s_\alpha c_\gamma & c_\alpha s_\beta c_\gamma + s_\alpha s_\gamma \\ s_\alpha c_\beta & s_\alpha s_\beta s_\gamma + c_\alpha c_\gamma & s_\alpha s_\beta c_\gamma - c_\alpha s_\gamma \\ -s_\beta & c_\beta s_\gamma & c_\beta c_\gamma \end{bmatrix} \tag{4.17}
\end{aligned}$$

Again, as this is a minimal state representation, it possesses drawbacks which must be managed, including gimbal lock and non-uniqueness of rotations. Also, the Euclidean distance in this space is not functionally equivalent to the geodesic distance.

4.3.4 Converting Between Parameterizations

Converting between representations is necessary throughout this work. We will use the following notation to indicate mapping the representation of a rotation from parameterization a to b .

$$\mathcal{M}_a^b(\cdot): a \mapsto b \tag{4.18}$$

The mappings from each of the three representations to rotation matrices are given by Eqs. (4.11,4.16,4.17).

4.4 Periodic Motion Modeling in $SO(3)$

The choice of representation of 3-D rotation for this application requires weighing how 3-D rotations will fit into the existing AM Fourier series framework. Due to the topology of the space, no representations will exactly fit into the existing framework; however, we present

models for the three which come the closest: unit quaternions, exponential coordinates, and Euler angles.

4.4.1 Direct Quaternion Model

The direct application of the AM framework to rotation simply treats quaternions as vectors in \mathbb{R}^4 .

$$\mathcal{Q}(\phi_C, \phi_R) = \mathbf{W}_{\mathbf{q}}^T \boldsymbol{\varphi} \quad (4.19)$$

As the quaternion is modeled as the sum of vectors, no steps are taken to enforce unit length constraints. To return a unit quaternion the evaluated vector can simply be normalized. As previously discussed in Section 4.3, while the Euclidean distance is a proper distance metric on unit quaternions, because the quaternions double-cover the space, i.e., $d(\mathbf{q}, -\mathbf{q}) = 0$, special care must be taken when using this model. Enforcing smoothness in the representation can be done simply to ensure that jumps in representation do not occur.

$$\mathbf{q}(k) = \begin{cases} \mathbf{q}(k) & \text{if } \|\mathbf{q}(k-1) - \mathbf{q}(k)\| \leq \sqrt{2} \\ -\mathbf{q}(k) & \text{if } \|\mathbf{q}(k-1) - \mathbf{q}(k)\| > \sqrt{2} \end{cases} \quad (4.20)$$

4.4.2 Intermediate Frame Models

Exponential coordinates and Euler-angles parameterizations require modification of the model due to the fact that exponential coordinates have a discontinuity at $\pm\pi$, and Euler representation possesses singularities when $\beta = \pm\frac{\pi}{2}$, and we wish to represent arbitrary rotations which may cross these boundaries. The solution to this problem is to place the discontinuities opposite the current operating point. This is done by defining an intermediate rotation, $\mathbf{q}_{\text{H}}^{\text{P}}$, defined as the average rotation.

$$\mathbf{q}_{\text{H}}^{\text{P}} = \underset{\mathbf{q}}{\operatorname{argmin}} \sum_{i=1}^N d(\mathbf{q}, \mathbf{q}_{\text{H}}^{\text{P}}(i))^2 \quad (4.21)$$

If we can estimate this value, then the remaining periodic rotation, $\mathbf{q}_{\bar{\mathbb{H}}}$, is centered about the origin. We can then model this zero-mean periodic rotation using any of the three representations of rotation.

$$\begin{aligned}\mathcal{Q}(\phi_C, \phi_R) &= \mathbf{q}_{\bar{\mathbb{H}}}^{\text{P}} \otimes \mathbf{q}_{\bar{\mathbb{H}}}^{\bar{\mathbb{H}}}(\phi_C, \phi_R) \\ &= \mathbf{q}_{\bar{\mathbb{H}}}^{\text{P}} \otimes \mathbf{W}_{\bar{\mathbf{q}}}^T \boldsymbol{\varphi}\end{aligned}\tag{4.22}$$

$$= \mathbf{q}_{\bar{\mathbb{H}}}^{\text{P}} \otimes \mathcal{M}_{\omega}^{\mathbf{q}}(\mathbf{W}_{\omega}^T \boldsymbol{\varphi})\tag{4.23}$$

$$= \mathbf{q}_{\bar{\mathbb{H}}}^{\text{P}} \otimes \mathcal{M}_e^{\mathbf{q}}(\mathbf{W}_e^T \boldsymbol{\varphi})\tag{4.24}$$

Using either exponential coordinates or Euler angles in this form is desirable as they both are vectors in \mathbb{R}^3 and as such do not require enforcement of unity constraints; however, the Euclidean distance is not a proper distance metric in the space of rotations. Of the four models for rotation presented in (4.19), (4.22), (4.23), and (4.24), there is no clear optimal choice.

4.5 Intermediate Frame Translation Model

As three of the presented models for rotation model the rotation in the average rotation frame, we may wish to model the periodic deformation in the same reference frame. The standard model for translational motion is

$$\mathcal{P}(\phi_C, \phi_R) = \mathbf{W}_{\bar{\mathbf{t}}}^T \boldsymbol{\varphi}.\tag{4.25}$$

Defining the mean position as

$$\mathbf{t}_{\bar{\mathbb{H}}}^{\text{P}} = \underset{\mathbf{q}}{\operatorname{argmin}} \sum_{i=1}^N \|\mathbf{t} - \mathbf{t}_{\bar{\mathbb{H}}}^{\text{P}}(i)\|^2,\tag{4.26}$$

the periodic model in the transformed frame can be defined as

$$\mathcal{P}(\phi_C, \phi_R) = \mathcal{M}_{\bar{\mathbf{q}}}^{\mathbf{R}}(\mathbf{q}_{\bar{\mathbb{H}}}^{\text{P}}) \mathbf{W}_{\bar{\mathbf{t}}}^T \boldsymbol{\varphi} + \mathbf{t}_{\bar{\mathbb{H}}}^{\text{P}}.\tag{4.27}$$

Combining (4.25) and (4.27), and noting that $\mathbf{t}_{\mathbb{H}}^{\mathbb{P}}$ is equivalent to the \mathbf{t}_0 component of $\mathbf{W}_{\mathbf{t}}$, it is clear that the parameters in the rotated frame are equivalent to rotating the base-frame parameters by the mean rotation.

4.6 Model Parameter Estimation

Parameters for each model can be estimated using ordinary least squares in an offline batch process, or alternatively in a recursive manner for online implementation. The ordinary least squares solution is simply found using the pseudo-inverse:

$$\mathbf{W} = \Phi^\dagger \mathbf{S} \quad (4.28)$$

$$\Phi = \begin{bmatrix} \varphi(1)^T \\ \vdots \\ \varphi(n)^T \end{bmatrix}, \mathbf{S} = \begin{bmatrix} \mathbf{s}(1)^T \\ \vdots \\ \mathbf{s}(n)^T \end{bmatrix} \quad (4.29)$$

where \mathbf{s} is the signal being fitted. For the standard quaternion and translation in the base frame this signal is simply the measurement vector. However, for the models in the mean frame, we must first estimate the mean, then transform the measurement vectors into the desired parameterization, as shown below for the exponential coordinate parameterization.

$$\mathbf{s} = \mathcal{M}_{\mathbf{q}}^\omega(\mathbf{q}_{\mathbb{H}}^{\mathbb{P}-1} \otimes \mathbf{q}_{\mathbb{H}}^{\mathbb{P}}) \quad (4.30)$$

Online estimation of the parameters follows a similar process. In the case of the base-frame models all parameters can be estimated in a single stage, whereas the mean-frame models require a multistage approach. This two-stage approach, shown in Fig. 4.3, first uses a simple moving-average filter to estimate the mean of the signal, which is then used to transform the input signal. The transformed signal is then mapped to the proper parameterization, and then fit using recursive least squares.

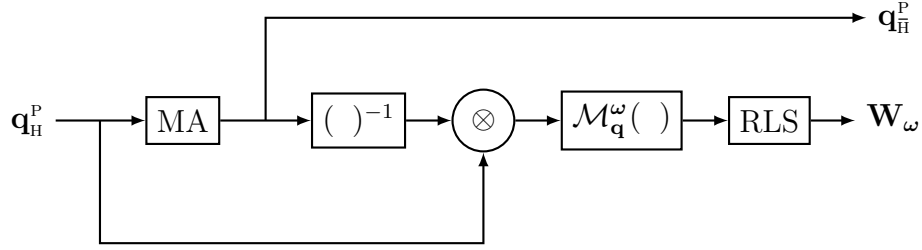


Figure 4.3: Online estimation scheme for exponential parameterization of rotation. The average rotation is first estimated using a moving average filter. The measurement is then transformed by the mean rotation, converted from quaternion to exponential coordinates, and fit using recursive least squares.

4.7 Experiments

This section describes the experiments conducted retrospectively on data collected during a live-animal closed-chest beating-heart procedure using the methods described in Section 2.7. The Lamprey robot was used to collect ~ 100 thirty-second time traces while attached to the beating heart. Virtual image guidance was used to guide uniform coverage of the heart.

4.7.1 Rotation Model Comparison

The purpose of this experiment is to determine the effects of the different distance metrics and nonlinear mappings between representations on the relative quality of the fit provided by each of the four models presented for periodic rotation. The numbers of harmonics used in each model were $H_C = 5$, $H_R = 4$, $H_{MC} = 2$, and $H_{MR} = 1$. Each model was fit to a time trace approximately 30 s in length using ordinary least squares. The learned weights were then used to generate predicted measurements for the entire time trace.

For the two models that operate directly on quaternions the lengths of the predicted quaternions before normalization were calculated. RMS error was then calculated over the entire trace for each model relative to the quaternion measurements as well as between prediction models. Geodesic distance given by Eq. (4.13) was used to compute error.

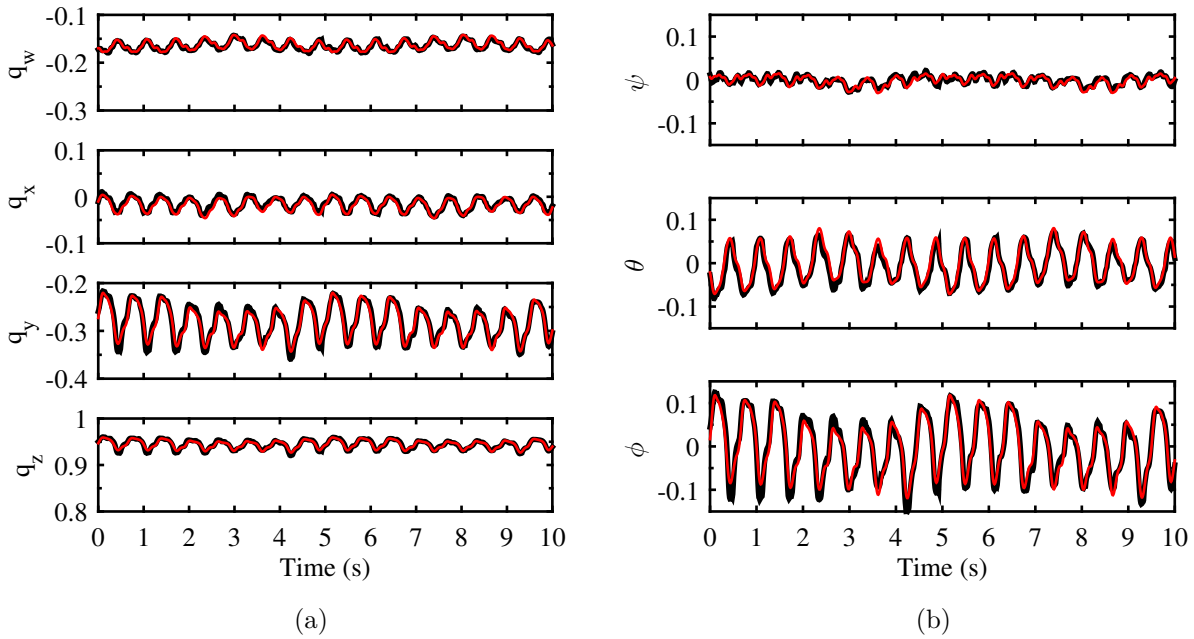


Figure 4.4: Offline estimation of periodic rotation using (a) quaternion representation and (b) Euler angle representation. Each model to 30 s of data, shown in black, and the learned parameters were then used to generate predicted measurements, shown in red.

Offline estimation performance for a portion of the 30 s of periodic rotation using the quaternion and Euler angle parameterizations are shown in Fig. 4.4. The resulting errors from each model are virtually identical. For the quaternion-based models the lengths of the unnormalized quaternions were notably close to unit length, having maximum and minimum lengths of 1.0006 and 0.9996. RMS errors between each of the prediction models, as well as the ground truth data, are shown in Table 4.1. Each of the models had RMS prediction error of 0.016 radians ($\approx 0.9^\circ$). Looking at the RMS errors of the model predictions with each other, of which the largest is 3.1×10^{-4} ($\approx 0.02^\circ$) shows that for the range of rotations the robot experiences on the heart these four models are essentially equivalent, with the exponential and Euler-based models using far fewer parameters to achieve the same predictions.

Table 4.1: Orientation Relative Prediction Error

	\mathbf{q}	$\bar{\mathbf{q}}$	$\boldsymbol{\omega}$	\mathbf{e}
Data	0.016	0.016	0.016	0.016
\mathbf{q}		2.5×10^{-9}	1.2×10^{-5}	3.1×10^{-4}
$\bar{\mathbf{q}}$			1.2×10^{-5}	3.1×10^{-4}
$\boldsymbol{\omega}$				3.1×10^{-4}

Entries are RMS prediction difference (radians) between the presented models for periodic rotation where \mathbf{q} refers to Eq. (4.19), $\bar{\mathbf{q}}$ is Eq. (4.22), $\boldsymbol{\omega}$ is Eq. (4.23), and \mathbf{e} is Eq. (4.24).

4.7.2 Model Fidelity

Experiments were conducted to select the model order which best describes the underlying dynamics of the periodic motion realized by the robot over the entire heart. In order to address this question, the 100 time traces collected over the surface of the heart were fitted with each of the proposed models using a varying range of harmonics.

For each test the first 80% of the time traces, approximately 25 s or 5 respiration cycles, was used to train the models. These models were then tested on the remaining 20% of data, approximately 5 s or 1 respiration cycle. RMS error for both training and testing was recorded, with the distance metric used for rotation being the geodesic distance, and combined across all points to get a single error for each model and set of harmonics. Each model was then classified by the total number of parameters required by the model, and the model with the smallest error for each number of parameters was identified.

In order to limit the space of models, as well as to keep the respiration and cardiac harmonics from interfering with each other, the numbers of harmonics were capped at $H_C = 7$, $H_R = 6$, $H_{MC} = 7$, and $H_{MR} = 3$.

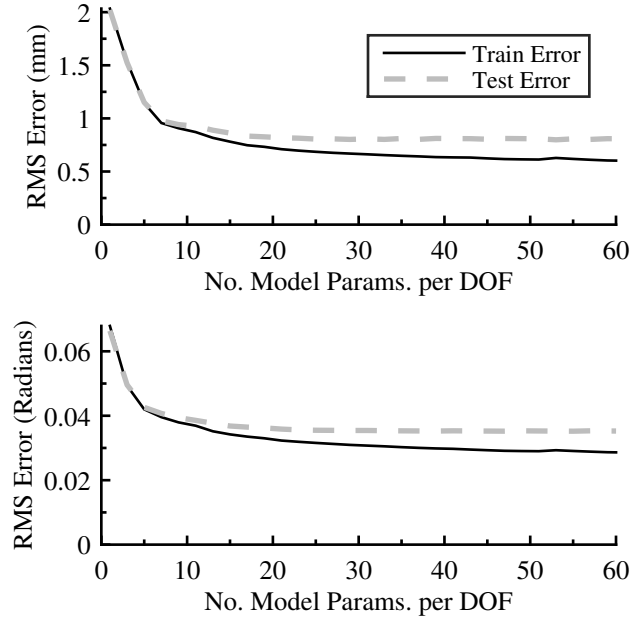


Figure 4.5: Training and test errors vs. number of model parameters per degree of freedom for (top) translational models, and (bottom) rotational models. Geodesic distance is used as the distance metric for rotations.

Training and test errors for translational and rotational models averaged across all points are shown in Fig. 4.5. Errors are plotted against the number of parameters per degree of freedom of the parameterization, meaning the same model order in exponential coordinates requires a quarter fewer parameters than using quaternions.

The results show that although the fit of the training models improves with model order, the predictive ability of the models improves little past the use of 20 parameters. Prediction error is essentially halved for the best model orders, decreasing from 2.0 mm and 0.07 radians for a constant (zeroth-order) model to a minimum of 0.8 mm and 0.035 radians. The results also show that predictive ability does not degrade at higher model orders.

From these results, we can generate an ordered list of models indicating the numbers of harmonics that provide the best performance for a particular model order, as shown in

Table 4.2: Preferred Model List

\mathbf{N}^a	3	5	7	9	11	13	15	17	19	21
H_C	0 / 1 ^b	1	1 / 2	2	3	2	2 / 3	3	4	3
H_R	1 / 0	1	2 / 1	2	2	2	3 / 2	3	3	3
H_{MC}	0	0	0	0	0	1	1	1	1	1
H_{MR}	0	0	0	0	0	1	1	1	1	2

^a Number of parameters per model DOF from Eq. (4.5).

^b Multiple entries denote different preferences for rotation and translation.

Table 4.2. While the numbers of harmonics for translation and rotation generally agree, there are a few differences. These differences show how the contributions of motion differ between the cardiac and respiratory components of motion.

4.7.3 Online Estimation and Prediction

Experiments were also conducted in order to demonstrate the ability to estimate these model parameters online. The cascaded filter estimation scheme was used to estimate the model parameters for exponential representation of rotation and translation. The goal of this study was to demonstrate the ability of the presented scheme to provide stable estimates of the model parameters, to characterize the time required to learn the model, and to determine the prediction accuracy.

Once again the 100 time traces collected over the surface of the heart were fit using the described model and online algorithm. Initial estimates for all parameters were set to 0. The moving-average filter used a window length of 500 samples, or approximately 5 s, while the RLS algorithm used a forgetting factor of 0.995.

At each time step, after the online algorithm updated the model parameters, the current model was used to predict the motion for the next 5 secs. RMS errors of these predictions

were then calculated and combined over the points to get RMS prediction error over the entire heart as a function of time.

An example of the predictive performance of the translational and exponential models using online estimation is shown in Fig. 4.6. These plots show the evolution of the estimate of the means up to the current filter iteration, beyond which the current model is projected forward in time. Fourier series parameter values for one degree of freedom are shown in Fig. 4.7 over the entire run. These figures demonstrate the feasibility of estimating these parameters in an online manner.

Inspection of both the estimates of the means and the parameter values show that the estimation of the mean requires approximately 5 s, the length of a respiration cycle, to converge to a steady value, while the Fourier series parameters require approximately another 2 respiration cycles to completely settle. From this point onwards, the parameter values do not vary significantly, meaning the model has converged.

Once again, combining the results over all 100 points over the surface of the heart yields the RMS prediction error for 5 s prediction horizons, as shown in Fig. 4.8. There are two important things to note about these plots. First is the rise in error which occurs at 5 s. This increase in error corresponds to the length of a full respiration cycle and is due to changes in the parameter estimates which occur due to the convergence of the mean estimates. While not starting the parameter estimation until after the mean has settled will avoid this bump, it was found to not significantly affect performance. Secondly, the prediction errors for both translation and rotation reach approximately the same minimum values as the offline experiments: 0.8 mm and 0.035 radians RMS. These minimum values are reached at approximately 15 seconds and do not vary significantly for the remainder of the run.

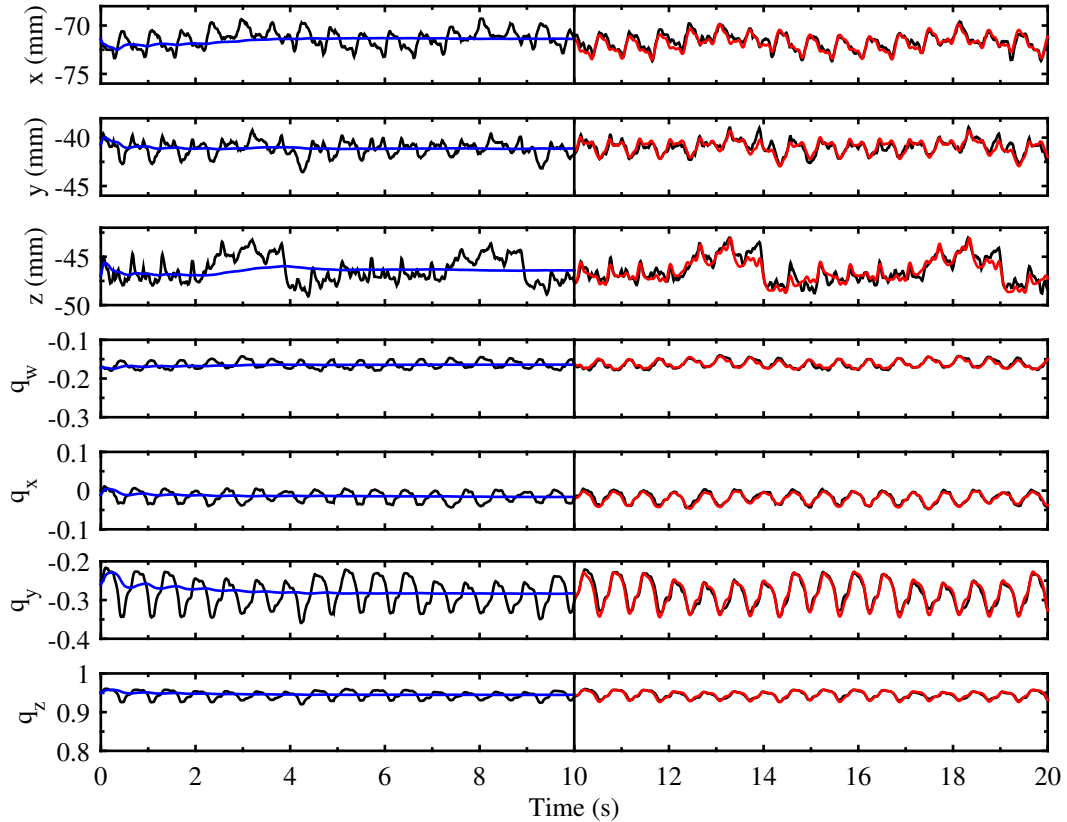


Figure 4.6: Online estimation and prediction results for translation and rotation. In each plot the ground truth measurements are shown in black. The current filter time step is denoted by the vertical black line. Blue lines show the evolution of the estimate of the signal means, while the projection of the current model forward in time is shown in red.

4.8 Discussion

This chapter deals with the problem of accurately modeling the quasi-periodic motion of the beating heart as it pertains to organ-mounted robots. Due to the unique nature of these robots we were able to address this motion with data collected from a live-animal closed-chest procedure, over all areas of the heart, with orientation as well as position measurements.

The framework used as the groundwork for modeling is the amplitude-modulated

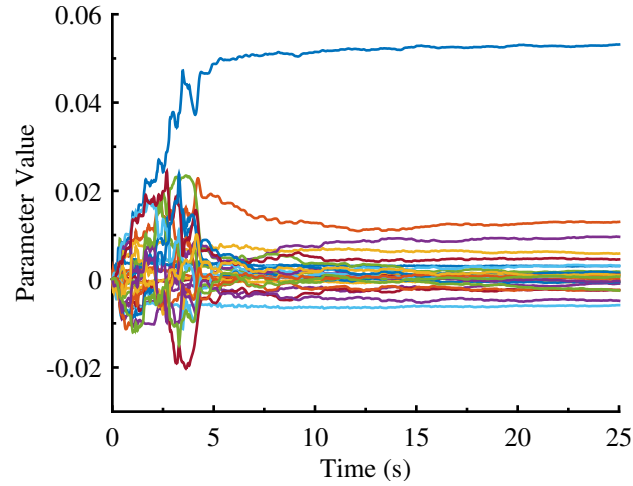


Figure 4.7: Model parameter values evolution during online estimation. Parameter values change vary significantly until the mean estimates converge at 5 s.

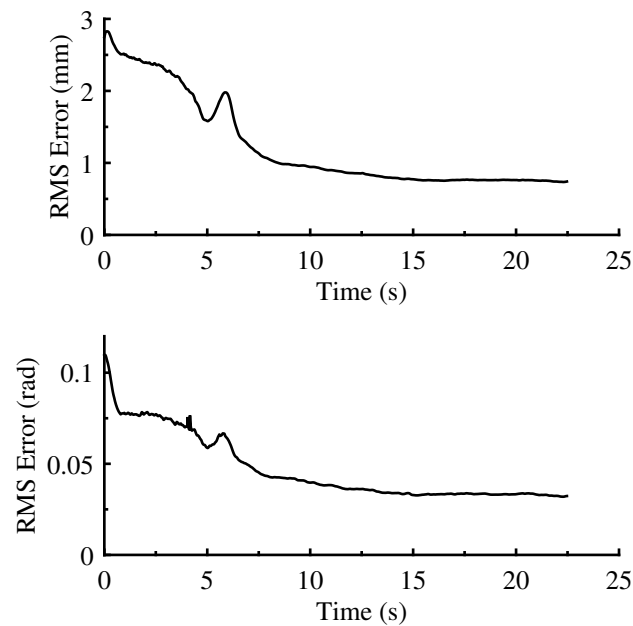


Figure 4.8: Online estimation and prediction global error for (top) translation and (bottom) rotation. Error is calculated over a 5 s prediction horizon and averaged across all points.

Fourier series, which was first introduced in [51]. This model had previously been shown to outperform other model-based motion-prediction schemes. It directly models the coupling seen between cardiac and respiratory motion, and can be optimized easily using a least

squares approach.

Four models using three different parameterizations of rotation—unit quaternions, exponential coordinates, and Euler angles—were presented as candidates for describing the periodic rotational motion of the heart. Each model possessed some non-ideality which made its suitability questionable. Quaternions have constraints on length. Exponential coordinates and Euler angles have discontinuities and the Euclidean distance in these parameterizations is not a proper distance metric on $SO(3)$. Comparison of the models, however, showed that, for the relatively small rotations seen in the data, the models are essentially equivalent. With rotations that are near zero, the Euclidean distance metrics are suitable for optimization on these parameterizations. The only practical difference in the models is that the exponential and Euclidean parameterizations provide essentially the same results with a quarter fewer model parameters.

The remainder of the work presented in this chapter should be viewed from the very specific application of this work relative to other related works. The goal of these models is not to predict where a point will be in a short time as accurately as possible, but rather to describe where the point will be at all times as accurately as possible. This goal, which uses error metrics which cover long durations of time over all areas of the heart lead us to the conclusion that a large number of harmonics does not improve prediction performance in general. Whereas other works have used as many as 13, 6, 7, and 2 cardiac, respiration, and coupled cardiac and respiration harmonics to predict the motion of the heart [51], for this specific application we found no benefit from using any more than 3, 3, 1 and 2 cardiac, respiration, and coupled cardiac and respiration harmonics, respectively. Likely reasons for these differences in findings include measurement frequency and noise characteristics, measurement modalities, and most importantly the fact that our data was from a closed-chest procedure, introducing many more sources for non-idealities.

The final contribution of this chapter is the demonstration of the online estimation of

the presented models. These online methods achieved errors comparable to those found using offline methods. While an argument could be made for using a filtering approach to fitting the model, our argument for the least squares approach is twofold. As the best model found in this work consists of 127 parameters, if we wish the filter to be adaptive, as it is currently, assigning meaningful transition uncertainties is difficult, rendering the uncertainties which the system outputs difficult to make use of. Secondly, the estimation scheme produces satisfactory results and requires only two parameters to be identified, both of which have physical meaning.

Chapter 5

Spatiotemporal Registration

The efficacy of virtual image guidance relies almost entirely on the ability to present the clinician an accurate representation of the state of the surgery. This quality of representation relies directly on having accurate anatomical models, precise position measurements, and the accurate alignment of these two sources of information. This alignment, called *registration*, poses a unique challenge for our organ-mounted robotic system.

ECG-gated cardiac CT images, used to construct surface models, provide only a snapshot of the operating environment. Our robots, however, provide measurements of the heart which is under continuous motion. The task of registration then is to align our model and measurements *temporally* as well as *spatially*. This chapter presents our efforts in *spatiotemporal* registration.

Section 5.1 formally defines the problem and demonstrates the failure of a global optimization approach. The remainder of the chapter presents our efforts in circumventing this failure to provide a method for temporal registration which minimizes the magnitude of the resulting registration.

5.1 Problem Formulation

The problem we are addressing in this work is the standard registration problem—aligning two point clouds—with the added complication of one of the sets being periodic, and is shown diagrammatically in Fig. 5.1. Registration is defined as

$$\mathcal{S}(\mathbf{u}_i) = \mathbf{R}^* \mathbf{p}_i^{\phi^*} + \mathbf{t}^*, \quad (5.1)$$

where

$$\mathbf{p}_i^{\phi^*} = \mathcal{P}_i(\phi_C^*, \phi_R^*), \quad (5.2)$$

\mathcal{S} is the surface mesh of the heart, \mathbf{u}_i are the map coordinates of the point on the surface, \mathcal{P}_i is the function defining the trajectory of the the i^{th} point, ϕ_C^* and ϕ_R^* are the ground truth cardiac and respiration phases of our map, and \mathbf{R}^* and \mathbf{t}^* are the rigid rotation and translation which align $\mathcal{S}(\mathbf{u}_i)$ and $\mathbf{p}_i^{\phi^*}$.

This formulation assumes that the spatial registration is a rigid transformation. Assuming a rigid transform means the robots do not deform the surface of the heart and that the set of poses of the robot at the image phases, $\{\mathbf{p}_1^{\phi^*}, \mathbf{p}_2^{\phi^*}, \dots\}$, is the same shape as the map. We believe this assumption is justified due to the small form factors of the robots.

If the ground truth image phases are known, the spatial registration parameters can be found using an iterative closest point (ICP) method [47] which minimizes the following distance function:

$$\mathbf{T}^* = \underset{\mathbf{T}}{\operatorname{argmin}} \sum_i \left(\mathcal{S}(\mathbf{u}_i) - \mathbf{T} \mathbf{p}_i^{\phi^*} \right)^2 \quad (5.3)$$

where we have combined rotation and translation into a rigid transformation, \mathbf{T}^* , and assumed homogenous coordinates for \mathbf{p} .

If the imaging modality used to construct the anatomical models used a gating technique, it is reasonable to assume that the cardiac phase of the image set, ϕ_C^* , is known. It is less likely, however, that the respiration phase of the image set is known. While these image sets are optimally collected during a breath hold [48], estimating a respiration phase

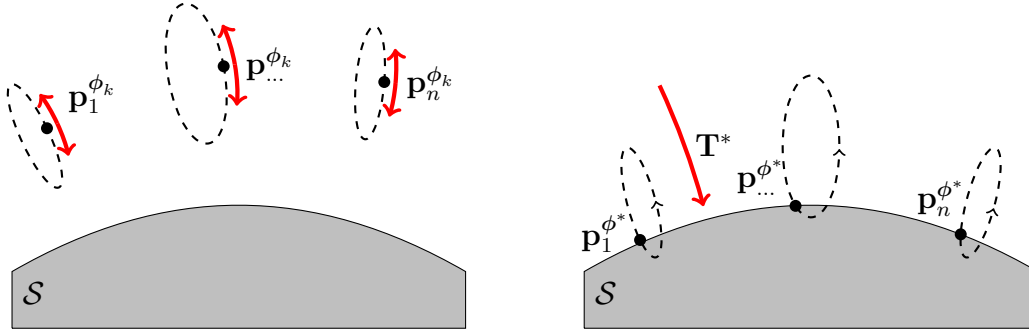


Figure 5.1: Registration of the periodic models of motion and the surface heart model requires simultaneously estimating the (a) phases corresponding to the map, $\phi^* = (\phi_C^*, \phi_R^*)$ as well as (b) the rigid registration which spatially the data, \mathbf{T}^*

during imaging is not well defined. Identification of the respiration phase that correspond to when the image set is taken is the temporal component to *spatiotemporal registration*.

The initial instinct to solve for temporal registration may be to minimize the previous metric over the physiological phases,

$$\phi_C^*, \phi_R^* = \operatorname{argmin}_{\phi_C, \phi_R} \left(\min_{\mathbf{T}} \sum_i (\mathcal{S}(\mathbf{u}_i) - \mathbf{T}\mathbf{p}_i^\phi)^2 \right). \quad (5.4)$$

Optimizing over the phases, in theory, solves for temporal registration if the shape of the heart is unique at the image phases. Data from live-animal experiments, however, do not bear this out. Plots showing RMS error for registration experiments conducted on data from six live-animal experiments is shown in Fig. 5.2. Average RMS error for these trials, in which we iterate over one phase while holding the other constant at the known image phase, shows that the temporal registration method given by (5.4) does not result in reliable global minimums.

The remainder of this chapter presents an empirical method for registering in phase due to the lack of a theoretical optimization metric that can be defined *a priori*. We first describe the data set used in this study, then present an empirical optimization metric based on the experimental data.

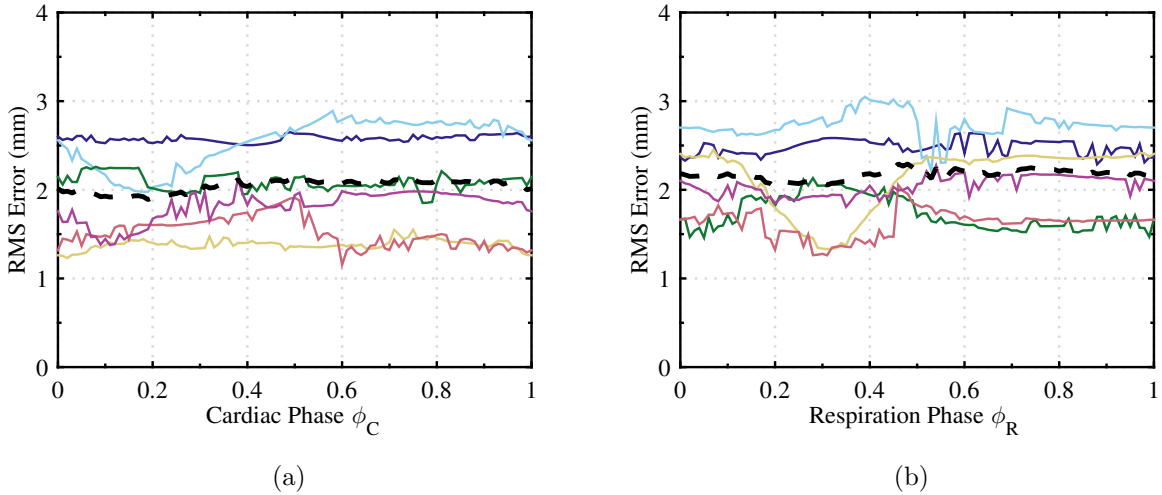


Figure 5.2: Registration RMS error across (a) cardiac and (b) respiration phase for six trials. Average RMS error across all trials is shown in bold dashed trials.

5.2 Experimental Data

In order to study how we may achieve temporal registration for virtual image guidance for organ-mounted robots, data from live animal experiments ($N=6$) conducted under a board approved protocol were analyzed retrospectively. The pre- and intraoperative protocol outlined in Section 2.7 was followed for each procedure. In each experiment an initial fiducial registration step was performed as described in Section 2.7.4. The Lamprey robot was then manually guided to collect heart motion data covering the entire heart. At each location sampled 6-DOF pose, respiration, and ECG signals were collected for approximately 30 s. Each of these signals was processed as described in Section 2.7.3 to yield the pose of the robot with respect to the chest wall and cardiac and respiration phases.

Information on each of the datasets used is shown in Table 5.1. ECG-gated cardiac CT image sets for each animal were collected prior to each experiment as described in Section 2.7.1. Image sets were collected during a breath hold after inspiration of the forced

Table 5.1: Trial Data

Trial	Points	Heart Rate ^a	Resp. Rate ^a	Im. Phase	\mathbf{R}_M^I ^b		
		(s^{-1})	(s^{-1})	ϕ_C^*	α ($^\circ$)	β ($^\circ$)	γ ($^\circ$)
1	101	1.08	0.20	0.66	-22.9	2.2	-43.8
2	108	1.36	0.20	0.61	-14.6	5.1	-63.5
3	98	1.59	0.17	0.64	-19.5	11.2	-59.0
4	44	1.42	0.17	0.66	-26.0	12.7	-86.0
5	84	1.37	0.17	0.64	-27.6	14.0	-55.6
6	95	1.03	0.17	0.67	-25.7	16.1	-78.4

^a Calculated as average over all points.

^b Rotation of map frame relative to image frame given as X - Y - Z intrinsic Euler angles. ($\mathbf{R}(\alpha, \beta, \gamma) = \mathbf{R}_x(\alpha)\mathbf{R}_y(\beta)\mathbf{R}_z(\gamma)$)

respiration system, which corresponds with a ground-truth respiration phase, ϕ_R^* , of 0.3. The desired cardiac phase targeted during imaging was 0.7. Using image metadata we can calculate the phase of each individual image slice, shown in Fig. 5.3 for all trials. Ground-truth image phases, ϕ_C^* , were calculated as the mean image phase over the image volume and ranged from 0.61 to 0.67. While 3 of the image sets do have jumps in cardiac phase, the portion of the cardiac cycle ranging from 0.6–0.8 is relatively motion-free [23].

Average heart rates for the 6 trials ranged from 1.03 to 1.59 Hz (62 to 95 bpm). Forced respiration was used in all cases with the first two trials using respiration frequencies of 0.2 Hz (12 bpm) and the remaining four 0.17 Hz (10 bpm). The rotation of the heart-centric frames with respect to the CT image coordinates are given as the X - Y - Z Euler angles.

Each of the 30-s time traces for each trial was then fit using the relative frame AM Fourier series models described in Chapter 4. Exponential coordinates were used for rotation. The numbers of harmonics used for each trial were $H_C = 5$, $H_R = 4$, $H_{MC} = 2$, and $H_{MR} = 1$. These models of position and orientation for each point i allow us to generate the position and orientation of the robot at any phase combination.

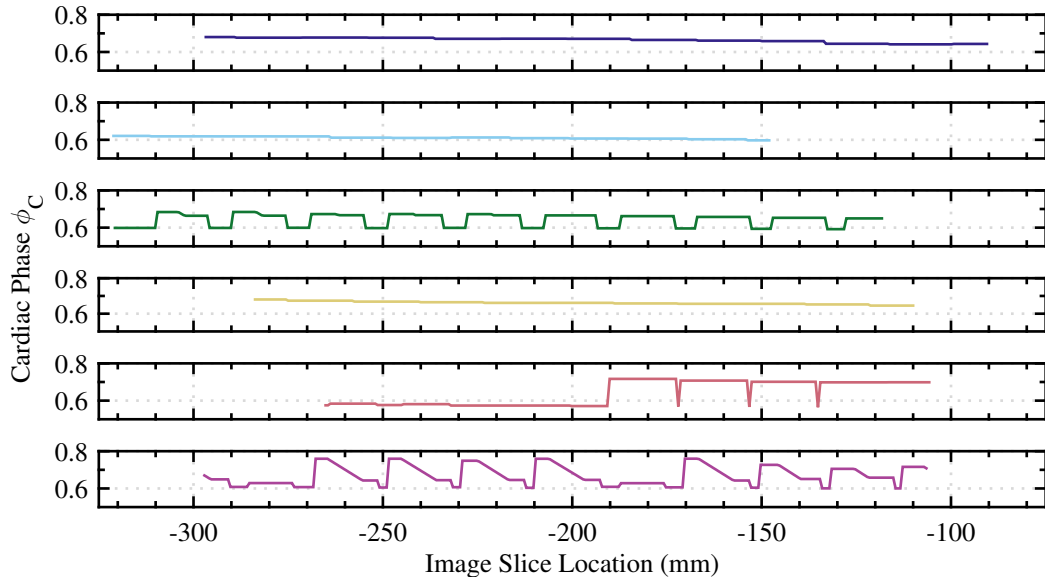


Figure 5.3: Cardiac phase for each image slice for each gated CT can be found using the time each image was required in conjunction with the detected QRS complexes in the image metadata.

5.3 Experiments

5.3.1 Respiration Phase Registration

Using the maps of the heart surfaces and the models of periodic motion, spatial registration parameters were solved for $\phi_C = \phi_C^*$ and ϕ_R ranging from 0 to 1 in increments of 0.01 using a standard ICP implementation [47]. Spatial registration estimated using fiducials, \mathbf{T}_0 , was used as the seed for ICP. RMS error from each point to the nearest point on the map as well as the registration parameters for each test were recorded. Various distance metrics were used for the point-to-surface correspondence, including the use of surface normals extracted from the periodic rotation model (4.23), and surface normals estimated from the surface mesh; however, they were found to have minimal effect.

RMS registration error over the entire respiration cycle for each of the trials was shown previously in Fig. 5.2. There is no discernible global minimum in the overall error, as it is nearly constant over the respiration cycle at 2 mm RMS. Registration parameters for each

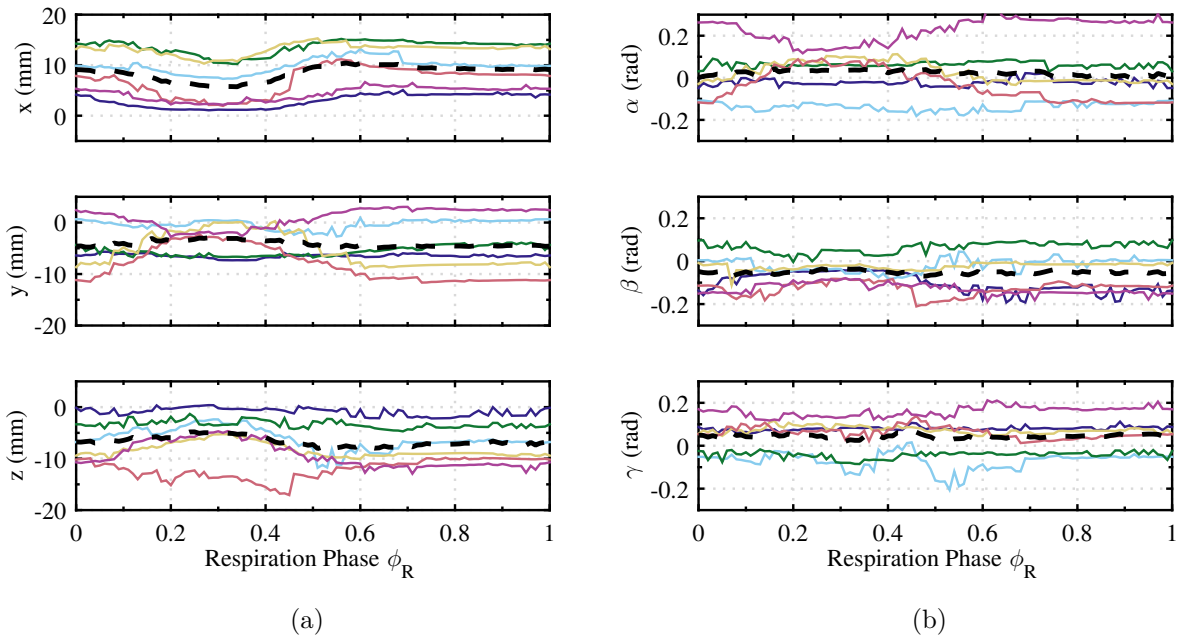


Figure 5.4: Registration parameters across respiration phase for all trials for (a) translation, (b) rotation. Average registration transformations are shown as bold dashed lines.

trial are shown in Fig. 5.4(a) for translation and Fig. 5.4(b) for rotation. These parameters are given in the heart-centric reference frames with rotation given in xyz -Euler angles.

Inspection of the translation registration parameters, shown in Fig. 5.4(a), reveals the first discernible trend. As the registration provided by the fiducials is used as the seed in the ICP implementation, the registration parameters found essentially yield the error in the fiducial registration. In all three directions, the mean registration reaches a global minimum at a respiration phase of ~ 0.3 . This effect is amplified when looking at the total 3D translation and rotation for these trials, shown in Fig. 5.5. Total translation is calculated as the norm of the translation vector, while total rotation is the geodesic distance.

In five of 6 trials, the global minimum registration translation distance occurs at a respiration phase of ~ 0.3 . The mean translation reaches a minimum of 9.9 mm at a respiration phase of 0.27. A similar trend does not hold for rotation, as the mean remains

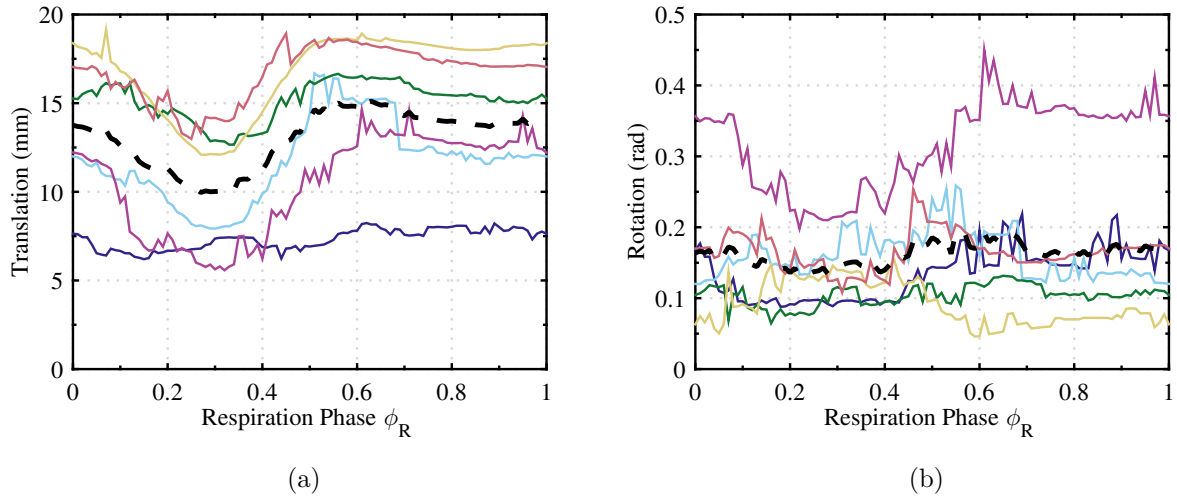


Figure 5.5: Magnitude of registration distances for (a) translation, (b) rotation. Average distances are shown as bold dashed lines.

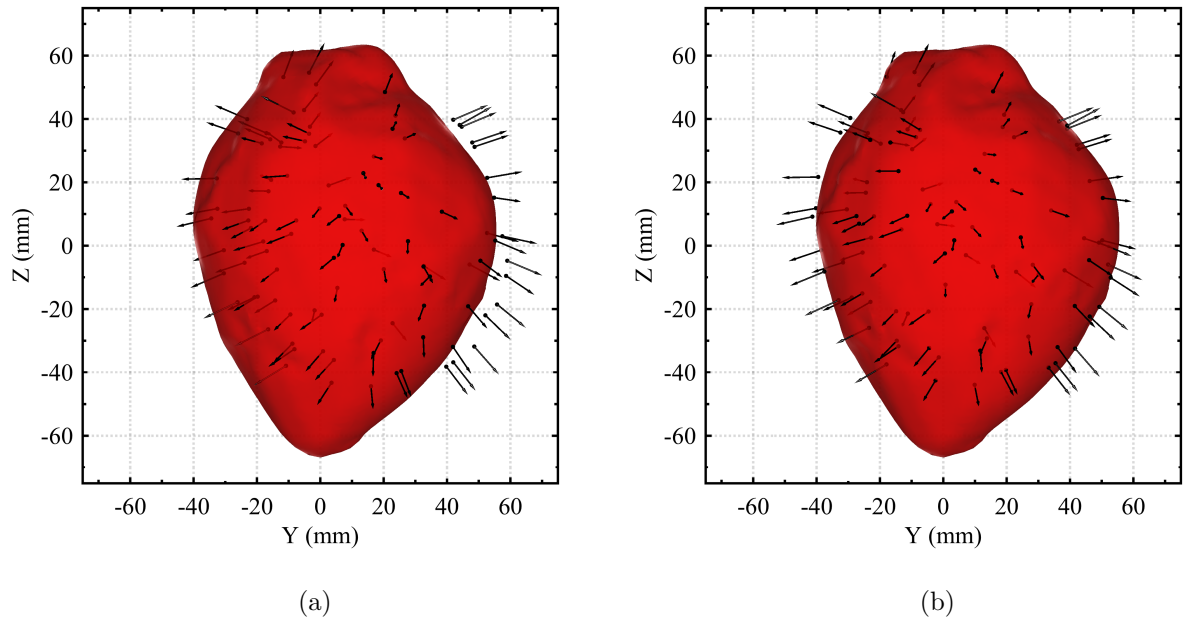


Figure 5.6: (a) The initial registration found using fiducials has significant error. (b) The final alignment after registration significantly reduces point to surface error.

fairly constant on average. The mean rotation distance at the phase corresponding to minimum translation is 8.2° . From these results, we can define an empirical registration metric for respiration phase as the phase which minimizes the magnitude of the translation from the initial fiducial registration.

$$\phi_R^* = \operatorname{argmin}_{\phi_R} \mathbf{d} \left(\mathbf{T}_0, \operatorname{argmin}_{\mathbf{T}} \sum_i (\mathcal{S}(\mathbf{u}_i) - \mathbf{T}\mathbf{p}_i^{\phi^*})^2 \right) \quad (5.5)$$

Results of registration can be seen qualitatively in Fig. 5.6, with the initial fiducial registration shown in Fig. 5.6(a) and the final registration in Fig. 5.6(b). The arrows represent the predicted surface normals from the motion models at the estimated image phases. Visually, the registered points more accurately fit the surface model of the heart and the predicted surface normals match the surface well. As these images qualitatively demonstrate, the initial fiducial registration is a reasonable estimate for anchoring the empirical registration metric.

5.3.2 Spatial Registration Comparison

In order to determine the effect of the use of the periodic motion of the heart in registration, we compared the results obtained using the previously described spatiotemporal registration approach to a simpler spatial registration where point motion is treated as noise. The de-noised estimate of registration using the mean position of each point, $\bar{\mathbf{p}}_i$ is given by

$$\bar{\mathbf{T}} = \operatorname{argmin}_{\mathbf{T}} \sum_i (\mathcal{S}(\mathbf{u}_i) - \mathbf{T}\bar{\mathbf{p}}_i)^2. \quad (5.6)$$

The points transformed by the estimated registration parameters were then projected to the closest point on the heart surface. Using the notation $\bar{\mathbf{u}}_i$ and \mathbf{u}_i^* for the map frame coordinates of these projected points on the heart surface, the distance between where the

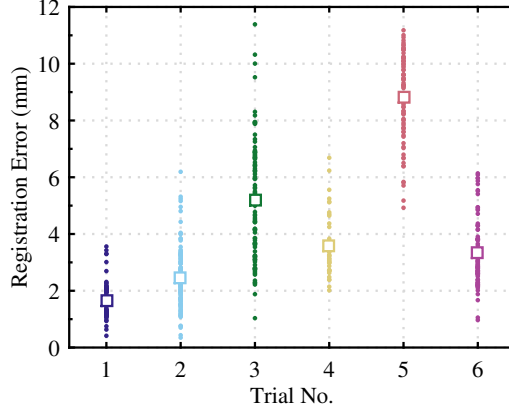


Figure 5.7: Difference in estimated position between registration methods.

two methods predict the robot is on the heart, δ_i , can be calculated as

$$\delta_i = \|\mathcal{S}(\mathbf{u}_i^*) - \mathcal{S}(\bar{\mathbf{u}})\|. \quad (5.7)$$

Because the surface models are convex, the Euclidean distance between the points will underestimate the distance along the surface between the points. However, due to the small curvature of the heart relative to the distances between points, this effect will be minimal.

A plot of the difference in predicted location on the surface of the heart is shown in Fig. 5.7. For each trial a single point error is shown as a dot, while the average over all points in a trial is shown as a square. Per-trial mean errors range from a minimum of 1.7 mm to 8.8 mm, with a mean error across trials of 4.2 mm.

5.4 Discussion

The results presented in this section have several important implications, as well as limitations, which must be accounted for when interpreting their meaning. First, temporal registration cannot be achieved by optimizing over the error in the fit between the data and model. This means that the shape of the heart at the image phases was not unique to

a level which can overcome the noise in the surface and motion models. Due to this, registration in cardiac phase is not feasible without including further information. This is not a significant limitation, however, as we have reasonable expectation that diagnostic imaging prior to any intervention would include a cardiac-gated image set that ground-truth cardiac phase can be extracted from.

Next, motion of the heart due to respiration has been shown to be, in part, a rigid motion applied to the entire heart[76]. This observation agrees with our observation of invariance of error with respiration phase, and provides a grounding for the empirical respiration-phase registration metric we presented. Minimizing the magnitude of translational component of spatial registration simply finds the rigid motion which most closely agrees with fiducial registration.

Finally, we showed that the mean error between the predicted robot location using the periodic motion of the heart as opposed to filtering it out is ~ 4 mm. While the acceptable positioning error will be intervention-specific, identifying the required clinical accuracy is difficult. These estimates of clinically required accuracy are often ad hoc and based on the best guess of the clinician. An “acceptable” error often used is ~ 5 mm [33].

Several factors must be noted here. First, achieving this level of accuracy while ignoring the motion requires an accurate estimate of the mean position of the robot. Because of the low frequency of the respiration motion, this still requires significant time to observe, time in which we could be learning the actual motion of the heart. Finally, we reiterate that the major focus of this work is to push the envelope of what is possible in minimally invasive surgery as a means to enable new interventions.

Chapter 6

Localization

The previous two chapters presented methods for modeling the periodic motion of the surface of the heart and registering these motion models to static preoperative maps of the heart surface. Using these methods, accurate estimates of the position of the robot on the surface of the heart can only be achieved once the frequency-based models have converged. Due to the low frequency of respiration ($\sim 0.2 \text{ Hz}$) this requires a significant amount of time. While accurate registration requires accurate predictions from the models, once registration has converged, waiting for accurate predictions wastes valuable time. We refer to this post-registration estimation of position on the heart as localization.

This chapter presents the use of function approximation for robot localization. This method uses models of previously observed motion at other locations to predict where on the surface of the heart new observations will fall. These estimates outperform model-based prediction over short time horizons, and may help in reducing the time required to perform interventions. This chapter first briefly poses the localization problem using previously presented motion models in Section 6.1. Next, in Section 6.2, we reinterpret the problem as function approximation. Finally, Section 6.3 presents experimental results comparing the approaches and characterizing performance.

6.1 Localization via Motion Prediction

Localizing on a registered surface is trivial in most cases. In the case of a static surface with a static map, the spatial registration parameters provide full information to associate a single measurement of robot pose to a location on the surface of the heart. Registration fully constrains this problem.

In the case of a periodically deforming surface with a static map, however, the problem is less trivial. If the measurements of robot pose have the same phase as the map, the problem is once again fully constrained. If the measurements are not the same phase as the map, we must project the measurements to the correct phase.

Using the previously derived model for periodic motion (Chapter 4) and assuming that spatial and temporal registration, \mathbf{T}^* , ϕ_C^* , and ϕ_R^* , have been solved, the estimated location of the robot on the heart, $\tilde{\mathbf{u}}$, is defined as the nearest location in the map,

$$\tilde{\mathbf{u}} = \underset{\mathbf{u}}{\operatorname{argmin}} \|\mathcal{S}(\mathbf{u}) - \mathbf{T}^* \mathbf{p}^{\phi^*}\|, \quad (6.1)$$

where

$$\mathbf{p}^{\phi^*} = \mathcal{P}(\phi_C^*, \phi_R^*) = \mathcal{M}_q^{\mathbf{R}}(\mathbf{q}_{\mathbb{H}}^{\mathbf{P}}) \mathbf{W}_{\mathbf{t}}^T \boldsymbol{\phi} + \mathbf{t}_{\mathbb{H}}^{\mathbf{P}}. \quad (6.2)$$

This formulation for localization is identical to the matching procedure used in ICP for registration; however, in that case it was assumed the models had converged and provided reasonable estimates of robot pose. In the case of using this formulation for localization, it is clear that localization error relies directly on the accuracy of the model. As we have shown in Chapter 4, convergence for these models requires up to 15 s (~ 3 respiration cycles).

In this scheme the accuracy of prediction is a function of how long the robot stays at a single location. This dependence is demonstrated graphically in Fig. 6.1. The longer the robot observes the motion, the more accurate the model, and the more accurate the

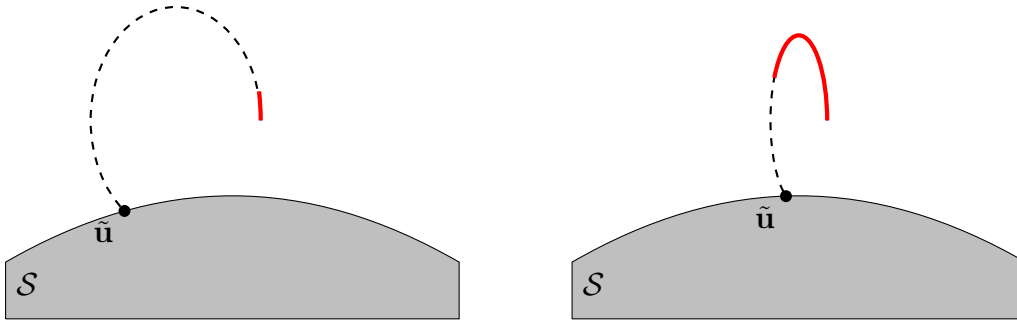


Figure 6.1: Using motion prediction models for localization requires predicting the future location of the robot at the phase of the heart model. The predicted motion, shown as a dashed line will change significantly from (a) after only a few observations to (a) observing for longer periods of time. The accuracy of the predicted location, $\tilde{\mathbf{u}}$, will improve as our model improves.

prediction. Depending on the acceptable level of accuracy, this may require remaining stationary for long periods of time.

6.2 Localization via Function Approximation

In order to bypass the long convergence time required to accurately localize using motion prediction, localization problem can be reinterpreted to utilize all available data. Accurate registration requires accurate models of the motion of points spread over the surface of the heart. These models enable prediction of robot pose at these points for any phase, as well as where the points lie on the surface of the static heart. Using these data, localization can be posed as function approximation.

A diagram of this approach to localization is shown in Fig. 6.2. Given a measurement of the robot pose at the current phase, \mathbf{z}^{ϕ_k} , the predicted location of the robot on the heart, $\tilde{\mathbf{u}}$, can be estimated by approximating the function which maps from the existing models' predictions of pose at the current phase, $\{\mathbf{p}_1^{\phi_k}, \mathbf{p}_2^{\phi_k}, \dots, \mathbf{p}_n^{\phi_k}\}$, to their corresponding locations on the heart, $\{\mathbf{u}_1, \mathbf{u}_2, \dots, \mathbf{u}_3\}$.

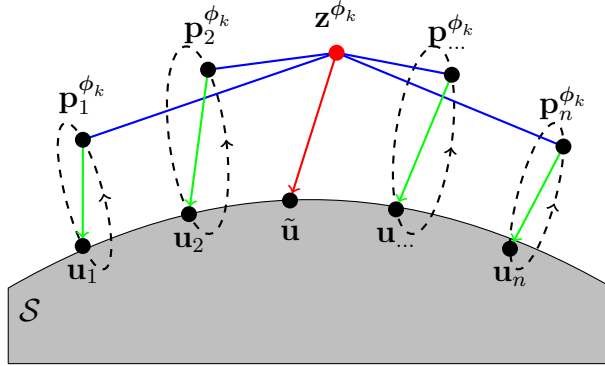


Figure 6.2: Using the motion models of previously observed heart motion, the localization problem can be posed as an interpolation or function approximation. In this scheme we learn a function which maps from robot pose and phase to map.

6.2.1 Radial Basis Function Approximation

In order to approximate the mapping to the surface of the heart, we employ radial basis function (RBF) interpolation. This method of scattered data interpolation is ubiquitous, being used in applications including solving partial differential equations [77], surface reconstruction [77], and nonlinear registration and surface estimation in medical imaging [78–80]. We briefly review RBFs here and point the reader to [81] for further information.

Radial basis functions approximate the real-valued function, $f : \mathbb{R}^d \rightarrow \mathbb{R}$, with $f : \mathbb{R}^d \rightarrow \mathbb{R}$, given the values $\{f(x_i) : i = 1, 2, \dots, n\}$ at the centers of interpolation $\{x_i : i = 1, 2, \dots, n\}$. The interpolant is of the form

$$f(x) = \sum_{i=1}^n \lambda_i \kappa(r(x_i, x)), \quad (6.3)$$

where $r(\cdot, \cdot)$ is a distance metric on \mathbb{R}^d , usually the Euclidean norm,

$$r(x_i, x) = \|x_i - x\|. \quad (6.4)$$

The kernel function, κ , is a positive definite, fixed function whose value only depends on the distance from the center. Common basis functions include

$$\text{Multiquadric:} \quad \kappa(r) = \sqrt{1 + (\epsilon r)^2} \quad (6.5)$$

$$\text{Gaussian:} \quad \kappa(r) = e^{-(\epsilon r)^2} \quad (6.6)$$

$$\text{Thin Plate Spline:} \quad \kappa(r) = r^2 \log r \quad (6.7)$$

$$\text{Linear:} \quad \kappa(r) = r. \quad (6.8)$$

Real-valued weights, λ_i , satisfy the interpolation conditions at the centers,

$$f(x_i) - \} (x_i) = 0, \quad \forall i. \quad (6.9)$$

Writing the system in linear form,

$$K\boldsymbol{\lambda} = \mathbf{g}, \quad (6.10)$$

where

$$K_{i,j} = \kappa(r(x_i - x_j)) \quad (6.11)$$

$$\boldsymbol{\lambda} = [\lambda_1, \lambda_2, \dots, \lambda_n]^T \quad (6.12)$$

$$\mathbf{g} = [\} (x_1), \} (x_2), \dots, \} (x_n)]^T, \quad (6.13)$$

and assuming the problem is well conditioned, the inverse of K exists. The weights are then found using the inverse,

$$\boldsymbol{\lambda} = K^{-1}\mathbf{g}. \quad (6.14)$$

6.2.2 RBF's for Organ-mounted Robot Localization

Although it may be possible to construct an RBF interpolant using a distance metric over an anisotropic space [82], the problem is simplified by not considering the full state space

– $\mathbb{R}^3 \times \mathbb{S}^1 \times \mathbb{S}^1$ (3D position, ϕ_C , and ϕ_R) – and instead solve the problem at each instant using a more standard metric over \mathbb{R}^3 .

At a particular instant, $\boldsymbol{\phi}_k = (\phi_{C_k}, \phi_{R_k})$, the centers of the interpolant are the predicted positions of the n motion models used during registration, $\{\mathbf{p}_1^{\phi_k}, \mathbf{p}_2^{\phi_k}, \dots, \mathbf{p}_n^{\phi_k}\}$, and the query point is the current position measurement of the robot, \mathbf{z}^{ϕ_k} .

Instead of directly estimating the map coordinates, we instead attempt to learn the deformation field, or the translations required to move each center to its location on the map. This is done to first avoid the complications of singularities or constraints in spherical coordinates, and also to effectively zero-mean the data. The function to be approximated, $\mathcal{S}(\cdot)$, is the difference between the registered and current locations,

$$\mathcal{S}(\mathbf{p}_i^{\phi_k}) = \mathcal{S}(\mathbf{u}_i) - \mathbf{p}_i^{\phi_k}. \quad (6.15)$$

Localization is solved by estimating the deformation at the query point and identifying the closest point in the map to the deformed position estimate,

$$\tilde{\mathbf{u}} = \underset{\mathbf{u}}{\operatorname{argmin}} \left(\mathbf{z}^{\phi_k} + \sum_{i=1}^n \lambda_i \kappa_i \cdot \left(\|\mathbf{p}_i^{\phi_k} - \mathbf{z}^{\phi_k}\| \right) \right). \quad (6.16)$$

6.3 Experiments

The previously described methods of localization, motion modeling, and RBF approximation, were tested retrospectively on data collected during a live-animal closed-chest beating-heart procedure. The Lamprey robot was used to collect ~ 100 thirty-second time traces while attached to the beating heart. Virtual image guidance was used to guide uniform coverage of the heart. The data were processed and fit using frequency-based models presented in Chapter 4, then registered to the anatomical model using the methods presented in Chapter 5.

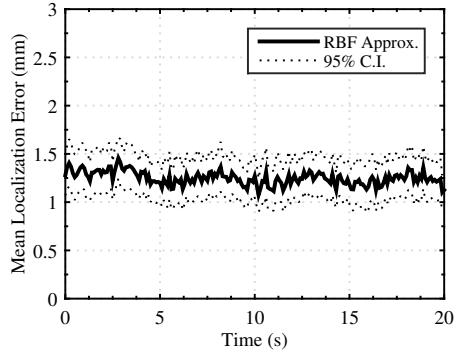


Figure 6.3: Localization error using radial basis functions is essentially constant in time. This plot shows the best performance achieved and uses the cartesian distance metric, multiquadric radial basis function with $\epsilon=1$, and differential cartesian coordinates for prediction variable.

6.3.1 RBF Localization Performance

Optimal localization performance with RBF approximation was achieved using a multi-quadric basis function with a shape parameter $\epsilon = 1$, and is shown in Fig. 6.3. This trial shows the mean error across all points for 20 s with estimation occurring every 0.1 s.

In this trial, localization was estimated for each point in a leave-one-out fashion such that all remaining points were used as interpolation centers. The raw data for each point, which were used to construct the motion model, were used as query locations, and the error in localization was calculated as the Euclidean distance from the ground-truth location estimated during registration. The data shown in Fig. 6.3 are the mean and standard error across all points.

Mean localization accuracy across the entire run was 1.25 mm with a 95% confidence interval of ± 0.22 mm. While there is variation in estimates at what appears to be the respiration period (~ 5 s) the effect is less than 0.25 mm peak-to-peak.

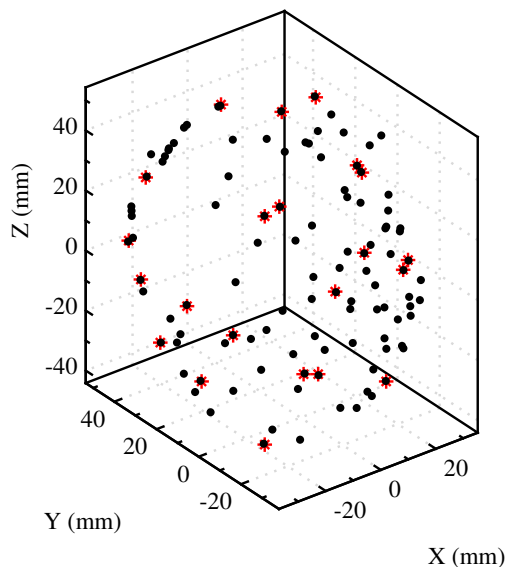


Figure 6.4: Approximate uniform sampling of centers from a point cloud identifies points with the greatest distance to its nearest center. This example shows 22 centers (*) sampled from the 108 point data set.

6.3.2 Effects of Center Density

In order to determine the effects of the density of centers on localization error, experiments were conducted in which the number of interpolation centers used ranged from 1.0 to 0.2 of the total number of point observations. Uniform sampling over the surface of the heart was approximated via a sampling scheme that chose points to convert to centers which were farthest from the nearest existing interpolation center. Sampling was randomly initialized and continued until the desired number of centers was identified. For each subsampled set the average minimum inter-center distance was calculated as an approximation of center density. An example of 22 centers sampled from the 108 point set is shown in Fig. 6.4.

For each set of sampled centers, prediction trials were conducted for all 108 points to estimate localization accuracy. Predictions were done for 20 s for each point at 10 Hz. Prediction errors were combined across all points and time to estimate a single mean prediction error for each set of centers. Results of these trials are shown in Table 6.1 and Fig. 6.5.

Table 6.1: Results from Center Density Experiment

Samp. Ratio	No. Centers	Avg. Dist. ^a (mm)	Mean Error (mm)	$\pm 95\%$ Conf. Int. (mm)
1.0	107	3.9	1.25	0.22
0.9	97	4.6	1.30	0.22
0.8	86	5.3	1.37	0.22
0.7	76	5.9	1.34	0.24
0.6	65	6.7	1.43	0.24
0.5	54	7.6	1.54	0.24
0.4	43	8.8	1.62	0.25
0.3	32	10.9	1.74	0.26
0.2	22	13.4	1.99	0.29

^a Calculated as average of the minimum distance between each center.

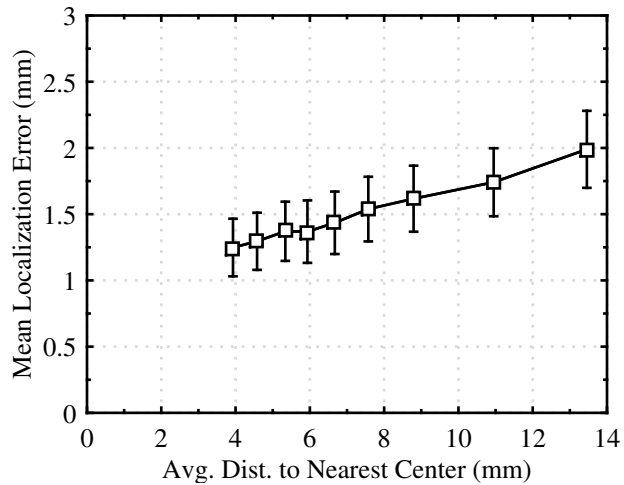


Figure 6.5: Interpolation error using Radial Basis Functions increases as the density of centers decreases. Square markers denote mean error with error bars representing 95% confidence interval of the mean estimate. Density is approximated as the average of the minimum distance between centers.

Reduction in the density of center locations caused an expected increase in localization error. The effect is highly linear as a function of density, increasing localization error from 1.25 mm to 1.99 mm as the average spacing of centers increased from 3.9 mm to 13.4 mm.

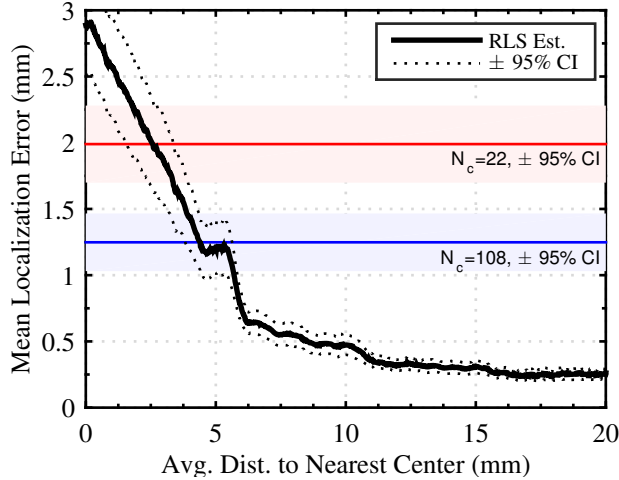


Figure 6.6: Localization performance using motion prediction decreases as the motion model observes more data and becomes more accurate. RBF localization results are shown for minimum and maximum center density.

The number of interpolation centers used decreased almost five-fold from 107 to 22. Even with this significant reduction in centers, localization error remains small.

6.3.3 Motion Prediction Comparison

Motion-prediction localization simulations were run to provide a comparison of the localization methods. Using the method described in Section 6.1, an AM Fourier series model of the motion of each point was learned and used to predict the robot location at the map, phase which was then used to estimate the robot’s location on the heart. All parameters of the model were initialized to zero. Estimation was conducted for 20 s at 100 Hz. Error was calculated as the Euclidean distance between the ground-truth location estimated during registration and the predicted location, and averaged across all points to yield mean error, shown in Fig. 6.6.

Because the motion-prediction scheme relies on estimating a motion model, prediction accuracy is correlated with time. As more measurements are observed, the motion models become more accurate and reduce prediction error. Also shown in Fig. 6.6 are the mean

and 95% confidence intervals for the minimum and maximum number of centers used in the previously described RBF approximation experiments. While the motion-prediction scheme provides much more accurate estimates of position over long time horizons, more accurate estimates of location are achieved using RBF approximation for the first ~ 2.5 s using only 22 centers and ~ 4.5 s using all centers.

6.4 Discussion

The two localization schemes presented in this chapter should be viewed as complimentary approaches that should both be used in real-time operation of the robot. The RBF approximation provides very accurate estimates of robot location instantaneously. This method can be used to provide reasonable estimates of robot location even when the robot is not attached to the heart. For applications that require less accurate positioning, RBF approximation may be sufficient on its own.

For applications that require more accurate positioning, RBF approximation can be used over short time horizons and can then hand off estimation to the motion-prediction scheme over longer time horizons. RBF approximation may possibly even be used to “jump-start” the motion-prediction models if an estimation scheme more complex than recursive least squares is employed for learning.

From a general perspective, the localization accuracy achieved by using motion prediction is relatively small (~ 3 mm) at the first time step. While this level of accuracy may be sufficient for many existing therapies, we reiterate our position that the presented work will have the greatest effect on enabling therapies that are not possible with existing technologies.

Part II

Specialized Organ-mounted Robots

Chapter 7

HeartLander: Delivery of Thermosensitive Materials

The growth of our family of organ-mounted robots from HeartLander is due to the specialization required for emerging therapies. The first emerging therapy we consider is the injection of materials that transition from liquid to gel as their temperature rises to body temperature. These thermoresponsive hydrogels, when injected in localized patterns into the infarcted myocardium, are effective in preventing changes in the structure of the infarcted tissue. Delivery of these materials to the heart requires actively preventing premature transition from liquid to gel.

This Chapter presents the coordinated development of an actively cooled injection system for the HeartLander robot and a specifically formulated thermoresponsive hydrogel. This collaborative work builds on prior efforts [83–86] to develop an alternative option for minimally invasive delivery of hydrogel to the left ventricle without entering the circulation system.

First, Section 7.1 provides a brief overview of hydrogel therapies and the thermoresponsive hydrogels formulated by our collaborators specifically for robotic delivery. The design of the active cooling system and modified HeartLander robot follows in Section 7.2.

Finally, Section 7.3 presents the successful delivery of this material in a predetermined pattern in a live-animal beating-heart procedure.

7.1 Hydrogel for Myocardial Infarction Therapy

7.1.1 Clinical Relevance

Pathological remodeling of the ventricular wall following myocardial infarction (MI) can ultimately lead to end-stage heart failure and death. The loss of myocardium after MI results in an abrupt increase in loading conditions, causing a unique pattern of remodeling involving the feedback loop of higher wall stress, left ventricle (LV) dilation and a thinning ventricular wall [87]. The injection of hydrogels into and around the infarcted myocardium has been effective in preventing ventricular remodeling and maintaining cardiac function putatively by providing mechanical support [21, 88, 89].

Recently, clinical trials have been launched in an effort to translate intramyocardial hydrogel injection therapy to the bedside [90–92]. One of the advantages of hydrogel injection therapy is its potential to be delivered in a minimally invasive fashion; for instance Seif-Naraghi et al. successfully injected extracellular matrix-derived hydrogel through a percutaneous transendocardial intervention and Leor et al. delivered alginate by intracoronary infusion, both in pig models [93, 94]. Both techniques approach the injection sites by catheter originating through a femoral artery access site. No remote infarction or embolization was reported in either pig model; however, there are safety concerns. Particularly with gel materials, the risk of backflow and embolization from an endocardial injection site is a serious concern.

Epicardial injections, such as those demonstrated using HeartLander, obviate these concerns. Further, accurate and targeted delivery using HeartLander would be compatible with a patient-specific planning strategy to optimize the mechanical benefits of the hydrogel

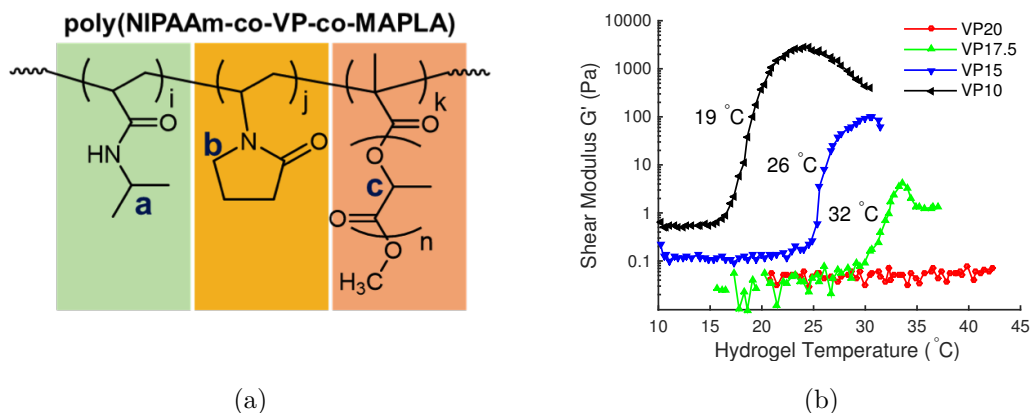


Figure 7.1: (a) Composition of poly(NIPAAm-co-VP-co-MAPLA). (b) Shear modulus of poly(NIPAAm-co-VP-co-MAPLA) hydrogels under temperature change.

bulking effect [95, 96].

7.1.2 Thermoresponsive Hydrogel Design

Our efforts in designing and constructing a robot specifically for this task were coordinated with the design of the injectable hydrogel by our collaborators. We briefly outline their singular contribution here and point the reader to [97] for further details.

A biodegradable, thermoresponsive poly(NIPAAm-co-VP-co-MAPLA) (NIPAAm: N-isopropylacrylamide, VP: N-vinylpyrrolidone, MAPLA: methacrylate-poly(lactide)) which gels from a low viscosity solution as the temperature increases to 37 °C with varied composition was synthesized by radical polymerization. In the polymer design, which is shown in Fig. 7.1(a), NIPAAm provides thermal responsiveness, while increasing VP content tunes the hydrophilicity for lower viscosity, higher transition temperatures and longer transition times. MAPLA, incorporating hydrolytically labile PLA segments, provides an “insoluble to soluble” shift to the whole polymer at body temperature as these hydrophobic segments are cleaved. Similar synthetic hydrogels have shown benefit in small animal models, and the general concept of hydrogel introduction into the infarcted LV wall is undergoing

clinical evaluation using endovascular delivery approaches [85, 86].

To ensure smooth injection without solidifying the hydrogel in the catheter, a hydrogel with a higher transition temperature is more attractive. As shown in Fig. 7.1(b), the transition temperature increases as the VP feed ratio used in the polymer synthesis increases, from 19 °C (VP10) to an indiscernible transition (VP20). In addition, the viscosity of the hydrogel in the solution state decreased with the increased VP content, which also favored easier hydrogel delivery. In order to identify the hydrogel in tissue using photoacoustic (PA) imaging, indocyanine green (ICG) photoacoustic dye was dissolved in the hydrogels.

7.2 Design of Active Cooling System

Successful delivery of liquid hydrogel to the myocardium with HeartLander comes with several restrictions other than the thermal requirements imposed by the hydrogel. The tight confines of the intrapericardial space preclude increasing the size of the robot, eliminating any approaches localized to the distal portions of the robot and thereby requiring delivery from outside the body. The subxiphoid approach used to gain access means that a relatively long distance (~ 0.3 m) of any delivery tether is exposed to body temperature (37 °C). Adding stiffness to the tethers, however, decreases locomotion capabilities.

These design constraints, in conjunction with insights gleaned from prior efforts [83, 84], lead to the dual-lumen injection system shown schematically in Fig. 7.2. The cooling system takes the form of a parallel-flow heat exchanger, in which an inner lumen carrying hydrogel is surrounded by saline flowing through an outer sheath. Space limitations restrict the ability to recirculate the cooling fluid, which is expelled into the intrapericardial space. In order to improve locomotion of the device the injection system is terminated in the rear body of the robot. The remainder of this section outlines the experiments conducted in order to optimize and validate the design of the cooling system under the presented constraints.

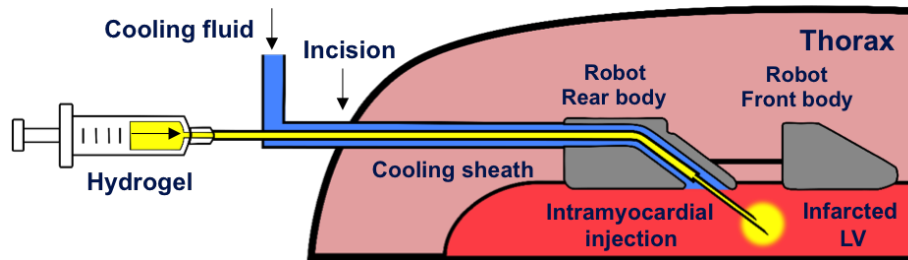


Figure 7.2: The cooling system for delivery of thermoresponsive hydrogel consists of a dual-lumen parallel-flow heat exchanger design. The hydrogel is kept in its liquid state from outside the body to the infarcted heart by a jacket of cooled saline. Terminating the injection system in the rear body of the robot allows for improved locomotion capabilities.

7.2.1 Simulation Study

A computational model of the parallel-flow heat exchanger model was developed using COMSOL Multiphysics software in order to determine the required cooling fluid flow rate so that a peristaltic pump could be selected for use in the injection system, and the size of the outer PTFE tube of the injection system. The implemented model sought to provide estimates for the worst-case operating scenario of the cooling system, namely when the device was deployed on the heart and the injection catheter was filled with solidified body-temperature hydrogel.

The implemented model was a 2D axisymmetric model with an overall length of 0.30 m. The inner channel dimensions assumed the nominal dimensions of 23 gauge PTFE Light Wall Tubing (inner diameter (ID) = 0.66 mm, wall thickness (WT) = 0.15 mm), while the outer channel dimensions were varied to correspond to 15 and 17 gauge PTFE Light Wall Tubing. The hydrogel was modeled as a stationary solid, while the cooling fluid was modeled as liquid water. A constant-temperature heat source at 37 °C was applied to the outer surface of the outer lumen. The inlet temperature of the cooling channel was set to 12.5 °C with flow rates of 0.25, 0.42, 0.58, 0.73, and 1.0 mL/s. Thermal and mechanical properties for the cooling fluid and PTFE tubes were set using COMSOL's built-in material

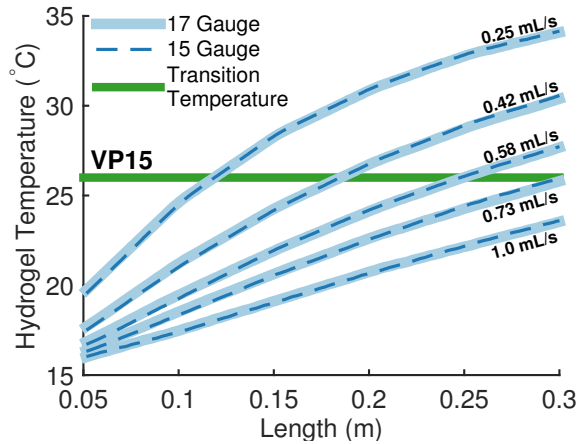


Figure 7.3: Results from simulation of the cooled injection system. The size of the outer sheath has virtually no effect on hydrogel temperature profile and the driving factor is the flow rate of the cooling fluid.

definitions.

Simulation results, shown in Fig. 7.3, with varied cooling fluid flow rates and outer tube diameters show that the greatest influences on the hydrogel temperature distribution are the cooling fluid inlet temperature and flow rate. Changing the tube diameter from 15 to 17 gauge has little effect on the hydrogel temperature profile, leading to the choice of 17 gauge outer tubing to minimize tether stiffness, and a cooling fluid flow rate of 0.73 mL/s to keep the hydrogel below the 26 °C transition temperature of the VP15 hydrogel formulation.

7.2.2 Water Bath Study

Using the results obtained from the simulation environment, a peristaltic pump (Stenner 85MHP17, Stenner Pump Company, Jacksonville, FL) was identified which provides sufficient flow to cool the hydrogel. A length of 0.30 m of the injection system was submerged in a 0.30 m × 0.14 m × 0.03 m container filled with water at 36.5 to 37.5 °C. The distal end of the injection system protruded out of the container to empty the cooling fluid outside of the system. A thermocouple with attached microprobe was inserted to measure

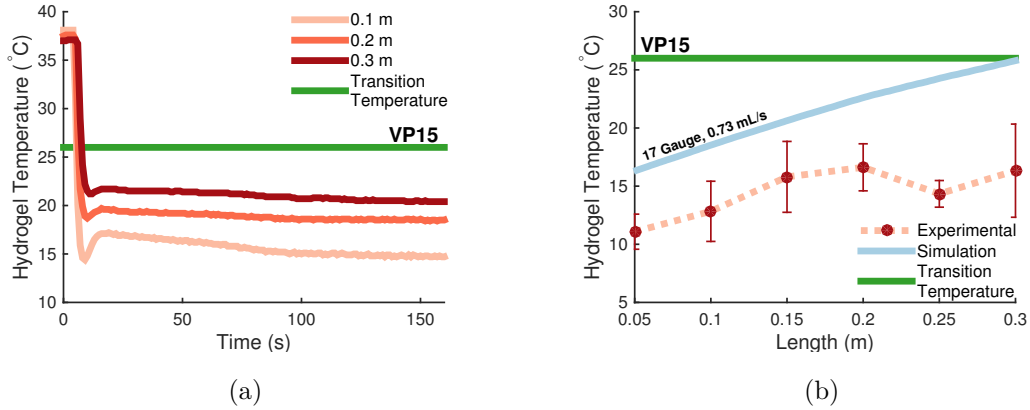


Figure 7.4: (a) Time trace of hydrogel temperatures at three locations in a water bath. At each location the hydrogel was allowed to reach the steady-state temperature before engaging the cooling system. Transition to liquid at all locations occurred within 10 s. (b) Steady-state performance of the cooling system. Each dot corresponds to the mean of steady state cooled temperature averaged over 3 trials at each location, while the error bars correspond to standard deviation.

the hydrogel temperature at intervals of 0.05 m along the tube. Water at 0 to 3 °C was used as the cooling fluid and pumped at a rate of 0.73 mL/s. The measured temperature of the cooling fluid at the inlet to the injection system was 12.5 °C.

VP15 hydrogel was loaded into the injection system and allowed to reach 37 °C. Once the hydrogel had reached the temperature of the water bath, the pump was started and temperature measurements of the hydrogel were taken at intervals of 1 s for approximately 3 min to ensure that it reached steady state. This procedure was performed three times.

Time traces of the temperature of the hydrogel at various points along the length of the cooling system are shown in Fig. 7.4(a). The cooling system lowered the temperature of the hydrogel to a minimum in approximately 10 s, at which time the temperatures increased slightly and settled to steady-state values. The steady-state values along the entire length of the injection system, shown in Fig. 7.4(b), were well below the transition temperature of VP15. Within the first 0.2 m the steady state temperature was near or below the transition temperature of VP10. Since the distance from the subxiphoid incision

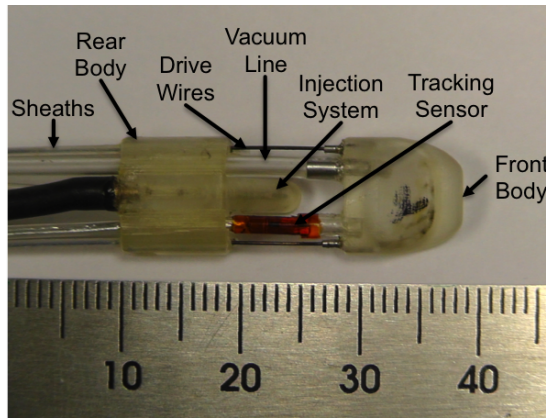


Figure 7.5: Modified HeartLander with cooled injection system.

to the epicardial injection sites would be less than 0.3 m, the hydrogel would be expected to remain in the liquid state.

7.2.3 Incorporation into HeartLander

Modifications to the existing HeartLander design were required to accommodate the dual-lumen cooled injection system, with the modified HeartLander shown in Fig. 7.5. Again, moving the injection channel to the rear foot mitigates the effect of the cooling system on locomotion. In order to accommodate the cooling system the bodies were widened from 8 to 9.85 mm. The cooled injection system consists of inner and outer polytetrafluoroethylene (PTFE) tubes of 23 and 17 gauge respectively. All remaining components (drive wires, sheaths, vacuum lines, and tracking sensor) remain unchanged.

7.3 Experiments

7.3.1 Water Bath Injections

To evaluate the coordination between hydrogel and the cooling system, the catheter was preloaded with hydrogel and submerged in 37 °C water bath to reach an isothermal state,

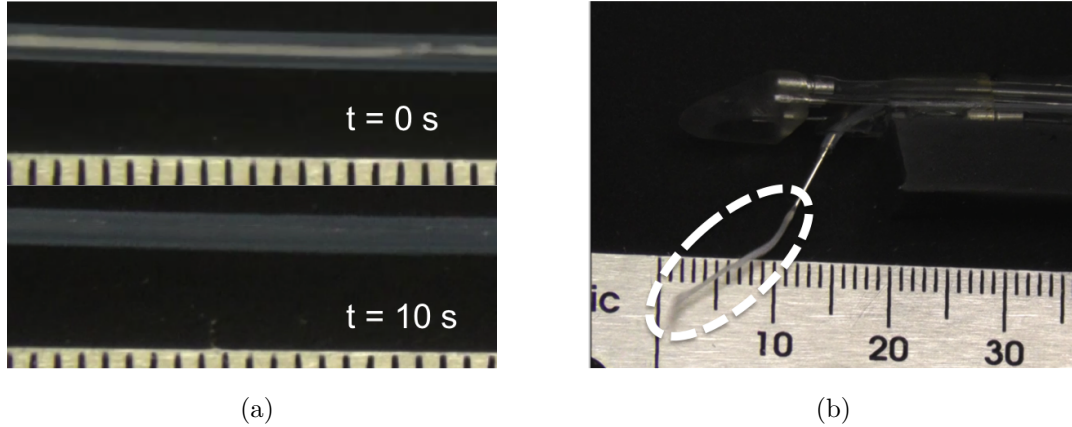


Figure 7.6: (a) Cooling system confirms ability to dissolve gelled VP15 occluding injection line.(b) Cooled injection of VP15 hydrogel in 37 °C water bath.

followed by active cooling. VP15 gelled and occluded the catheter at 37 °C, and the hydrogel was dissolved as a result of heat transfer with the cooling fluid, allowing reoccurrence of smooth injections. The unblocking process took ~ 10 s for VP15, as shown in Fig. 7.6(a), consistent with the measured time required for the cooling system to bring the hydrogel temperature down to near transition temperature (Fig. 7.4(a)). Injection capabilities were also confirmed with the entire needle exposed to the water bath, as shown in Fig. 7.6(b).

7.3.2 Injections Ex Vivo

In an injection test ex vivo using an excised porcine heart at 37 °C, the injection device successfully crawled to 2 distant injection sites and performed one shallow injection at 3.5 mm deep and one deeper injection at 6.8 mm deep, as shown in Fig. 7.7. The injection depth was controlled by the distance the needle was pushed out of the catheter. The hydrogel temperature was maintained below the hydrogel transition temperature and no gelation was observed in fluid pathway. It took approximately 10 s to complete the injection of 0.3 mL VP15 hydrogel. Inspecting the site visually by dissection 5 min after the injection showed ellipsoid hydrogel deposits with long axes orienting along the circumferential di-

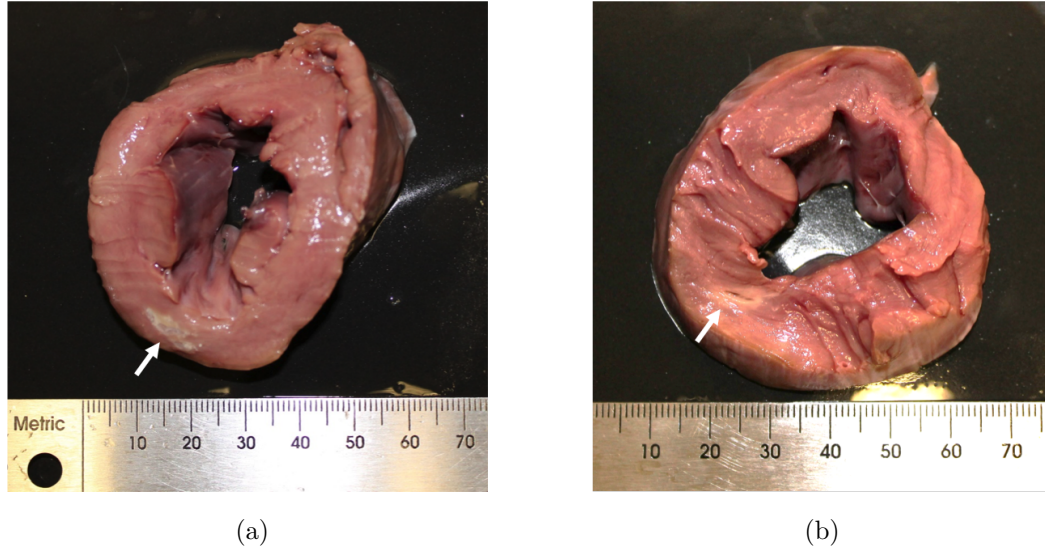


Figure 7.7: Ex vivo injections performed on an excised porcine heart warmed to 37 °C. Ability to perform (a) shallow and (b) deep injections were confirmed.

rection. The shallow deposit, shown in Fig. 7.7(a), was 10.8 mm long and 3.1 mm wide, whereas the deeper deposit, shown in Fig. 7.7(b), was 8.2 mm long and 2.7 mm wide.

7.3.3 Beating Heart Injections in Porcine Model

Demonstration of the modified injection system design was performed in a porcine model in vivo in a protocol that followed the National Institutes of Health guidelines for animal care and that was approved by the University of Pittsburgh's Institutional Animal Care and Use Committee.

A preoperative static 3D computed tomography (CT) image dataset was collected in order to provide image guidance during the procedure, and in order to plan the desired injection pattern on the epicardial surface. Surface models of the pericardium, endocardium, cardiac vasculature, rib cage, and fiducial markers on the chest wall were constructed from the 3D image set. A 15 mm square injection pattern was planned on the anterior surface of the left ventricle between the anterior interventricular artery and the diagonal artery,

as might be planned in a patient-specific manner for an ischemic area after an MI.

Approximately 30 min before the procedure, saline cooling fluid was placed in an ice bath and remained there throughout the procedure. Temperature measurements of the saline were taken periodically both pre- and intraoperatively. The temperature of the cooling fluid was 3 °C prior to the procedure. Syringes containing the VP15 hydrogel were stored in an ice-filled cooler until needed for injections.

During the procedure the heart was allowed to beat naturally, while artificial ventilation was used to regulate respiration at a rate of 12 breaths/min. Access to the apex of the heart was achieved through a subxiphoid skin incision and a second small incision in the pericardium. The surgeon was then able to place the robotic device onto the epicardium, under the pericardium, through these incisions. Once placed on the heart, the device was manually controlled using virtual image guidance in which a virtual view of the robot and anatomy were displayed to the surgeon on the control computer.

Prior to reaching the first target, both the inner and outer lumens of the injection line were kept empty, in order to limit the volume of water expelled into the pericardial space. Upon acquisition of the first target, the cooling fluid was first pumped through the system at a flow rate of 0.73 mL/s. Next, 1.5 mL of hydrogel was introduced to completely fill the inner lumen. The needle tip was then advanced into the myocardium, and 0.5 mL of cooled hydrogel was injected into the LV wall. The needle was then retracted. With the injection line filled with hydrogel and the cooling fluid continuing to flow, the robot was driven to the second injection site where another injection was performed. After the second site was injected, the robot was removed from the animal and visually inspected to ensure that no solidification of the hydrogel had occurred in the inner lumen. Saline was pushed through the injection line to ensure the line was free of occlusion. After inspection the robotic device was once again placed on the heart and the procedure was repeated for the third and fourth injection targets.

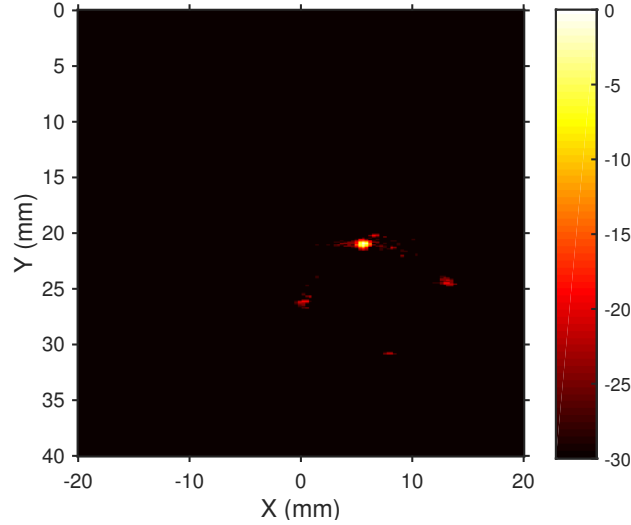


Figure 7.8: Photoacoustic imaging of patterned injections in a beating porcine heart.

Upon completion of the injections, the animal was euthanized and the heart was excised and placed in a warm saline bath. Visual inspection of the surface of the heart showed neither identifiable needle tracks nor backflow of the hydrogel.

In order to validate the successful injection of the material, photoacoustic (PA) imaging was performed to localize the hydrogel material in the excised heart. As shown in Fig. 7.8, four distinct injection sites in a square pattern can be identified near the cardiac apex under photoacoustic (PA) imaging.

Quantitative comparison of the planned and actual injection locations was done to determine the positioning accuracy of the modified injection device. The locations of the injection sites in the PA image were calculated by first segmenting the foreground pixels using k-means clustering, then computing the intensity-weighted centroid of each cluster. In order to compare the actual injection locations with the planned injection locations, the rigid registration between the imaged points and the planned points was solved using least squares. A scaling factor was also included to account for the shrinkage of the heart post mortem [98].

The observed injection sites were placed in the preoperative 3D virtual view of the

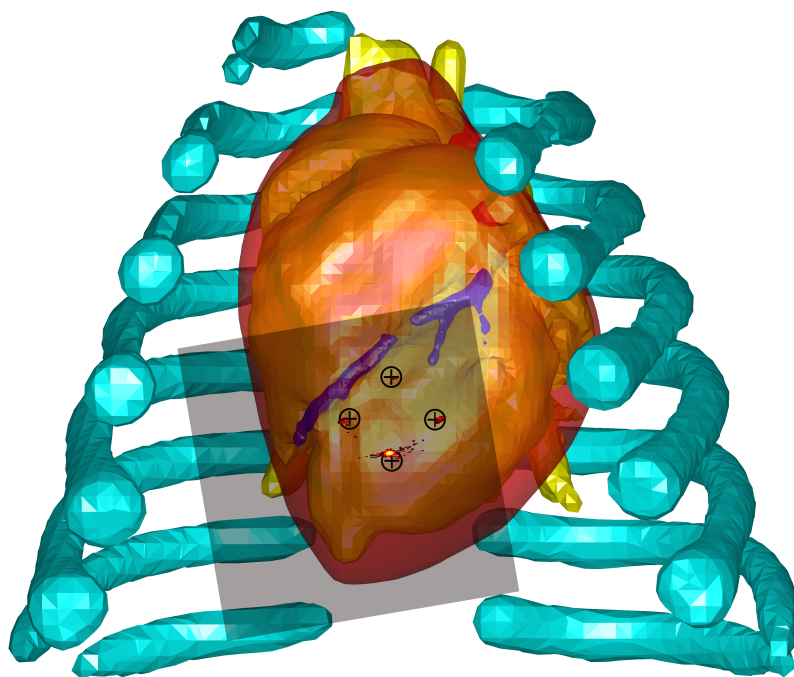


Figure 7.9: Overlay of photoacoustic image with the preplanned injection sites.

animal to compare with the pre-planned injection sites as marked by black crosses, as shown in Fig. 7.9. The overlaid PA image shows that the injection pattern accurately matches the desired pattern with a mean error of 1.4 ± 0.5 mm. Due to the artifactual reduction in size of the heart upon explant, the measured square was smaller than both that planned and recorded during the procedure. The calculated scaling factor was determined to be 1.87, meaning the excised heart size reduction post mortem was approximately 47%, which is consistent with the literature [98].

In addition to the accuracy in injection localization, reliability in depth control was also achieved, as indicated by the ability to image the 4 injection sites in the same plane with PA imaging.

Rapid hydrogel gelation limited the occurrence of diffusion in the healthy myocardium. Consistently, the injected hydrogels could be found ~ 7 mm underneath the epicardial surface in both animals undergoing the surgery. The morphological integration of the hydrogel with the myocardium was similar to that observed in the test ex vivo. Given

the angle of the injection system, 0-12.5 mm of the metallic needle was exposed to 37 °C tissue instead of being protected by cooling fluid as in the catheter. Despite this uncooled region in the needle, it was found that multiple injections of the VP15 hydrogel could be accomplished without occlusion, as in the test ex vivo.

7.4 Discussion

With the coordinated design of a thermoresponsive hydrogel and a robotic injection device employing a parallel flow cooling system we have demonstrated the ability to deliver this thermosensitive material in a minimally invasive manner which avoids the circulatory system. Design of the cooling system was achieved through simulation and water bath studies. Performance of smooth injections of the thermoresponsive hydrogel was confirmed in artificial media, tests ex vivo, and finally in beating-heart surgery in vivo. We also demonstrated the ability to accurately deliver the injections in a predetermined pattern. While the injection system was implemented in the HeartLander robot, the choice of HeartLander was due to the nature of the intervention – a tight grouping of injections. The injection system is portable and could be implemented in any organ-mounted robot.

While approximately 100 mL of saline was introduced into the pericardial space during the intervention, no negative effects were observed due to the cooling fluid. The risk of thermal shock or cardiac tamponade due to this fluid are not fully understood. Further animal experiments are necessary to further study the effects of water temperature and volume have on cardiac performance.

The ability to do interventions that require small, accurately placed groupings is the real strength of the HeartLander robot. While the locomotive capabilities theoretically give the device the ability to walk relatively large distances over the surface of the heart, it is the ability to use one foot as an anchor from which the desired targets may be acquired that is arguably the most important aspect of its design.

Chapter 8

Cerberus: A Parallel Wire Robot for Epicardial Interventions

The next emerging therapy we target with our organ-mounted paradigm is the use of gene therapy drugs for the treatment of heart failure. Heart failure (HF) is a chronic, progressively fatal disease with extremely limited interventional options. These drugs, if properly delivered, increase cardiac output, relieving the most serious symptoms of HF and enhancing quality of life.

This chapter presents the design and control of a planar parallel wire manipulator, known as Cerberus, designed specifically to provide global, homogeneous, and transmural delivery of gene therapy drugs in a minimally invasive manner. The material presented covers the entirety of our development of the robot to date [99–102].

First, Section 8.1 provides an overview of the treatment of chronic heart failure using gene therapies and the limitations of existing delivery methods. Next, Section 8.2 describes the design and control of a parallel wire robot specifically designed to enable these therapies. Finally, Section 8.3 first demonstrates the accuracy of positioning the device in benchtop experiments and then presents successful insertion, deployment, and myocardial injections in live-animal beating-heart procedures.

8.1 Gene Therapy for Congestive Heart Failure

8.1.1 Clinical Relevance

Heart failure (HF), a chronic, progressively fatal disease, is the leading cause of hospitalization in the U.S. [103]. Approximately 2.5 million Americans are classified as having advanced HF, which has a mortality rate approaching 50% at one year. The human and economic costs due to HF make it a significant public health concern.

Unfortunately, therapies for advanced HF are extremely limited and include transplantation, mechanical circulatory support, or palliative care. Currently, transplantations are limited to only 2500 advanced HF patients annually due to donor availability, mechanical support is expensive and has high associated morbidity, leaving the vast majority of patients to die receiving palliative care.

Currently, extremely promising gene drugs are in Phase II trials for HF therapies [104–108]. These investigation therapies directly increase myocyte contractility through raising intracellular calcium or adenylyl cyclase. While not ultimately curative, these trials have shown remarkably promising results.

While many promising therapeutically effective gene drugs exist, the most important challenge is the means to deliver them to the heart [109]. All of the strategies employed in clinical trials thus far limit the dispersion of gene expression [110]. Intracoronary approaches do not deliver drugs to the target in adequate amounts [111]. Injection into the myocardium may provide more efficient delivery if multiple injections can be made [111], but existing instrumentation has limited its effectiveness because of poor accuracy and coverage of the heart [110].

The major implication of the state-of-the-art in gene therapy delivery is that without an open chest, transfer of the gene is low, inconsistent, or spotty. Minimally invasive delivery that is global, homogenous, and transmural is not feasible with existing methods [112].

8.1.2 Cerberus Concept

Delivery gene drugs in a global and homogenous manner will require the ability to do many injections over large portions of the heart. Our existing robotic platform, HeartLander, excels in doing tightly controlled groups of injections, however, doing the requisite number of injections with HeartLander to cover the heart would be time-prohibitive. Addressing the particular needs presented by gene therapy requires a different approach than that of HeartLander.

In order to provide global and homogenous delivery of drugs for gene therapy, we have developed a novel organ-mounted parallel wire manipulator. This robot, known as Cerberus, combines the previously discussed advantages of an organ-mounted robot, with the advantages of parallel wire robots, including larger workspaces, higher speeds and accelerations, and lower moving masses [113].

The conceptual design for the robot, shown in Fig. 8.1, consists of a support structure comprised of three suction bases, which adhere to the surface of the heart, connected by two resilient arms. A tool head, or injector, is connected to the three bases via wires which run through each base to external control hardware. Through the coordinated actuation of the three wires, the injector can be moved anywhere within the triangle defined by the support structure.

The use of resilient arms serves two purposes. First, it allows the robot to conform to the curved surface of the heart. Also, it allows the device to collapse within a cannula, shown in Fig. 8.1(b), for subxiphoid delivery to the heart. Once advanced out of the cannula, the arms passively expand to return the device to its deployed state, and vacuum pressure applied to the suction bases attaches the device to the heart Fig. 8.1(c).

The namesake of our device from Greek mythology is a hound with three heads (suction bases), a serpent's tail (tether), a mane of snakes (cables), and the claws of a lion (injector). We know of no other case in which a planar wire robot [114] has been used as a surgical

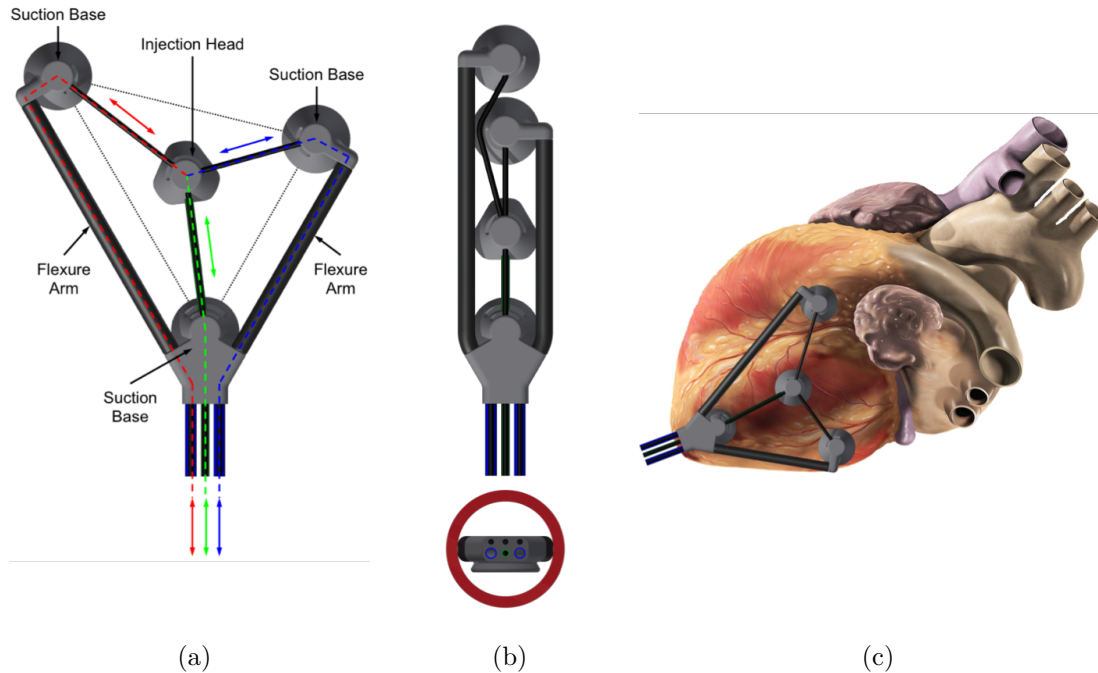


Figure 8.1: Concept for Cerberus minimally invasive parallel wire robot for gene therapies. (a) The manipulator consists of a support structure which is fixed during operation and an injection head that can be moved throughout the polygon defined by the support structure. (b) Resilient arms allow the manipulator to collapse and fit within a cannula for insertion and to expand the device into its deployed state as it exits the cannula. (c) When deployed on the heart the support structure adheres to the heart providing a stable platform. The design of the manipulator enables coverage of large portions of the heart.

robot. Non-planar wire-driven subsystems have been used as wrists for surgical robots [115, 116], and wire robots have been proposed for other biomedical applications such as patient bed transfer [117] and rehabilitation of the upper [118] and lower extremities [119].

8.2 Design and Control of Cerberus Robot

8.2.1 Hardware

A prototype Cerberus robot is shown in its deployed state in situ on a porcine heart in Fig. 8.2(a). The suction bases and injector head were constructed using rapid prototyping

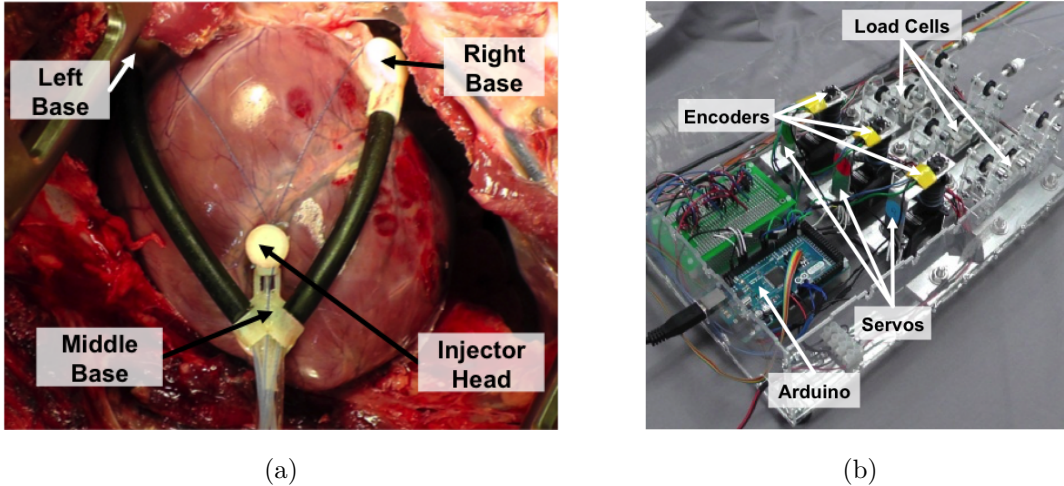


Figure 8.2: (a) Cerberus parallel wire robot for rapid accurate myocardial injection for gene therapy. The prototype is deployed on porcine heart in situ. (b) Control box with Arduino Mega 2560, continuous rotation servos, rotary encoders, load cells, and pulleys.

techniques. The arms of the support structure consist of neoprene tubes. Wires are delivered to the bases via PTFE tubes that run through each arm to decrease friction. Precise and accurate control of the tool is provided by an electronic control system, shown in Fig. 8.2(b). The low-level control system includes an Arduino Mega 2560 microcontroller, three continuous-rotation servos, and three encoders for position feedback, and load cells used to measure the tension in each wire.

8.2.2 Inverse Kinematics

Due to the parallel form of Cerberus, kinematically depicted in Fig. 8.3, no analytical solution for the forward kinematics exists. We instead consider the inverse kinematics which maps from tool pose, (\mathbf{x}, β) , to wire lengths, \mathbf{w} .

The base frame of the robot, \mathbf{B} , is defined such that it coincides with the center of the proximal suction base, with the y -axis bisecting the angle between the left and right arms. The tool frame of the robot, \mathbf{I} , is placed at the center of the injector head, with the y -axis

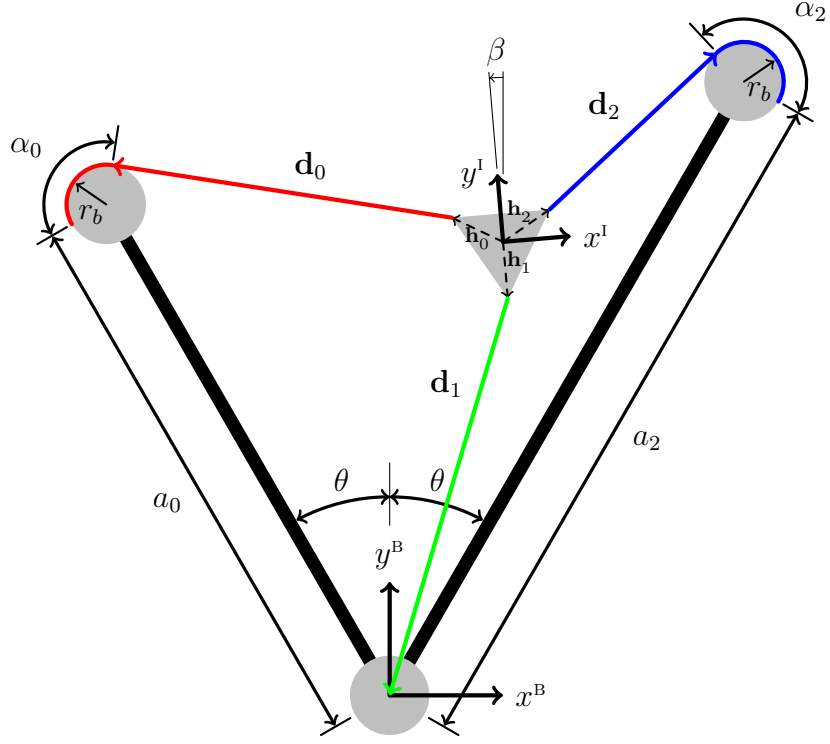


Figure 8.3: Kinematic diagram of Cerberus

defined to align with the centroid of the injector and the connection point of the middle wire. The wire lengths, \mathbf{w} , are then given by:

$$\mathbf{w} = \begin{bmatrix} w_0 \\ w_1 \\ w_2 \end{bmatrix} = \begin{bmatrix} r_b \alpha_0 + \|\mathbf{d}_0\| \\ \|\mathbf{d}_1\| \\ r_b \alpha_2 + \|\mathbf{d}_2\| \end{bmatrix}, \quad (8.1)$$

where the subscripts 0, 1, and 2 correspond to the left, middle, and right wires, r_b is the radius of the distal bases, α_i is the angle through which the i th wire wraps on the distal base, and \mathbf{d}_i is the vector from the i th wire connection point, \mathbf{h}_i to either the tangent point of the i th distal base for $i = 0$ or 2 , or the center of the proximal base for $i = 1$. Left and right wire lengths are defined from the outside points on the pulleys because the points at which the wires exit the pulleys vary through the workspace.

The wire vectors, \mathbf{d}_i , are given by:

$$\mathbf{d}_0 = a_0 \begin{bmatrix} -\sin \theta \\ \cos \theta \end{bmatrix} + \mathbf{r}_{t,0} - \mathbf{h}_0^{\text{B}} \quad (8.2)$$

$$\mathbf{d}_1 = -\mathbf{h}_1^{\text{B}} \quad (8.3)$$

$$\mathbf{d}_2 = a_2 \begin{bmatrix} \sin \theta \\ \cos \theta \end{bmatrix} + \mathbf{r}_{t,2} - \mathbf{h}_2^{\text{B}} \quad (8.4)$$

where a_i is the length of the i th arm, θ is half the angle between the two arms, $\mathbf{r}_{t,i}$ is where the wire vectors are tangent with distal bases, and \mathbf{h}_i^{B} are the locations of the wire connection points with the tool head in the base frame. These locations are calculated by transforming the locations in the tool frame, \mathbf{h}_i^{I} , by the tool pose, (x, y, β) .

$$\mathbf{h}_i^{\text{B}} = \mathbf{R}_1^{\text{B}} \mathbf{h}_i^{\text{I}} + \mathbf{x} \quad (8.5)$$

$$\mathbf{R}_1^{\text{B}} = \begin{bmatrix} \cos \beta & -\sin \beta \\ \sin \beta & \cos \beta \end{bmatrix} \quad (8.6)$$

8.2.3 Statics

The equations which describe the quasi-static state of the injector head, shown schematically in Fig. 8.4, are

$$\sum_{i=1}^2 t_i \widehat{\mathbf{d}}_i = \mathbf{0}_{2 \times 1} \quad (8.7)$$

$$\sum_{i=1}^2 t_i \widehat{\mathbf{d}}_i \times \mathbf{R}_1^{\text{B}} \mathbf{h}_i^{\text{I}} = \mathbf{0}, \quad (8.8)$$

where t_i is the tension in the i th wire, $\widehat{\mathbf{d}}_i$ is the unit vector along the i th wire, \mathbf{h}_i^{I} is the connection point of the i th wire to the injector head, and \mathbf{R}_1^{B} is the rotation matrix for

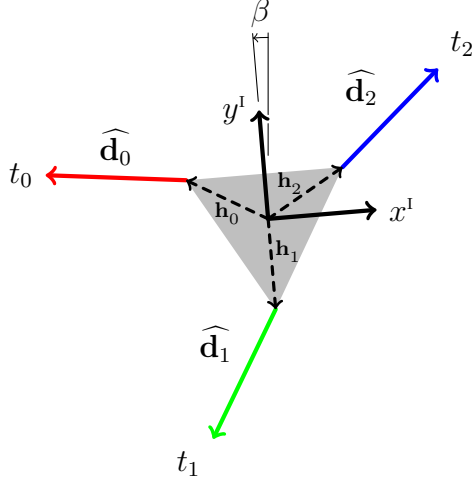


Figure 8.4: Free body diagram of injector with geometry.

the tool head rotation, β , which rotates the wire connection points into the base frame. Combining equations yields

$$\begin{bmatrix} \widehat{\mathbf{d}}_0 & \widehat{\mathbf{d}}_1 & \widehat{\mathbf{d}}_2 \\ \widehat{\mathbf{d}}_0 \times \mathbf{R}_1^{\mathbf{B}} \mathbf{h}_0^{\mathbf{I}} & \widehat{\mathbf{d}}_1 \times \mathbf{R}_1^{\mathbf{B}} \mathbf{h}_1^{\mathbf{I}} & \widehat{\mathbf{d}}_2 \times \mathbf{R}_1^{\mathbf{B}} \mathbf{h}_2^{\mathbf{I}} \end{bmatrix} \begin{bmatrix} t_0 \\ t_1 \\ t_2 \end{bmatrix} = \mathbf{0}_{3 \times 1}, \quad (8.9)$$

which we simplify to

$$\mathbf{S} \mathbf{t} = \mathbf{0}_{3 \times 1}. \quad (8.10)$$

The matrix \mathbf{S} is a function of injector pose and robot geometry and is referred to as the *structure matrix* [120]. This matrix is a force Jacobian matrix, transforming actuator forces into end-effector forces, and is the transpose of the velocity Jacobian which transforms end-effector velocities into actuator velocities [121]. \mathbf{S} is an $n \times m$ matrix, where n is the number of end-effector degrees of freedom and m is the number of actuators. In our case $n = m = 3$.

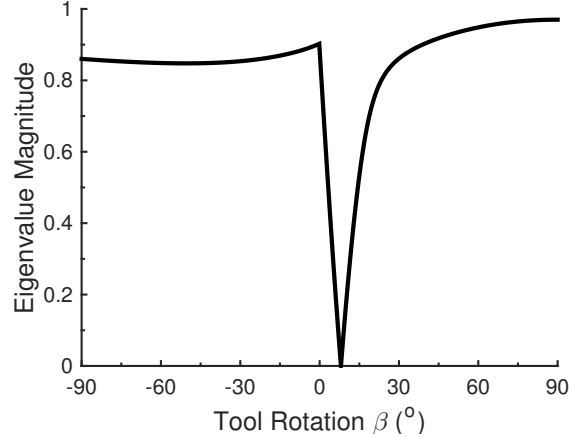


Figure 8.5: Plot showing the magnitude of the smallest eigenvalue of \mathbf{S} as a function of β . The point at which \mathbf{S} drops rank coincides with the smallest eigenvalue reaching zero. In this case $\beta = 8.07^\circ$ at $(x = 20 \text{ mm}, y = 95 \text{ mm})$.

8.2.4 Injector Rotation

Because of the structure of our device, $m = n$ for $\mathbf{h}_i \neq \mathbf{0}$, (8.10) has only the general solution, $\mathbf{t} = \mathbf{0}$, for arbitrary poses in the workspace. A non-trivial solution to (8.10) requires the injector to be in a *singular posture*.

More formally, the tensions which satisfy (8.10) lie in the null space of \mathbf{S} . A solution other than $\mathbf{t} = \mathbf{0}$ requires $\text{rank}(\mathbf{S}) < m$. The loss in rank corresponds to a singularity in the workspace of the robot, specifically in the rotation of the injector. Physically this means that we do not get to choose the orientation of the tool injector, and must instead determine the rotations which yield singular postures in order to solve the inverse kinematics and statics equations.

A plot of tool orientation versus the value of the smallest eigenvalue of the matrix \mathbf{S} for a particular location in the workspace is shown in Fig. 8.5. A drop in matrix rank occurs when an eigenvalue is zero, which occurs at only one feasible orientation for each position in the robot workspace. The tension distribution, subject to a scaling factor, is then the corresponding eigenvector for this value of β .

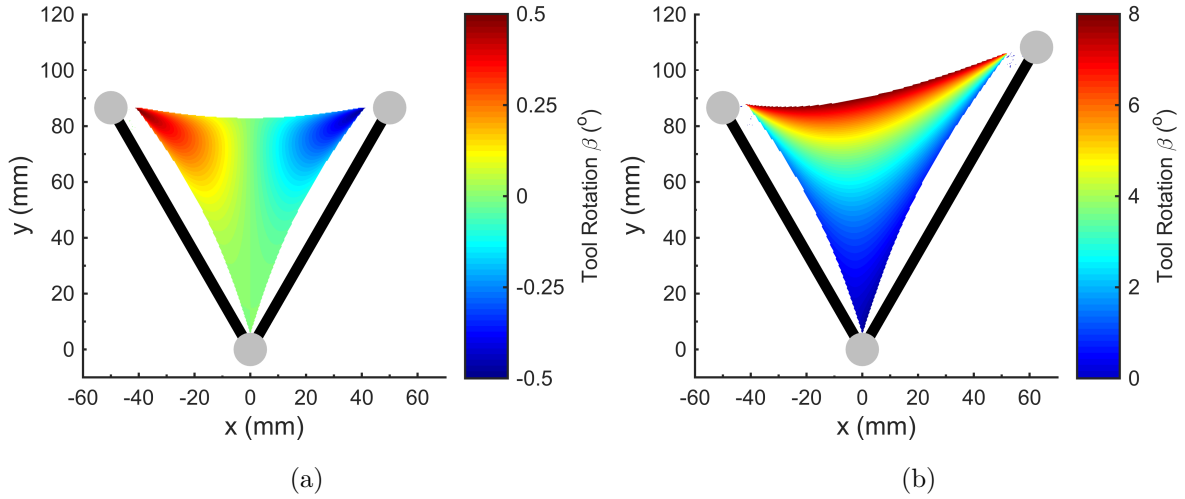


Figure 8.6: Orientation surface plots for (a) 1:1 geometry and (b) 1:1.25 geometry.

Surface plots showing the singular orientation of the injector throughout the robot workspace for both a symmetric and an asymmetric robot are shown in Fig. 8.6. For the case of a symmetric robot, shown in Fig. 8.6 (a), the injector undergoes rotations of only $\pm 0.5^\circ$ while a robot with an asymmetry of 1:1.25 in arm length will experience rotations of up to 8° .

8.2.5 Optimal Tension Distribution

With the orientation of the injector, β , resolved, we can now solve for the wire tensions which satisfy (8.10). Again, the tensions which satisfy (8.10) lie in the null space of \mathbf{S} , and with β defined as the singular rotation, the null space of \mathbf{S} is not empty. Tensions which satisfy the statics equations are of the form

$$\mathbf{t} = \alpha \mathbf{n}, \quad (8.11)$$

where \mathbf{n} is the null space of the \mathbf{S} matrix and α is a scalar weighting function.

At this time we consider the constraints we wish to apply on the forces in the system. While the design of the robot itself only allows for tensile forces, we wish to further constrain

these forces to ensure safety as well as accurate positioning. Allowing a wire to go slack ($t_i = 0$) disrupts the ability to accurately control the position of the tool, while forces which are too large may result in loss of traction, destruction of the robot, or dangerous compression of the heart. We therefore impose the following constraint on wire tension.

$$t_{\min} \leq t_i \leq t_{\max}, \forall i \quad (8.12)$$

As the system is redundantly actuated, any scalar multiple of the solution will also be a solution. The “optimal” tensions in this case are found by minimizing the total sum of tensions, which is achieved using the following metric.

$$\mathbf{t}^* = \frac{t_{\min}}{\min(\mathbf{n})} \mathbf{n} \quad (8.13)$$

It is important to note here that any point in the workspace that returns a negative tension will lie outside the convex hull of the support triangle, and any point in which (8.12) is not satisfied, although lying inside this polygon, is not in the reachable workspace.

Computed optimal wire tensions for a symmetric robot are shown in Fig. 8.7. Wire tensions are at their minimum in the portion of the triangle opposite the wire’s base, and reach their maximum at the edges, adjacent to the wires base. These large tensions occur as the angle between adjacent wires approaches 180° .

Plots of the tension ratios, $\max(\mathbf{t}) / \min(\mathbf{t})$, for both symmetric and asymmetric robots are shown in Fig. 8.8. As the ratio of maximum allowable tension to the minimum allowable tension decreases, the workspace of the robots will be decreased.

8.2.6 Control System

In order to control both the position of the injector, as well as the tensions applied by each cable, a parallel force/position control scheme was implemented, shown in Fig. 8.9. The input to the controller is the desired Cartesian position of the tool in the base frame

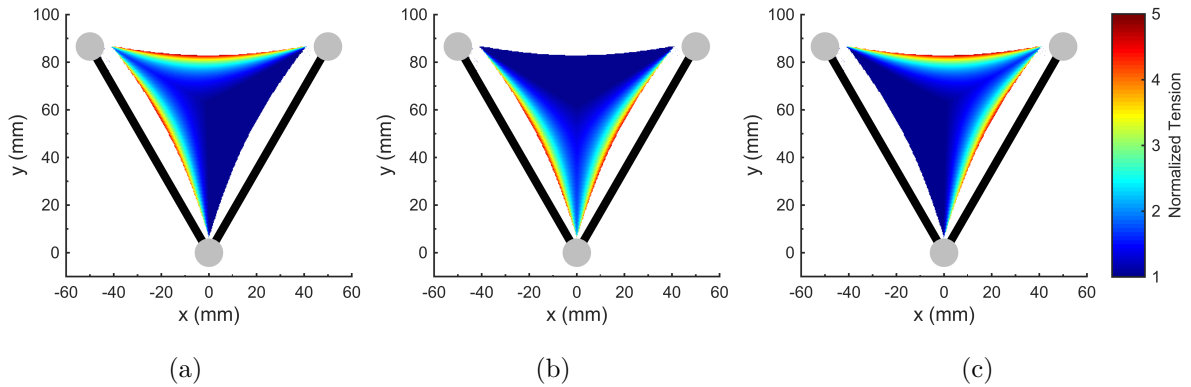


Figure 8.7: Normalized tensions for Cerberus robot for (a) left wire, (b) middle wire, and (c) right wire.

coordinates. The previously derived inverse kinematics and statics equations are used to compute the desired wire tensions and lengths, which are then fed to parallel control loops.

8.3 Experiments

8.3.1 Control Experiments

For the purposes of this experiment, a desktop setup was designed capable of fixing the three bases of the robot to a planar surface while allowing variation of the lengths and angles of the arms at known values as shown in Fig. 8.10(a). A Pixy camera (Charmed Labs, Austin, TX) was mounted directly overhead to capture all possible configurations within the camera’s field of view. Ground truth was established using the camera’s color tracking software via markers on the bases and injector. The camera is only used to quantify error, not in the actual control system.

In order to quantify the performance of the previously described control approach, experiments were conducted for two different robot geometries as well as two different controllers. The two geometries tested were a symmetric robot defined by $\theta = 30^\circ$ and $a_0 = a_2 = 100$ mm and an asymmetric robot defined by $\theta = 30^\circ$, $a_0 = 100$ mm, and $a_2 =$

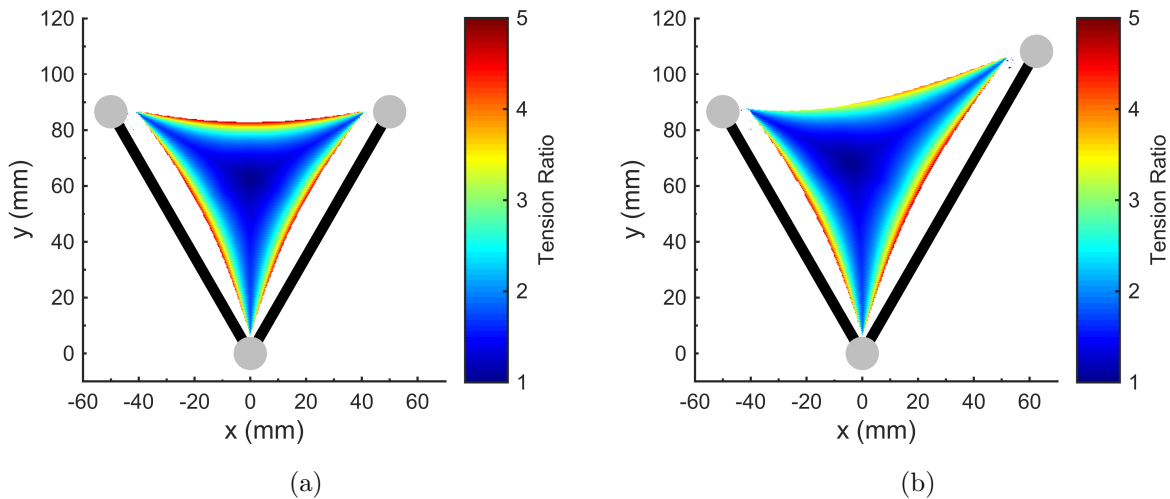


Figure 8.8: Tension ratio ($\max(\mathbf{t}) / \min(\mathbf{t})$) surface plots for (a) 1:1 geometry and (b) 1:1.25 geometry.

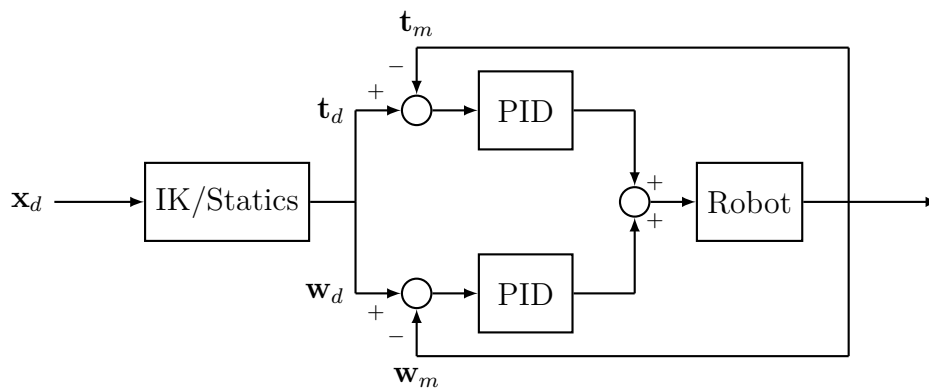


Figure 8.9: Control diagram for parallel force/position control.

125 mm. The first controller implemented used only position control, while the second used both position and tension control.

For each controller and geometry combination the robot was commanded to move the tool head sequentially to a triangular array of points throughout the reachable workspace, as shown in Fig. 8.10(b). This testing method was chosen to closely replicate the operating conditions intended for this robot, in which many injections are done in quick succession. Once the controller has reached its desired target, the overhead camera is used to collect ground-truth position measurements. A single trial consists of targeting 43 points, with a

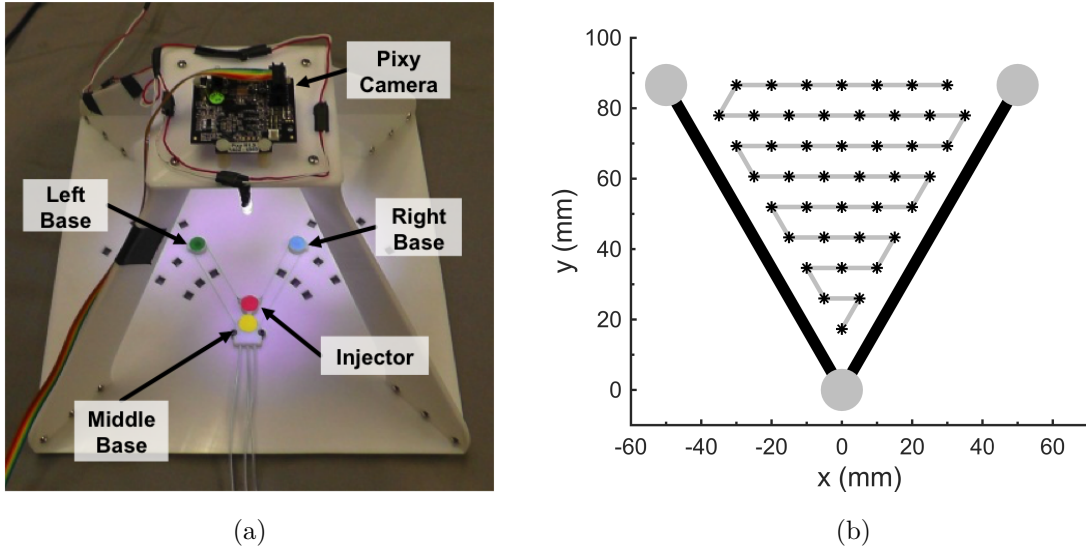


Figure 8.10: (a) Planar robot setup with colors for tracking. Bases with colors green, yellow, blue correspond to index numbers 0, 1, and 2, respectively. The red color covers the tool. (b) Desired injector path for control experiments with injection points denoted by a black star.

total of 10 trials run for each controller-robot pair.

Mean and standard error of the 2D positioning error for the various control schemes for the symmetric and asymmetric geometries are shown in Fig. 8.11. For both controllers, the error for the symmetric geometry is smaller than for the asymmetric case. For each geometry, mean positioning error decreases when force control is added.

8.3.2 Beating Heart Injections in Porcine Model

The manipulator was tested in vivo in a porcine model ($N = 3$) under a board-approved protocol. The device was inserted using subxiphoid access and tested for deployment, movement of the injection head, and injection. Fluoroscopy was used to visualize the device during operation. Small stainless steel washers were embedded in each suction base, as well as the injection head, to aid in visualization.

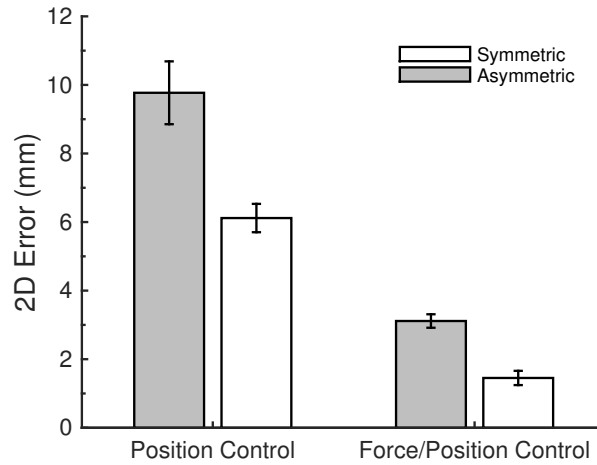


Figure 8.11: Mean 2D control error of different controllers for 1:1 geometry and 1:1.25 geometry. Error bars indicate 95% confidence interval from standard error.



Figure 8.12: Subxiphoid insertion of Cerberus robot in live animal experiment

Insertion Access to the pericardial space was achieved via a subxiphoid skin incision and a small incision in the pericardial sac near the apex of the heart. Prior to insertion the interior surface of the cannula was coated with surgical lubricant to reduce friction with the device. The device was collapsed and inserted into the cannula, which was then inserted into the pericardial space, as shown in Fig. 8.12(a). The device was then manually advanced into the pericardial space using surgical forceps and the cannula was retracted, as shown in Fig. 8.12(b).

Deployment Fluoroscopic visualization was used to confirm deployment of the device, as shown in Fig. 8.13. In two of three experiments the arms passively deployed as they exited the cannula satisfactorily. In the third experiment, however, the arms did not deploy sufficiently and were manually deployed by the surgeon. Once deployment and positioning of the device were confirmed suction was provided to the bases to adhere to the surface of the heart.

Tool Motion After deployment onto the heart, images and video were captured on the fluoroscope demonstrating the motion capabilities of the manipulator, as shown in Fig. 8.13. The injection head moved easily beneath the pericardium. The tool was moved to each base and viewed under fluoroscope to ensure the correct position. Postoperatively, a sternotomy revealed the device deployed under the pericardium, and movements were executed to ensure electronic control was achieved.

Injections During each procedure, injection into the myocardium was demonstrated. For each injection a PTFE lumen with a 23-gauge needle tip was advanced approximately 5 mm through a PTFE sheath embedded in the tool head. Water-based ink (0.1 mL)

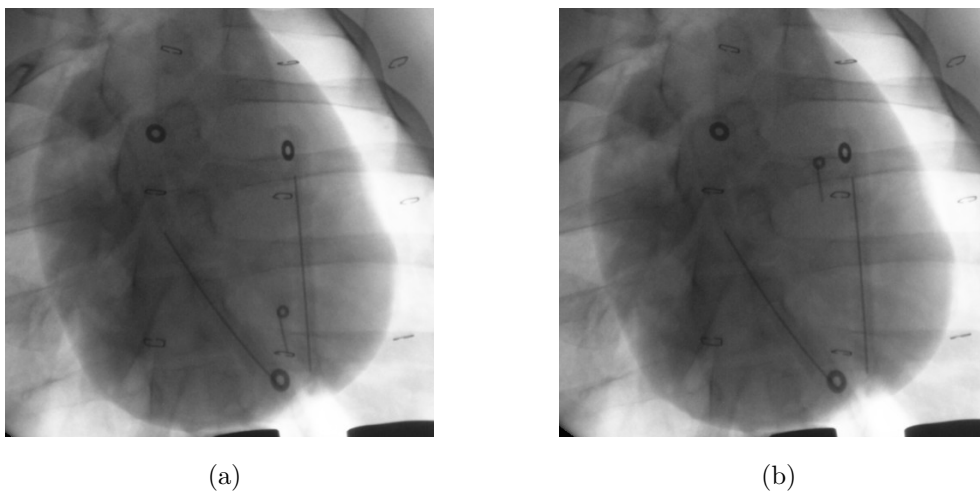


Figure 8.13: Fluoroscopic images of the Cerberus robot deployed on the beating heart.



Figure 8.14: Injections of water-based ink in the left ventricle using the Cerberus robot.

was injected into the myocardium, allowing injections to be identified post-operatively. During the final procedure, 6 injections of water-based ink (0.1 mL) were delivered to the myocardium of the left ventricle (LV). Grouping the injections on the LV allows for coverage of a large portion of the ventricle, as shown on the excised heart in Fig. 8.14.

8.4 Discussion

In this chapter we presented our work on the design, control, and demonstration of a parallel wire robot, known as Cerberus, for delivery of gene therapy to the beating heart. Our first major contribution in this work was the solution for the singularity manifold the tool must lie on to achieve quasi-static equilibrium. The uncontrollable rotation of the tool head was shown to be insignificant for symmetric robot geometries, however in the case of an asymmetric robot the tool rotation must be accounted for.

Next we presented a solution for the optimal tension distribution in the wires which minimized the total wire tension. Using the inverse kinematics and statics solutions we

then implemented a parallel force/position control scheme to accurately control the tool location to almost 1 mm accuracy in benchtop experiments. Finally, we demonstrated the capability to insert, deploy, and perform injections during live-animal beating-heart procedures (N=3).

The results presented in this section are essentially a proof-of-concept for the parallel wire robot concept applied to minimally invasive surgery. Although the device and control instrumentation was constructed on a shoestring budget, the device demonstrated its potential in providing fast and accurate interventions to the beating heart.

Part III

Conclusions and Future Work

Chapter 9

Conclusions

The work presented in this thesis strives to provide better patient care in cardiac surgery by expanding the capabilities of *organ-mounted robots*. We expanded the reach of organ-mounted robots in two ways – enabling more accurate interventions through virtual image guidance techniques, and enabling new interventions with the design of new robots.

Our initial contribution was providing more accurate interventions for organ-mounted robots. First we developed motion models which accurately describe the 6-DOF periodic motion of the robots on the surface of the heart, characterized their performance, and demonstrated their online estimation. The models were validated on data from live-animal closed-chest beating-heart experiments. Next we developed an empirical metric for performing spatiotemporal registration of static preoperative models of the heart with the periodic robot motion. This effort relied on data from (N=6) live-animal closed-chest beating-heart experiments. Finally we introduced the use of radial basis function approximation to provide more accurate estimates of robot pose over short time horizons.

Our next contribution was the delivery of a *thermosensitive hydrogel* in a targeted pattern to myocardium in a live-animal closed-chest beating-heart procedure. This material transitions from a liquid to gel well below body temperature and required the implementation of an actively cooled injection system.

Finally, we presented the design and control of a surgical parallel wire robot called Cerberus. Once again we demonstrated the ability to effectively deploy and deliver interventions in live-animal closed-chest beating-heart procedures. The theoretical contributions of this work included the solution for the *persistent singular pose* of the robot that enables static force equilibrium.

Perhaps the most important takeaway from this thesis is the wide array of capabilities that are possible using an organ-mounted approach, both in localization accuracy and in robot form factor. Depending upon the requirements of the intended intervention, the approach taken during virtual image guidance may vary significantly. If ~ 5 mm positioning accuracy is sufficient for the intended intervention it is likely not necessary to spend the time required to accurately perform spatiotemporal registration, and sufficient accuracy can be achieved by filtering the periodic motion out as noise.

Extending capabilities beyond 5 mm positioning accuracy requires collecting more data prior to performing the intervention. This trade-off between speed and accuracy is really what must be considered for clinical application. For those interventions requiring high accuracy, we envision the procedure being conducted in two stages – registration followed by intervention. Using the Lamprey robot as a measurement probe, time traces of points on the surface of the heart can be collected until registration has converged. After registration the intervention could then be performed using either Lamprey or HeartLander.

Interventions requiring ~ 2 mm positioning accuracy could be performed using Lamprey in a semiautonomous mode in which the clinician manually moves the robot over the surface of the heart, and suction is automatically engaged when the device is on an intended intervention site. Using the radial basis function localization method, we demonstrated the ability to instantaneously localize using only ~ 20 samples spread over the heart. Acquiring this number of samples can be done in less than 10 minutes.

Further increasing positioning accuracy will require the use of HeartLander as well as

more time to enable motion models to converge and provide more accurate estimates of position. In this most accurate operation mode, the relative positioning capabilities of HeartLander can be used to perform the small motions required to accurately position the device. Once again, the tradeoff that must be weighed is speed versus accuracy.

The Cerberus robot is a bit of an outlier, in the sense that many of the assumptions made to solve for registration likely will not hold. The large footprint of the device likely deforms the heart; however, if a large number (tens) of injections are required over a large area, Cerberus is likely the best solution. While the registration methods presented are likely not possible with Cerberus on the heart, if very high accuracy is required, we believe that we could accurately register the heart using Lamprey to provide accurate knowledge of the initial position of Cerberus on the heart. If high accuracy is not required, we believe that placing the device under medical image guidance may be the best solution.

Our final perspective on the contributions of this thesis is that performing interventions on a blood-filled soft tissue organ under continuous motion is a difficult. We strongly believe that myocardial injections are the “killer app” for organ-mounted robots due to the safety ensured by attaching to the surface of the heart and the ability to deliver them in a minimally invasive fashion.

Chapter 10

Future Work

This thesis makes contributions to the state estimation, design, and control of organ-mounted robots for minimally invasive beating-heart surgery. In each of the presented areas there are extensions or new directions which may merit further exploration.

10.1 Virtual Image Guidance

The most pressing need in the ongoing development of virtual image guidance for organ-mounted robots is the demonstration of the methods in survival experiments for providing accurate ground-truth positioning performance. This data is extremely difficult to collect in sacrificial experiments for a variety of reasons including the change in the shape of the heart after being excised, difficulty in leaving identifiable surface markings on the heart, and the lack of surface features to enable localizing surface markings postoperatively. Survival experiments in which a material that is easily identifiable in medical imaging is injected into the myocardium would provide an easier path to establishing ground truth performance. We understand that this is no small task; however, at some point it will be necessary to advance these robots to clinical relevance.

Separate from the clinical aspects of this work are a number of potential improvements

to the presented motion modeling, registration, and localization methods. First, the work presented essentially only provides estimates of the mean, ignoring higher order statistics. There exist natural extensions to estimate the uncertainty at each step. Instead of using recursive least-squares to estimate the Fourier series parameters, Kalman filters could be used to provide estimates of uncertainty of all state variables. Kalman filtering based approaches could similarly be employed to estimate the uncertainty in registration [122, 123]. Finally, Gaussian process regression are a natural extension to the radial basis function regression used for interpolation.

These natural extensions to the presented work may enable providing surgeons with more accurate estimates of position as well as bounds on these estimates. Uncertainty in the system may also be employed to speed up the registration process by guiding the sampling of points on the surface of the heart which provide the most information, or to guide denser sampling of areas that are targeted by an intervention.

10.2 Cooled Injection

Once again, the most pressing need for the continued development of cooled injection capabilities is further studies in animal models. While no negative effects were observed due to the cooling fluid, the risk of thermal shock or cardiac tamponade are not fully understood. Also, demonstration of injection into infarct models may provide the necessary challenge to demonstrate the localization capabilities of the system. Improvements to the design of the cooling system may include a recirculation pathway using the vacuum lines to the feet, embedding miniature thermocouples in the cooling system to enable automatic control, and automating the injection system.

10.3 Cerberus

In our view, Cerberus presents the most interesting research challenges moving forward. The work presented on Cerberus in this thesis is essentially proof-of-concept for the device, which is still in its infancy. The design of the robot and control system assumed the device was planar. This assumption was not grossly violated with early prototypes; however, the geometry of recent prototypes will require further development of the kinematics, statics, and control system. In order to provide more complete coverage of the left ventricle, in the most recent Cerberus prototype the three suction bases are rotated 90° so that the main base attaches to the apex of the heart while the distal bases attach to the anterior and posterior surfaces.

The change in geometry opens several avenues which must be studied. First, the kinematics and statics of the device must be extended to curved surfaces. The statics solution presented in this thesis only considered forces tangent to the surface, but with the modified geometry the normal forces applied to the heart must be carefully controlled to not risk tamponade. The simple kinematics must also be embedded on the curved surface.

Accounting for the curvature of the surface is only a step towards the final goal of controlling the device on periodically deforming curved surface. As the heart contracts, the shape of the heart, and in turn the geometry of the robot, will change. Controlling the injector head to remain at a fixed point on the moving heart will likely require embedding electromagnetic position sensors in the robot, modeling the periodic deformation of each base using the motion modeling techniques presented in this thesis, and using these models to generate feed-forward signals for wire length and tension control.

Separate from the development of more accurate control schemes, further development of the hardware and method of delivery to the heart will be required. As Cerberus violates several of the assumptions made for our virtual image guidance scheme, we envision the insertion and positioning of this device being done manually under medical imaging

guidance. Development of the mechanisms by which this manual positioning is achieved remains an open problem.

Bibliography

- [1] M. Vinall, “Minimally Invasive Cardiac Surgery,” *Curr. Probl. Surg.*, vol. 34, no. 9, p. 34, 2011. 1, 2.3.1, 2.3.2
- [2] L. Cohn, *Cardiac Surgery in the Adult*. McGraw Hill Professional, 2011. 1
- [3] R. Ascione, C. T. Lloyd, M. J. Underwood, A. A. Lotto, A. A. Pitsis, and G. D. Angelini, “Inflammatory response after coronary revascularization with or without cardiopulmonary bypass,” *Ann. Thorac. Surg.*, vol. 69, no. 4, pp. 1198–1204, 2000. 1, 2.3.1
- [4] M. J. Mack, “Minimally invasive and robotic surgery,” *JAMA*, vol. 285, no. 5, pp. 568–572, 2001. 1, 2.3.1
- [5] M. F. Newman, J. L. Kirchner, B. Phillips-Bute, V. Gaver, H. Grocott, R. H. Jones, D. B. Mark, J. G. Reves, and J. a. Blumenthal, “Longitudinal assessment of neurocognitive function after coronary-artery bypass surgery,” *N. Engl. J. Med.*, vol. 344, no. 6, pp. 395–402, 2001. 1, 2.3.1
- [6] C. Borst, E. W. Jansen, C. A. Tulleken, P. F. Gründeman, H. J. Mansvelt Beck, J. W. van Dongen, K. C. Hodde, and J. J. Bredée, “Coronary artery bypass grafting without cardiopulmonary bypass and without interruption of native coronary flow using a novel anastomosis site restraining device (“Octopus”),” *J. Amer. Coll. Cardiol.*, vol. 27, no. 6, pp. 1356–64, may 1996. 1, 1.1, 2.3.2
- [7] E. W. Jansen, J. R. Lahpor, C. Borst, P. F. Gründeman, and J. J. Bredée, “Off-pump coronary bypass grafting: how to use the Octopus Tissue Stabilizer.” *Ann. Thorac. Surg.*, vol. 66, no. 2, pp. 576–579, aug 1998. 1, 1.1, 2.3.2, 2.4.1
- [8] V. Falk, “Robotic surgery,” in *Minimal Access Cardiothoracic Surgery*. Philadelphia: W. B. Saunders, 1999, p. 623. 1, 2.3.2
- [9] F. Yanagawa, M. Perez, T. Bell, R. Grim, J. Martin, and V. Ahuja, “Critical outcomes in nonrobotic vs robotic-assisted cardiac surgery,” *JAMA Surgery*, vol. 150, no. 8, pp. 771–7, aug 2015. 1, 2.3.2
- [10] T. H. Liem, L. H. D. J. Booij, M. A. W. M. Hasenbos, and M. J. M. Gielen, “Coronary artery bypass grafting using two different anesthetic techniques: Part I: Hemodynamic results,” *J. Cardiothorac. Vasc. Anesth.*, vol. 6, no. 2, pp. 148–155, 1992. 1.1, 2.3.1
- [11] J. P. Williams, E. A. Sullivan, and H. Ramakrishna, “Effects of thoracic epidural

- anaesthesia on the coagulation system,” *Clin. Anaesth.*, vol. 13, pp. 31–56, 1999. 1.1, 2.3.1
- [12] R. Dzwonczyk, C. L. del Rio, C. Sai-Sudhakar, J. H. Sirak, R. E. Michler, B. Sun, N. Kelbick, and M. B. Howie, “Vacuum-assisted apical suction devices induce passive electrical changes consistent with myocardial ischemia during off-pump coronary artery bypass graft surgery,” *Eur. J. Cardiothorac. Surg.*, vol. 30, pp. 873–876, 2006. 1.1, 2.3.2
- [13] S. Kinjo, J. Tokumine, K. Sugahara, M. Kakinohana, K. Iha, H. Matsuda, M. Akasaki, and S. Yamashiro, “Unexpected hemodynamic deterioration and mitral regurgitation due to a tissue stabilizer during left anterior descending coronary anastomosis in off-pump coronary artery bypass graft surgery,” *Ann. Thorac. Surg.*, vol. 11, no. 5, pp. 324–328, 2005. 1.1, 2.3.2
- [14] V. Falk, A. Diegler, T. Walther, R. Autschbach, and F. W. Mohr, “Developments in robotic cardiac surgery,” *Curr. Opin. Cardiol.*, vol. 15, no. 6, pp. 378–87, nov 2000. 1.1, 2.3.1, 2.3.2
- [15] M. Lemma, A. Mangini, A. Redaelli, and F. Acocella, “Do cardiac stabilizers really stabilize? Experimental quantitative analysis of mechanical stabilization,” *Interact. Cardiovasc. Thorac. Surg.*, vol. 4, no. 3, pp. 222–6, 2005. 1.1, 2.3.2
- [16] M. L. Koransky, M. L. Tavana, A. Yamaguchi, M. H. Kown, D. N. Miniati, W. Nowlin, and R. C. Robbins, “Quantification of mechanical stabilization for the performance of off-pump coronary artery surgery.” *Heart Surg. Forum*, vol. 6, no. 4, pp. 224–31, 2003. 1.1, 2.3.2
- [17] M. L. Buja and G. R. F. Krueger, *Netter’s Illustrated Human Pathology*. Saunders, 2004. 1.1, 2.3.1
- [18] M. A. Zenati, G. Bonanomi, A. K. Chin, and D. Schwartzman, “Left heart pacing lead implantation using subxiphoid videopericardioscopy.” *J. Cardiovasc. Electrophysiol.*, vol. 14, no. 9, pp. 949–53, 2003. 1.1, 2.4.1
- [19] K. Soejima, G. Couper, J. M. Cooper, J. L. Sapp, L. M. Epstein, and W. G. Stevenson, “Subxiphoid surgical approach for epicardial catheter-based mapping and ablation in patients with prior cardiac surgery or difficult pericardial access,” *Circulation*, vol. 110, no. 10, pp. 1197–201, sep 2004. 1.1
- [20] N. A. Patronik, “A miniature mobile robot for precise and stable access to the beating heart,” Ph.D. Thesis, Carnegie Mellon University, 2008. 1.3, 2.4.1
- [21] D. M. Nelson, Z. Ma, K. L. Fujimoto, R. Hashizume, and W. R. Wagner, “Intra-myocardial biomaterial injection therapy in the treatment of heart failure: materials, outcomes and challenges,” *Acta Biomaterialia*, vol. 7, no. 1, pp. 1–15, jan 2011. 1.3, 7.1.1
- [22] H. Gray, *Anatomy of the Human Body*. Lea & Febiger, 1918. 2.1
- [23] G. Shechter, J. R. Resar, and E. R. McVeigh, “Displacement and velocity of the coronary arteries: cardiac and respiratory motion,” *IEEE Trans. Med. Imag.*,

- vol. 25, no. 3, pp. 369–375, 2006. 2.2, 2.2, 3.3.1, 5.2
- [24] T. Ota, N. A. Patronik, D. Schwartzman, C. N. Riviere, and M. A. Zenati, “Minimally invasive epicardial injections using a novel semiautonomous robotic device.” *Circulation*, vol. 118, no. 14 Suppl, pp. S115–20, 2008. 2.4.1
- [25] N. A. Patronik, T. Ota, M. A. Zenati, and C. N. Riviere, “A miniature mobile robot for navigation and positioning on the beating heart,” *IEEE Trans. Robot.*, vol. 25, no. 5, pp. 1109–1124, 2009. 2.6, 2.4.1
- [26] N. A. Patronik, T. Ota, C. N. Riviere, and M. A. Zenati, “Synchronization of epicardial crawling robot with heartbeat and respiration for improved safety and efficiency of locomotion,” *Int. J. Med. Robot. Comput. Assist. Surg.*, vol. 8, no. 1, pp. 97–106, 2012. 2.4.1
- [27] R. K. Li, Z. Q. Jia, R. D. Weisel, F. Merante, and D. A. Mickle, “Smooth muscle cell transplantation into myocardial scar tissue improves heart function,” *J. Mol. Cell. Cardiol.*, vol. 31, no. 3, pp. 513–22, 1999. 2.4.1
- [28] D. W. Losordo, P. R. Vale, J. F. Symes, C. H. Dunnington, D. D. Esakof, M. Maysky, A. B. Ashare, K. Lathi, and J. M. Isner, “Gene therapy for myocardial angiogenesis: initial clinical results with direct myocardial injection of phVEGF165 as sole therapy for myocardial ischemia,” *Circulation*, vol. 98, no. 25, pp. 2800–2804, 1998. 2.4.1
- [29] J. D. Gleason, K. P. Nguyen, K. V. Kissinger, W. J. Manning, and R. L. Verrier, “Myocardial drug distribution pattern following intrapericardial delivery: an MRI analysis,” *J. Cardiovasc. Magn. Reson.*, vol. 4, no. 3, pp. 311–316, 2002. 2.4.1
- [30] C. Leclercq and D. A. Kass, “Retiming the failing heart: principles and current clinical status of cardiac resynchronization,” *J. Am. Coll. Cardiol.*, vol. 39, no. 2, pp. 194–201, 2002. 2.4.1
- [31] R. Lee, T. Nitta, R. B. Schuessler, D. C. Johnson, J. P. Boineau, and J. L. Cox, “The closed heart MAZE: a nonbypass surgical technique,” *Ann. Thorac. Surg.*, vol. 67, no. 6, pp. 1696–702, 1999. 2.4.1
- [32] T. Ota, N. A. Patronik, D. Schwartzman, C. N. Riviere, and M. A. Zenati, “Subxiphoid epicardial pacing lead implantation using a miniature crawling robotic device,” *J. Surg. Res.*, vol. 137, no. 2, pp. 242–243, 2007. 2.4.1, 2.8
- [33] C. A. Linte, J. White, R. Eagleson, G. M. Guiraudon, and T. M. Peters, “Virtual and augmented medical imaging environments: enabling technology for minimally invasive cardiac interventional guidance.” *IEEE Rev. Biomed. Eng.*, vol. 3, pp. 25–47, jan 2010. 2.5, 2.6.1, 2.6.3, 5.4
- [34] R. A. Omary, J. D. Green, B. E. Schirf, Y. Li, J. P. Finn, and D. Li, “Real-time magnetic resonance imaging-guided coronary catheterization in swine,” *Circulation*, vol. 107, no. 21, pp. 2656–9, jun 2003. 2.5
- [35] E. R. McVeigh, M. a. Guttman, R. J. Lederman, M. Li, O. Kocaturk, T. Hunt, S. Kozlov, and K. a. Horvath, “Real-time interactive MRI-guided cardiac surgery:

- aortic valve replacement using a direct apical approach.” *Mag. Res. Med.*, vol. 56, no. 5, pp. 958–64, 2006. 2.5, 2.8
- [36] Y. Suematsu, G. R. Marx, J. A. Stoll, P. E. DuPont, R. O. Cleveland, R. D. Howe, J. K. Triedman, T. Mihaljevic, B. N. Mora, B. J. Savord, I. S. Salgo, and P. J. del Nido, “Three-dimensional echocardiography-guided beating-heart surgery without cardiopulmonary bypass: a feasibility study.” *J. Thorac. Cardiovasc. Surg.*, vol. 128, no. 4, pp. 579–87, oct 2004. 2.5
- [37] D. A. Jaffray, J. H. Siewerdsen, J. W. Wong, and A. A. Martinez, “Flat-panel cone-beam computed tomography for image-guided radiation therapy.” *Int. J. Rad. Onc. Biol. Phys.*, vol. 53, no. 5, pp. 1337–49, aug 2002. 2.5
- [38] S. Tully, G. Kantor, M. A. Zenati, and H. Choset, “Shape estimation for image-guided surgery with a highly articulated snake robot,” in *IEEE/RSJ Int. Conf. Intell. Robot. Sys. (IROS)*, sep 2011, pp. 1353–1358. 2.6, 2.9, 3.3.2
- [39] S. Tully, G. Kantor, and H. Choset, “Inequality constrained Kalman filtering for the localization and registration of a surgical robot,” in *IEEE/RSJ Int. Conf. Intell. Robot. Sys. (IROS)*, sep 2011, pp. 5147–5152. 3.3.2
- [40] A. Brij Koolwal, F. Barbagli, C. Carlson, and D. Liang, “An ultrasound-based localization algorithm for catheter ablation guidance in the left atrium,” *Int. J. Robot. Res.*, vol. 29, no. 6, pp. 643–665, jun 2009. 2.6, 3.3.2
- [41] W. Niessen, “Model-based image segmentation for image-guided interventions,” in *Image-Guided Interventions: Technology and Applications*, T. M. Peters and K. Cleary, Eds. Heidelberg, Germany: Springer, 2008, ch. 8, pp. 219–240. 2.6.1
- [42] T. Peters and K. Cleary, *Image-Guided Interventions: Technology and Applications*, Heidelberg, Germany, 2008. 2.6.3
- [43] K. S. Arun, T. S. Huang, and S. D. Blostein, “Least-squares fitting of two 3-D point sets,” *IEEE Trans. Patt. Anal. Mach. Intell.*, vol. 9, no. 5, pp. 698–700, 1987. 2.6.3, 2.7.4
- [44] B. K. P. Horn, “Closed-form solution of absolute orientation using unit quaternions,” *J. Optic. Soc. Amer.*, vol. 4, no. April, 1987. 2.6.3
- [45] S. Lavallée, P. Merloz, E. Stindel, P. Kilian, J. Troccaz, P. Cinquin, F. Langlotz, and L. P. Nolte, “Echomorphing introducing an intra-operative imaging modality to reconstruct 3d bone surfaces for minimally invasive surgery,” *4th Ann. Meet. Int. Soc. Comput. Ass. Ortho. Surg.*, pp. 38–39, 2004. 2.6.3
- [46] J. L. Herring, B. M. Dawant, C. R. Maurer, D. M. Muratore, R. L. Galloway, and J. M. Fitzpatrick, “Surface-based registration of CT images to physical space for image-guided surgery of the spine: a sensitivity study,” *IEEE Trans. Med. Imag.*, vol. 17, no. 5, pp. 743–752, 1998. 2.6.3
- [47] P. J. Besl and N. D. McKay, “A method for registration of 3-D shapes,” *IEEE Trans. Patt. Anal. Mach. Intell.*, vol. 14, no. 2, pp. 239–256, 1992. 2.6.3, 5.1, 5.3.1
- [48] B. Desjardins and E. A. Kazerooni, “ECG-Gated Cardiac CT,” *Am. J. Roentgenol-*

- ogy, vol. 182, no. 4, pp. 993–1010, 2004. 2.7.1, 5.1
- [49] P. Cignoni, M. Callieri, M. Corsini, M. Dellepiane, F. Ganovelli, and G. Ranzuglia, “MeshLab: an open-source mesh processing tool,” in *6th Eurographics Italian Chapter Conf.*, 2008, pp. 129–136. 2.7.1
- [50] J. Pan and W. J. Tompkins, “A real-time QRS detection algorithm,” *IEEE Trans. Biomed. Eng.*, vol. 32, no. 3, pp. 230–236, 1985. 2.7.3
- [51] W. Bachta, P. Renaud, L. Cuvillon, E. Laroche, A. Forgione, and J. Gangloff, “Motion prediction for computer-assisted beating heart surgery,” *IEEE Trans. Biomed. Eng.*, vol. 56, no. 11, pp. 2551–63, 2009. 3.3.1, 4, 4.1, 4.2, 4.2, 4.8
- [52] C. Riviere, J. Gangloff, and M. de Mathelin, “Robotic compensation of biological motion to enhance surgical accuracy,” *Proc. IEEE*, vol. 94, no. 9, pp. 1705–1716, 2006. 3.3.1
- [53] T. Ortmaier, M. Gröger, D. H. Boehm, V. Falk, and G. Hirzinger, “Motion estimation in beating heart surgery,” *IEEE Trans. Biomed. Eng.*, vol. 52, no. 10, pp. 1729–1740, 2005. 3.3.1
- [54] M. Çavusoglu, J. Rotella, W. Newman, J. Ustin, and S. Sastry, “Control algorithms for active relative motion cancelling for robotic assisted off-pump coronary artery bypass graft surgery,” in *Int. Conf. Adv. Robot. (ICAR)*, 2005, pp. 431–436. 3.3.1
- [55] O. Bebek and M. Çavusoglu, “Intelligent control algorithms for robotic-assisted beating heart surgery,” *IEEE Trans. Robot.*, vol. 23, no. 3, pp. 468–480, 2007. 3.3.1
- [56] T. J. Franke, O. Bebek, and M. C. Cavusoglu, “Improved prediction of heart motion using an adaptive filter for robot assisted beating heart surgery,” in *IEEE/RSJ Int. Conf. Intell. Robot. Sys. (IROS)*, 2007, pp. 509–515. 3.3.1
- [57] T. Franke, O. Bebek, and M. Çavusoglu, “Prediction of heartbeat motion with a generalized adaptive filter,” in *IEEE Int. Conf. Robot. Autom. (ICRA)*, 2008, pp. 2916–2921.
- [58] F. Liang, X. Meng, and Y. Yu, “Multivariate autoregressive model based heart motion prediction approach for beating heart surgery,” *Int. J. Adv. Robot. Syst.*, vol. 10, no. 129, 2013.
- [59] F. Liang, Y. Yu, H. Wang, and X. Meng, “Heart motion prediction in robotic-assisted beating heart surgery: A nonlinear fast adaptive approach,” *Int. J. Adv. Robot. Syst.*, vol. 10, no. 82, 2013.
- [60] E. E. Tuna, T. J. Franke, O. Bebek, A. Shiose, K. Fukamachi, and M. Çavusoglu, “Heart motion prediction based on adaptive estimation algorithms for robotic assisted beating heart surgery.” *IEEE Trans. Robot.*, vol. 29, no. 1, pp. 261–276, 2013. 3.3.1
- [61] L. Cuvillon, J. Gangloff, M. de Mathelin, and A. Forgione, “Toward robotized beating heart TECABG: assessment of the heart dynamics using high-speed vision,” in *Int. Conf. Med. Image Comput. Comput. Assist. Interv. (MICCAI)*, vol. 8, no. 2, 2005, pp. 551–558. 3.3.1

- [62] S. G. Yuen, P. M. P. Novotny, and R. D. Howe, “Quasiperiodic predictive filtering for robot-assisted beating heart surgery,” in *IEEE Int. Conf. Robot. Autom. (ICRA)*, 2008, pp. 3875–3880. 3.3.1
- [63] S. G. Yuen, D. T. Kettler, P. M. Novotny, R. D. Plowes, and R. D. Howe, “Robotic motion compensation for beating heart intracardiac surgery.” *Int. J. Robot. Res.*, vol. 28, no. 10, pp. 1355–1372, 2009. 3.3.1
- [64] A. Thakral, J. Wallace, D. Tomlin, and N. Seth, “Surgical motion adaptive robotic technology (SMART): Taking the motion out of physiological motion,” in *Int. Conf. Med. Image Comput. Comput. Assist. Interv. (MICCAI)*. Springer, 2001, pp. 317–325. 3.3.1
- [65] R. Richa, A. P. L. Bó, and P. Poignet, “Motion prediction for tracking the beating heart,” in *IEEE Int. Conf. Eng. Med. Biol. Soc. (EMBS)*, 2008, pp. 3261–3264. 3.3.1
- [66] ———, “Beating heart motion prediction for robust visual tracking,” in *IEEE Int. Conf. Robot. Autom. (ICRA)*, 2010, pp. 4579–4584.
- [67] ———, “Robust 3D visual tracking for robotic-assisted cardiac interventions.” *Int. Conf. Med. Image Comput. Comput. Assist. Interv. (MICCAI)*, vol. 13, no. 1, pp. 267–74, 2010.
- [68] ———, “Towards robust 3D visual tracking for motion compensation in beating heart surgery.” *Med. Image Anal.*, vol. 15, no. 3, pp. 302–15, 2011. 3.3.1
- [69] S. Tully, G. Kantor, and H. Choset, “Monocular feature-based periodic motion estimation for surgical guidance,” in *IEEE Int. Conf. Robot. Autom. (ICRA)*, 2013. 3.3.1
- [70] F. Liang and X. Meng, “A quadratic nonlinear prediction-based heart motion model following control algorithm in robotic-assisted beating heart surgery,” *Int. J. Adv. Robot. Syst.*, vol. 10, no. 13, 2013. 3.3.1
- [71] V. Duindam and S. Sastry, “Geometric motion estimation and control for robotic-assisted beating-heart surgery,” in *IEEE/RSJ Int. Conf. Intell. Robot. Sys. (IROS)*, 2007, pp. 871–876. 3.3.1
- [72] S. Tully, A. Bajo, G. Kantor, H. Choset, and N. Simaan, “Constrained filtering with contact detection data for the localization and registration of continuum robots in flexible environments,” in *IEEE Int. Conf. Robot. Autom. (ICRA)*, may 2012, pp. 3388–3394. 3.3.2
- [73] H. Zhong, T. Kanade, and D. Schwartzman, “”Virtual touch”: an efficient registration method for catheter navigation in left atrium,” in *Int. Conf. Med. Image Comput. Comput. Assist. Interv. (MICCAI)*, jan 2006, pp. 437–44. 3.3.2
- [74] D. Q. Huynh, “Metrics for 3D rotations: comparison and analysis,” *J. Math. Imag. Vis.*, vol. 35, no. 2, pp. 155–164, 2009. 4.3.1
- [75] J. J. Craig, *Introduction to Robotics: Mechanics and Control*, 3rd ed. Upper Saddle River, N.J.: Pearson Prentice/Hall, 2005. 4.3.3
- [76] Y. Wang, S. J. Riederer, and R. L. Ehman, “Respiratory motion of the heart:

- kinematics and the implications for the spatial resolution in coronary imaging,” *Magn. Reson. Med.*, vol. 33, no. 5, pp. 713–719, may 1995. 5.4
- [77] R. Schaback and C. Franke, “Solving partial differential equations by collocation using radial basis functions,” *Applied Mathematics and Computation*, vol. 93, no. 1, pp. 73–82, 1998. 6.2.1
- [78] M. Fornefett, K. Rohr, and H. S. Stiehl, “Elastic registration of medical images using radial basis functions with compact support,” in *Comp. Vis. Patt. Recog. (CVPR)*, 1999, pp. 402–407. 6.2.1
- [79] R. Tao, M. Tavakoli, R. Sloboda, and N. Usmani, “A Comparison of US versus MR Based 3D Prostate Shapes Using Radial Basis Function Interpolation and Statistical Shape Models.” *IEEE J. Biomed. Health Informat.*, vol. 19, no. 2, pp. 1–12, 2015.
- [80] J. C. Carr, W. R. Fright, and R. K. Beatson, “Surface interpolation with radial basis functions for medical imaging.” *IEEE tTrans. Med. Imag.*, vol. 16, no. 1, pp. 96–107, 1997. 6.2.1
- [81] M. D. Buhmann, *Radial Basis Functions: Theory and Implementations*. West Nyack, NY: Cambridge University Press, 2003. 6.2.1
- [82] D. E. Myers, S. De Iaco, D. Posa, and L. De Cesare, “Space-time radial basis functions,” *Comp. Math. Applicat.*, vol. 43, pp. 539–549, 2002. 6.2.2
- [83] M. P. Chapman, J. L. Lopez Gonzalez, B. E. Goyette, K. L. Fujimoto, Z. Ma, W. R. Wagner, M. A. Zenati, and C. N. Riviere, “Application of the HeartLander crawling robot for injection of a thermally sensitive anti-remodeling agent for myocardial infarction therapy,” *IEEE Int. Conf. Eng. Med. Biol. Soc. (EMBS)*, pp. 5428–5431, 2010. 7, 7.2
- [84] K. Fok, N. A. Wood, and C. N. Riviere, “Improved locomotion for the HeartLander robot for injection of an anti-remodeling hydrogel,” in *IEEE Annu. Northeast Bioeng. Conf. (NEBEC)*, 2012, pp. 207–208. 7.2
- [85] K. L. Fujimoto, Z. Ma, D. M. Nelson, R. Hashizume, J. Guan, K. Tobita, and W. R. Wagner, “Synthesis, characterization and therapeutic efficacy of a biodegradable, thermoresponsive hydrogel designed for application in chronic infarcted myocardium,” *Biomaterials*, vol. 30, no. 26, pp. 4357–68, sep 2009. 7.1.2
- [86] D. M. Nelson, R. Hashizume, T. Yoshizumi, A. K. Blakney, Z. Ma, and W. R. Wagner, “Intramyocardial injection of a synthetic hydrogel with delivery of bFGF and IGF1 in a rat model of ischemic cardiomyopathy,” *Biomacromolecules*, vol. 15, no. 1, pp. 1–11, 2014. 7, 7.1.2
- [87] M. G. S. J. Sutton and N. Sharpe, “Left ventricular remodeling after myocardial infarction: pathophysiology and therapy,” *Circulation*, vol. 101, no. 25, pp. 2981–2988, jun 2000. 7.1.1
- [88] E. Tous, B. Purcell, J. L. Ifkovits, and J. a. Burdick, “Injectable acellular hydrogels for cardiac repair,” *J. Cardiovasc. Transl. Res.*, vol. 4, no. 5, pp. 528–542, 2011. 7.1.1
- [89] A. A. Rane and K. L. Christman, “Biomaterials for the treatment of myocardial

- infarction: a 5-year update,” *J. Amer. Coll. Cardiol.*, vol. 58, no. 25, pp. 2615–2629, 2011. 7.1.1
- [90] “Safety and feasibility of the injectable BL-1040 implant,” 2012. 7.1.1
- [91] “A study of VentiGel in early and late post-myocardial infarction patients,” 2015.
- [92] “Safety and feasibility of Algisyl-LVR as a method of left ventricular restoration in patients with DCM undergoing open-heart surgery,” 2012. 7.1.1
- [93] S. B. Seif-Naraghi, J. M. Singelyn, M. a. Salvatore, K. G. Osborn, J. J. Wang, U. Sampat, O. L. Kwan, G. M. Strachan, J. Wong, P. J. Schup-Magoffin, R. L. Braden, K. Bartels, J. a. DeQuach, M. Preul, A. M. Kinsey, A. N. DeMaria, N. Dib, and K. L. Christman, “Safety and efficacy of an injectable extracellular matrix hydrogel for treating myocardial infarction,” *Sci. Transl. Med.*, vol. 5, no. 173, p. 173ra25, 2013. 7.1.1
- [94] J. Leor, S. Tuvia, V. Guetta, F. Manczur, D. Castel, U. Willenz, Ö. Petneházy, N. Landa, M. S. Feinberg, E. Konen, O. Goitein, O. Tsur-Gang, M. Shaul, L. Klappper, and S. Cohen, “Intracoronary Injection of In Situ Forming Alginate Hydrogel Reverses Left Ventricular Remodeling After Myocardial Infarction in Swine,” *J. Amer. Coll. Cardiol.*, vol. 54, no. 11, pp. 1014–1023, 2009. 7.1.1
- [95] J. F. Wenk, S. T. Wall, R. C. Peterson, S. L. Helgerson, H. N. Sabbah, M. Burger, N. Stander, M. B. Ratcliffe, and J. M. Guccione, “A method for automatically optimizing medical devices for treating heart failure: designing polymeric injection patterns,” *J. Biomech. Eng.*, vol. 131, no. 12, p. 121011, 2009. 7.1.1
- [96] G. M. Fomovsky, J. R. Macadangdang, G. Ailawadi, and J. W. Holmes, “Model-based design of mechanical therapies for myocardial infarction.” *J. Cardiovasc. Transl. Res.*, vol. 4, no. 1, pp. 82–91, 2011. 7.1.1
- [97] Y. Zhu, N. A. Wood, K. Fok, T. Yoshizumi, D. W. Park, H. B. Jiang, D. Schwartzman, M. A. Zenati, T. Uchibori, W. R. Wagner, and C. N. Riviere, “Design of a coupled thermoresponsive hydrogel and robotic injection system for myocardial infarction therapy,” *Ann. Thorac. Surg.*, 2015. 7.1.2
- [98] J. R. Reynolds and H. Hartshorne, *A System of Medicine, Volume 2*, ser. A System of Medicine, J. R. Reynolds, Ed. Philadelphia: H.C. Lea’s Son & Company, 1880, no. v. 2. 7.3.3
- [99] A. D. Costanza, N. A. Wood, M. J. Passineau, R. J. Moraca, S. H. Bailey, T. Yoshizumi, and C. N. Riviere, “A parallel wire robot for epicardial interventions,” in *IEEE Int. Conf. Eng. Med. Biol. Soc. (EMBS)*, 2014, pp. 6155–6158. 8
- [100] M. Breault, A. D. Costanza, N. A. Wood, M. J. Passineau, and C. N. Riviere, “Hybrid force/position control for the Cerberus epicardial robot,” in *IEEE Int. Conf. Eng. Med. Biol. Soc. (EMBS)*, 2015, pp. 7776–9.
- [101] ———, “Auto-calibration for a planar epicardial wire robot,” in *IEEE Annu. Northeast Bioeng. Conf. (NEBEC)*, 2015.
- [102] A. D. Costanza, M. S. Breault, N. A. Wood, M. J. Passineau, R. J. Moraca, and

- C. N. Riviere, "Hybrid control of an epicardial parallel wire robot," *IEEE Robot. Autom. Let.*, 2015. 8
- [103] A. S. Go, D. Mozaffarian, V. L. Roger, E. J. Benjamin, J. D. Berry, M. J. Blaha, S. Dai, E. S. Ford, C. S. Fox, S. Franco, H. J. Fullerton, C. Gillespie, S. M. Hailpern, J. a. Heit, V. J. Howard, M. D. Huffman, S. E. Judd, B. M. Kissela, S. J. Kittner, D. T. Lackland, J. H. Lichtman, L. D. Lisabeth, R. H. Mackey, D. J. Magid, G. M. Marcus, A. Marelli, D. B. Matchar, D. K. McGuire, E. R. Mohler, C. S. Moy, M. E. Mussolino, R. W. Neumar, G. Nichol, D. K. Pandey, N. P. Paynter, M. J. Reeves, P. D. Sorlie, J. Stein, A. Towfighi, T. N. Turan, S. S. Virani, N. D. Wong, D. Woo, and M. B. Turner, "Heart disease and stroke statistics - 2014 update: a report from the American Heart Association," *Circulation*, vol. 129, no. 3, pp. 1–268, 2014. 8.1.1
- [104] M. Jessup, B. Greenberg, D. Mancini, T. Cappola, D. F. Pauly, B. Jaski, A. Yaroshinsky, K. M. Zsebo, H. Dittrich, and R. J. Hajjar, "Calcium upregulation by Percutaneous Administration of Gene Therapy in Cardiac Disease (CUPID): a phase 2 trial of intracoronary gene therapy of sarcoplasmic reticulum Ca²⁺-ATPase in patients with advanced heart failure," *Circulation*, vol. 124, no. 3, pp. 304–13, 2011. 8.1.1
- [105] M. Giacca and A. H. Baker, "Heartening results: the CUPID gene therapy trial for heart failure." *Mol. Ther.*, vol. 19, no. 7, pp. 1181–2, jul 2011.
- [106] B. E. Jaski, M. L. Jessup, D. M. Mancini, T. P. Cappola, D. F. Pauly, B. Greenberg, K. Borow, H. Dittrich, K. M. Zsebo, and R. J. Hajjar, "Calcium upregulation by percutaneous administration of gene therapy in cardiac disease (CUPID Trial), a first-in-human phase 1/2 clinical trial." *J. Card. Fail.*, vol. 15, no. 3, pp. 171–81, apr 2009.
- [107] K. Zsebo, A. Yaroshinsky, J. J. Rudy, K. Wagner, B. Greenberg, M. Jessup, and R. J. Hajjar, "Long-term effects of AAV1/SERCA2a gene transfer in patients with severe heart failure: analysis of recurrent cardiovascular events and mortality." *Circ. Res.*, vol. 114, no. 1, pp. 101–8, jan 2014.
- [108] T. Tang, M. H. Gao, and H. K. Hammond, "Prospects for gene transfer for clinical heart failure," *Gene Ther.*, vol. 19, no. 6, pp. 606–12, 2012. 8.1.1
- [109] M. Hedman, J. Hartikainen, and S. Ylä-Herttuala, "Progress and prospects: hurdles to cardiovascular gene therapy clinical trials," *Gene Ther.*, vol. 18, no. 8, pp. 743–9, 2011. 8.1.1
- [110] Y. Kawase, D. Ladage, and R. R. J. Hajjar, "Rescuing the failing heart by targeted gene transfer," *J. Am. Coll. Cardiol.*, vol. 57, no. 10, pp. 1169–80, 2011. 8.1.1
- [111] R. Gupta, J. Tongers, and D. W. Losordo, "Human studies of angiogenic gene therapy," *Circ. Res.*, vol. 105, no. 8, pp. 724–36, oct 2009. 8.1.1
- [112] K. Ishikawa, L. Tilemann, K. Fish, and R. J. Hajjar, "Gene delivery methods in cardiac gene therapy." *J. Gene Med.*, vol. 13, no. 10, pp. 566–72, 2011. 8.1.1
- [113] T. Bruckmann, L. Mikelsons, T. Brandt, M. Hiller, and D. Schramm, "Wire Robots Part I: Kinematics, Analysis & Design," in *Parallel Manipulators, New Develop-*

- ments, J.-H. Ryu, Ed. Vienna: InTech, 2008, ch. 6, pp. 109–132. 8.1.2
- [114] R. L. Williams and P. Gallina, “Translational planar cable-direct-driven robots,” *J. Intell. Robot. Syst.*, vol. 37, pp. 69–96, 2003. 8.1.2
- [115] S. A. Hamid and N. Simaan, “Design and synthesis of wire-actuated universal-joint wrists for surgical applications,” *IEEE Int. Conf. Robot. Autom. (ICRA)*, pp. 1807–1813, 2009. 8.1.2
- [116] J. Wendlandt and S. Sastry, “Design and control of a simplified Stewart platform for endoscopy,” in *IEEE Annu. Conf. Decision Contr.*, 1994, pp. 357–62. 8.1.2
- [117] E. Ottaviano, M. Ceccarelli, and M. Ciantis, “A 4-4 cable-based parallel manipulator for an application in hospital environment,” in *IEEE Mediteranean Conf. Contr. Aut.*, 2007, pp. 1–6. 8.1.2
- [118] G. Rosati, P. Gallina, and S. Masiero, “Design, implementation and clinical tests of a wire-based robot for neurorehabilitation.” *IEEE Trans. Neural Syst. Rehabil. Eng.*, vol. 15, no. 4, pp. 560–9, 2007. 8.1.2
- [119] D. Surdilovic, J. Zhang, and R. Bernhardt, “STRING-MAN: Wire-robot technology for safe, flexible and human-friendly gait rehabilitation,” in *IEEE Int. Conf. Rehabil. Robot.*, 2007, pp. 446–453. 8.1.2
- [120] Y.-J. Ou and L.-W. Tsai, “Theory of isotropic transmission for tendon-driven manipulators,” in *Proc. of the ASME Design Technical Conf.*, vol. 72, 1994, pp. 53–61. 8.2.3
- [121] R. Verhoeven, “Analysis of the workspace of tendon-based Stewart platforms,” Doctoral Dissertation, Universität Duisburg-Essen, 2004. 8.2.3
- [122] X. Pennec and J.-P. Thirion, “A framework for uncertainty and validation of 3-D registration methods based on points and frames,” *Int. J. Comput. Vis.*, vol. 8, no. 54, pp. 204–229, 1997. 10.1
- [123] M. H. Moghari and P. Abolmaesumi, “A novel incremental technique for ultrasound to CT bone surface registration using unscented Kalman filtering,” in *Int. Conf. Med. Image Comput. Comput. Assist. Interv. (MICCAI)*, 2005, pp. 197–204. 10.1